

AD-A095 278

EG AND G INC SALEM MASS

F/G 9/1

HIGH VOLTAGE, LOW INDUCTANCE HYDROGEN THYRATRON STUDY PROGRAM.(U)

JAN 81 R F CARISTI, D V TURNQUIST

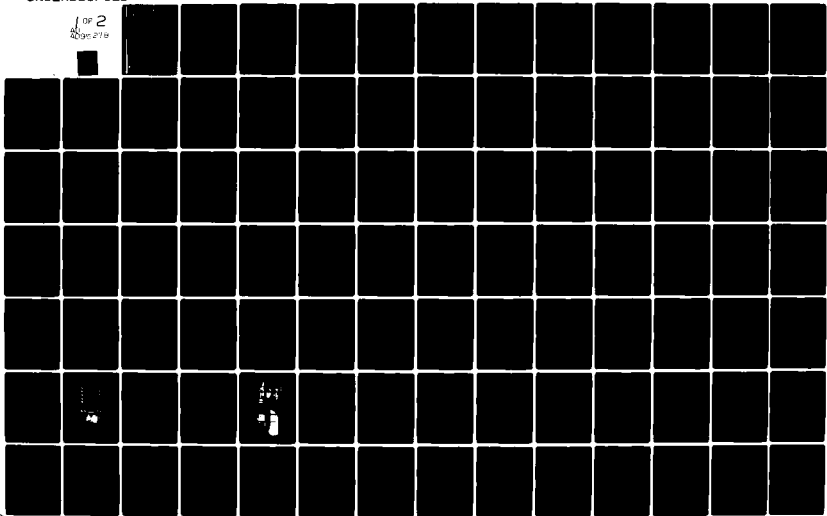
DAAB07-78-C-2977

UNCLASSIFIED

DELET-TR-78-2977-F

NL

1 of 2
299278



LEVEL

(13)



Research and Development Technical Report
DELET-TR-78-2977-F

AD A 09 5278

**HIGH VOLTAGE, LOW INDUCTANCE HYDROGEN THYRATRON
STUDY PROGRAM**

Robert F. Caristi
David V. Turnquist
EG&G, Inc.
35 Congress Street
Salem, Massachusetts 01970

DTIC
ELECTE
FEB 20 1981
S
C

January 1981

Final Report for the Period 4 September 1978 to 3 March 1980

DISTRIBUTION STATEMENT: Approved for Public Release; Distribution Unlimited

Prepared for:
Electronics Technology & Devices Laboratory

ERADCOM

U.S. ARMY ELECTRONICS R&D COMMAND, FORT MONMOUTH, NEW JERSEY 07703

81 2 20 069

DBC FILE COPY

X

NOTICES

Disclaimers

The citation of trade names and names of manufacturers in this report is not to be construed as official Government endorsement or approval of commercial products or services referenced herein.

Disposition

Destroy this report when it is no longer needed. Do not return it to the originator.

Unclassified

SECURITY CLASSIFICATION OF THIS PAGE (When Data Entered)

19 REPORT DOCUMENTATION PAGE		READ INSTRUCTIONS BEFORE COMPLETING FORM	
1. REPORT NUMBER 18 DELET-TR-78-2977-F ✓ AD A095278	2. GOVT ACCESSION NO.	3. RECIPIENT'S CATALOG NUMBER	
4. TITLE (and Subtitle) High Voltage, Low Inductance Hydrogen Thyratron Study Program.		5. PERIOD COVERED Final Report 4 Sep 78- to 3 Mar 80	
7. AUTHOR(s) Robert F. Caristi David V. Turnquist	8. CONTRACT OR GRANT NUMBER(s) DAAB07-78-C-2977 ✓	6. PERFORMING ORG. REPORT NUMBER	
9. PERFORMING ORGANIZATION NAME AND ADDRESS EG&G, Inc. 35 Congress Street Salem, MA 01970	10. PROGRAM ELEMENT, PROJECT, TASK AREA & WORK UNIT NUMBERS 62705A 1L162705AH9402		
11. CONTROLLING OFFICE NAME AND ADDRESS Electronics Technology and Devices Lab. (ERADCOM) ATTN: DELET-BG Fort Monmouth, NJ 07703	12. REPORT DATE January 1981	13. NUMBER OF PAGES 129	
14. MONITORING AGENCY NAME & ADDRESS (if different from Controlling Office) 12 132	15. SECURITY CLASS. (of this report) Unclassified	15a. DECLASSIFICATION/DOWNGRADING SCHEDULE	
16. DISTRIBUTION STATEMENT (of this Report) Approved for public release; distribution unlimited			
17. DISTRIBUTION STATEMENT (of the abstract entered in Block 20, if different from Report)			
18. SUPPLEMENTARY NOTES			
19. KEY WORDS (Continue on reverse side if necessary and identify by block number) Thyratrons, Switches, Pulse Generators, Blumleins, Pulse Modulators, Nanosecond Pulsers, High Voltage Components			
20. ABSTRACT (Continue on reverse side if necessary and identify by block number) The second phase of a multi-phase program of research and development to gain the information necessary to fabricate a high voltage, low inductance hydrogen thyratron switch has now been completed. The thyratron is to be capable of switching tens of kiloamperes within tens of nanoseconds at voltage levels as high as 250 kV. To achieve low inductance, the thyratron is operated within a close-fitting coaxial current return. Both the tube and the return are made physically short, and the tube is designed such that the discharge is constrained to flow principally at the outer reaches of the device. A technique has (over) → cont			

DD FORM 1 JAN 73 1473 EDITION OF 1 NOV 65 IS OBSOLETE

Unclassified

SECURITY CLASSIFICATION OF THIS PAGE (When Data Entered)

390408

Handwritten initials/signature

~~CONF~~ 20. been developed for modelling various types of box grids and then using computer-generated field plots to aid in the specifics of grid design. This model has been used to generate a comprehensive set of theoretical relations that are useful to determine the anode dissipation to be expected.

Experimental results are described and discussed. Included are the ceramic test results, holdoff vs. time on charge and gas pressure, stage voltage addition, operation at high pulse repetition rates, current rise time as a function of gas pressure, and the triggering characteristics of multi-stage, box-grid tubes.

Finally, the design of an intermediate experimental tube is discussed at length. This tube is expected to have an inductance less than 50nH and to operate at 150kV. Its design is based on both the theoretical and experimental results obtained during this phase of the research Program.

The overall conclusion is that a hydrogen thyratron capable of achieving the Program's objectives is a feasible proposition. However, further work is required to achieve the maximum holdoff at the highest practical gas pressure, and both theoretical and experimental studies will be necessary to devise and test multi-stage holdoff sections capable of operating at significant pulse repetition rates.

LIST OF SYMBOLS AND ABBREVIATIONS

<u>Symbol</u>	<u>Definition</u>
C1	Interstage Capacitance
C2	Stage-to-Ground Capacitance
DBV	Dynamic Breakdown Voltage
di/dt	Rate of Rise of Anode Current
E-E	Electrode Spacing
Ef	Cathode Heater Voltage
egy	Peak Forward Grid Voltage
epy	Peak Forward Anode Voltage
epx	Peak Inverse Anode Voltage
Eres	Reservoir Heater Voltage
ib	Peak Anode Current
Ib	Average Anode Current
Ip	RMS Anode Current
L _T	Tube Inductance
P	Gas Pressure in Tube
Pa	Anode Dissipation
prr	Pulse Repetition Rate
SBV	Static Breakdown Voltage
tad	Anode Delay Time
tj	Time Jitter of Anode Current Pulse
tp	Width of Anode Current Pulse
tr	Rise Time of Anode Current Pulse
TUT	Tube Under Test
α	Isolation Coefficient (Defined in Text)
γ	Transfer Efficiency (Defined in Text)
Π_b	Anode Heating Factor
τ_j	Time Constant of Anode Fall
ρ	Recovery Factor (Defined in Text)

Accession to
 PHS 6848
 PHS Lab
 Chamberland
 Jacksonville

FY-
 Distribution
 Availability Codes
 Available for
 Special

Dist: **A**

TABLE OF CONTENTS

<u>Section</u>		<u>Page</u>
	LIST OF SYMBOLS AND ABBREVIATIONS.	iii
1	PREFACE.	1
2	INTRODUCTION AND SUMMARY	3
	a. Purpose and Concerns of the Program.	3
	b. Report Organization and Summary.	4
3	REVIEW OF PHASE I.	9
4	OBJECTIVES OF PHASE II	11
5	DESIGN OF MULTI-STAGE, BOX-GRID TUBES.	13
	a. General Design Principles.	13
	(1) Box-Type Gradient Grids	13
	(2) Interstage and Stray Capacitance.	18
	(3) Stage Voltage Addition.	21
	b. Extended Design Studies.	23
	(1) Box-Grid Geometry	23
	(2) Anode Dissipation	33
6	TEST KITS FOR HIGH VOLTAGE, LOW INDUCTANCE TUBES	55
	a. 80 kV Pulse Charge System.	55
	b. 50 kV High di/dt System.	57
	c. 250 kV Pulse Charge System	61
7	EXPERIMENTAL TUBES AND TEST RESULTS.	63
	a. Objects of the Experimental Work	63
	b. Experimental Tubes	63
	(1) HY-5505	63
	(2) HY-5506	64
	(3) HY-5507	64
	(4) HY-5508	64
	(5) HY-5509	64
	(6) HY-5515	66
	(7) HY-5525	66

<u>Section</u>	<u>Page</u>
c. Test Results and Interpretation.	66
(1) Ceramic Stress Tests.	66
(2) Holdoff vs Time on Charge	74
(3) Holdoff vs Gas Pressure	79
(4) Stage Voltage Addition.	92
(5) Operation at High Pulse Repetition Rates.	97
(6) Current Rise Time vs Gas Pressure	103
(7) Triggering Characteristics.	106
8 INTERMEDIATE HIGH VOLTAGE, LOW INDUCTANCE HYDROGEN THYRATRON — HY-5525.	113
9 CONCLUSIONS FROM PHASE II AND PLANS FOR PHASE III.	117
a. Conclusions from Phase II.	117
b. Plans for Phase III.	119
10 REFERENCES	123
DISTRIBUTION LIST.	125

LIST OF ILLUSTRATIONS

<u>Figure</u>		<u>Page</u>
1	Typical aperture arrangements for box-type gradient grids .	16
2	Internally baffled box-type grid.	16
3	Basic configuration for minimizing insulator stress	17
4	Model used to calculate interelectrode capacitance.	19
5	A typical computer-generated field plot	26
6	An expanded view of the equipotentials within the box grid of Figure 5	27
7	Effect of increasing slot-width by 20%.	27
8	Effect of reducing slot-width by 40%.	28
9	A typical field pattern for a double-walled box grid.	28
10	Field pattern when a thin baffle is added to the grid of Figure 9.	29
11	Field pattern when a thick baffle is added to the grid of Figure 9.	29
12	A baffled box-grid where the slots are offset within the box	30
13	Results of a typical box grid parametric study.	30
14	Results of a parametric study performed to investigate the sensitivity of the transfer efficiency to the dimensions and location of the grid baffle	31
15	Relationship between isolation coefficient and transfer efficiency.	33
16	Waveform assumed for the anode fall	35
17	Circuits for a thyratron discharging a transmission line into a resistive load	37
18	Plot of the function $f(K_A)$	42
19	Ratio of the anode energy with inductance in the circuit to the anode energy with no inductance in the circuit.	43
20	Plot of the ratio $f(K_A)/f(0.1)$	43
21	Percentage of the stored energy that is lost to the commutation process as a function of parameter K	46

<u>Figure</u>		<u>Page</u>
22	Function $f(K_A)$ vs ratio τ_i/τ_L	48
23	Schematic and waveforms - 80 kV test kit.	55
24	Anode waveform used to investigate prr characteristics. . .	56
25	Schematic and waveforms - high di/dt test kit	58
26	Construction of high di/dt kit.	59
27	Schematic of 250 kV test kit.	61
28	Five-stage HY-5506.	65
29	Typical ceramic sample with electrodes.	68
30	Marx generator used for sample testing.	68
31	Waveforms showing sample holdoff and sample breakdown . . .	73
32	Dynamic breakdown voltage as a function of pressure, with time on charge as a parameter	77
33	Dynamic and static breakdown - HY-5506.	78
34	Typical reservoir calibration curve	81
35	Minimum epy for the HY-5509	81
36	Distribution of charging voltage - HY-5506.	83
37	Breakdown characteristics - HY-5506	84
38	Breakdown characteristics - HY-5508	85
39	Breakdown characteristics - HY-5509	86
40	Dynamic breakdown characteristics - HY-5509	87
41	Comparison of DBV - HY-5506, HY-5508, and HY-5509	89
42	Anode DBV - HY-5509 with first stage shunted.	91
43	DBV as a function of pressure, with gap spacing as a parameter - various single stage tubes.	91
44	Breakdown characteristics at high prr - HY-5.	99
45	Recovery factor at high pressures - HY-5.	99
46	Breakdown characteristics at high prr - HY-5506	100
47	Breakdown characteristics at high prr - HY-5508	100
48	Breakdown characteristics at high prr - HY-5509	101
49	Comparison of recovery factors - multistage tubes and HY-5.	102
50	A typical anode current pulse at high gas pressure.	103
51	Rise time as a function of gas pressure - multistage tubes	104
52	Intermediate experimental tube - HY-5525.	114

LIST OF TABLES

<u>Table</u>		<u>Page</u>
1	Electrical characteristics of high voltage, low inductance hydrogen thyratron.	3
2	Calculated interstage capacitance for a typical box-grid assembly.	20
3	Summary of equations related to anode dissipation	52
4	Characteristics of Marx generator used for ceramic sample evaluation.	69
5	Breakdown voltages of ceramic samples when immersed in transformer oil	71
6	Holdoff properties of ceramic samples when immersed in distilled water	73
7	Breakdown voltages for the samples of Table 6 when the samples were immersed in transformer oil.	73
8	Time related thyratron breakdown regimes.	75
9	Dynamic breakdown voltage as a function of time on charge, DBV(T), normalized to dynamic breakdown voltage for 2 mS on charge	76
10	Calculated and measured anode breakdown voltages for HY-5506	94
11	Calculated and measured anode breakdown voltages for HY-5508	95
12	Calculated and measured anode breakdown voltages for HY-5509	96
13	Breakdown times of box-grid tubes	111

1 PREFACE

This Final Technical Report documents the results of a program of research and development that commenced 4 September 1978 and ended 3 March 1980, and was generally known as Phase II of the High Voltage, Low Inductance Hydrogen Thyatron Study Program. Funded under ERADCOM Contract DAAB07-78-C-2977, this work was directed toward gaining the information necessary to fabricate a thyatron switch capable of operating under the electrical conditions stated in ERADCOM's Technical Guidelines dated 7 April 1978.

The work described was performed by the High Energy Switch Department of EG&G's Electronic Components Division, 35 Congress Street, Salem, Massachusetts. Mr. David V. Turnquist was Program Manager and Mr. Robert F. Caristi was Program Engineer. Mr. John E. Creedon of ERADCOM was Technical Monitor.

The authors of this report wish to recognize the significant contributions of Dr. Chathan M. Cooke, Director of Dielectric Research at the High Voltage Research Laboratory of the Massachusetts Institute of Technology, Cambridge, Massachusetts. Dr. Cooke is a consultant to EG&G.

2 INTRODUCTION AND SUMMARY

a. Purpose and Concerns of the Program

The purpose of the High Voltage, Low Inductance Hydrogen Thyatron Study Program was to develop a hydrogen thyatron capable of holding off hundreds of kilovolts before switching a fast-rising current pulse of tens of kiloamperes. The applicable Technical Guidelines (as issued by ERADCOM) are given in Table 1.

Table 1. Electrical characteristics of high voltage, low inductance hydrogen thyatron.

Characteristic	Symbol	Objective
Peak Forward Voltage	epy	250 kV
Peak Anode Current	ib	20 kA
Pulse Width (90%)	tp	60 nS
Pulse Rise Time (10% to 90%)	tr	5 nS
Current Rate of Rise (10% to 90%)	di/dt	3×10^{12} A/S
Number of Pulses per Burst	--	100
Off Time to Burst Duration Ratio	--	100:1
Total Inductance (Switch and Connectors)	L _T	125 nH

During Phase I of the Program, fundamental design principles were established for such tubes. Subject areas where experimentally generated information was required were also determined. The primary areas in need of experimental work were the maximum allowable insulator stress and the holdoff-commutation characteristics of multi-stage tubes having box-type gradient grids. Efforts during Phase II were principally directed toward generating these data.

The basic approach throughout the Program was to develop a theoretically based explanation for experimentally observed phenomena whenever possible. During Phase II, theoretical work on box grid design was continued and the model for gas discharge switches was used to predict the anode dissipation expected in actual practice.

An intermediately sized experimental tube has been designed and is presently being built for delivery to ERADCOM where further experimental data will be generated.

b. Report Organization and Summary

This report does not document every experimental and theoretical result generated during Phase II, nor does it contain descriptions of experimental apparatus or techniques beyond the extent necessary to provide a basic understanding of the work performed. Monthly letter reports were provided during the Program covering such details. This report summarizes principal findings, and interprets their significance in light of the overall objectives of the Program.

Section 3 briefly reviews the work done during Phase I. Its objects were to establish design principles for high voltage, low inductance hydrogen thyratrons, and to determine those areas where experimentally generated information was required.

Parametric studies performed during Phase I showed that a reasonable compromise could be achieved among inductance, stray capacitance, and tube-to-return electric fields at the desired anode voltage. A model was developed for gas discharge switches that considered their finite commutation times. The results obtained with the model indicated that reasonably fast current rise times could be achieved with a hydrogen thyratron having the anticipated inductance, and operated at a sufficiently high gas pressure.

The tube designs that evolved during Phase I were based on the use of multiple, short, box-type gradient grids. The assumption was that such tubes could satisfy the goals set by the Technical Guidelines subject to the ability of the inter-stage insulators to withstand very high voltage stress under short-pulse conditions, and also subject to the holdoff/commutation characteristics of multiple, box-grid structures. Experimental work was required to resolve these two contingencies, and efforts during Phase II were principally directed toward addressing these issues.

Section 4 outlines the objectives of Phase II in further detail. Theoretical and experimental investigations were performed in several areas pertinent to the design of high voltage, low inductance tubes. All of this work was directed toward gaining the information necessary to design a thyatron switch capable of meeting the requirements listed in Table 1.

Section 5 discusses various aspects of high voltage, low inductance tube design, with emphasis placed on the results of extended theoretical studies that addressed the subjects of box grid geometry and the development of a set of relationships that are useful to predict the anode dissipation to be expected under a variety of operating conditions. The grid design studies showed that it was possible to model the box-grid geometry and then to use computer-generated field plots to aid in the specifics of grid design. The transfer efficiency concept was devised to serve as a measure of the ability of a box-grid to provide sufficient isolation between stages so that the individual stage voltages are algebraically additive.

In the anode dissipation study, the commutating gas discharge switch model was used to generate relationships that predict thyatron anode dissipation to a degree of accuracy not previously attempted. This study provides a theoretical basis for many phenomena that have been previously observed but not quantified. The thrust of the analysis is to point to the significance of operating high performance tubes at high gas pressures in order to minimize the significant anode dissipation that results when the circuit rise time and the anode fall time are comparable.

Section 6 describes the test kits that were used to generate the experimental data reported herein. Of particular interest is the 50 kV high di/dt kit that was designed to have an inductance of only 10 nH — significantly less than that of the experimental tubes with which it was designed to operate. Experimental results showed that this kit had an inductance of the order calculated, and its performance was instrumental in advancing knowledge of several of the fundamental characteristics of low inductance, multi-gap tubes.

Section 7 presents highlights of experimental results, starting with the objects of the experimental work, and continuing with the various experimental tubes built under the auspices of the Program. Since an important aspect of the experimental effort was to determine the breakdown properties of the high alumina ceramics universally used for the insulators of high performance hydrogen thyratrons, a significant experimental effort was exerted in this area. The conclusion was that the ceramics can withstand electric fields well above those to be expected in a well designed tube capable of meeting the objectives of this Program.

For the experimental tubes under test, dynamic holdoff as a function of time on charge and as a function of gas pressure was determined, and both stage voltage addition properties and performance at high pulse repetition rates were investigated. Characterization was completed by determining their anode current rise times and their triggering characteristics — both as a function of operating gas pressure.

Section 8 provides a detailed description of the intermediately sized experimental tube now being built and which will be delivered to ERADCOM for subsequent testing and evaluation. This tube is a five-stage device designed to operate at a peak forward anode voltage of 150 kV and to have an inductance of less than 50 nH. This tube is expected to be capable of generating a 10 kA, 60 nS current pulse having a rise time of 10 to 15 nS. A pulse repetition rate of 1 kHz should be achievable in the burst mode.

Section 9 discusses the principal conclusions from work accomplished during Phase II and plans for Phase III. The work of Phase II showed that the breakdown properties of the ceramic insulators would not necessarily inhibit the development of a tube that could meet the objectives of the Program. It was further established that a multi-stage tube having a plurality of short, box-type gradient grids could in fact hold off, commutate, and recover in substantially the same manner as a conventional tube. Near-perfect stage voltage addition can be accomplished, and very low tube inductances can be achieved.

For the tubes under consideration here, the rise time of the anode current is limited principally by the anode fall time. The time constant of

the anode fall is solely a function of gas pressure, and the time constant decreases as the gas pressure increases. Therefore, low inductance tubes must be operated at high pressure, but such operation reduces tube holdoff capabilities. Command pulse charging of the anode with a time on charge of a few microseconds takes advantage of tube dynamic holdoff capabilities, but the improvement in holdoff, although worthwhile, is not extraordinary, particularly at high pressures. As a result, the single most important advance that needs to be made in the development of high voltage, low inductance tubes is to devise a scheme that improves gap holdoff at high tube gas pressure.

The rise time capabilities and triggering characteristics of multi-stage, box-grid tubes are of the same general nature as those of conventional tubes. Their recovery properties, although poor when compared to those of single-stage tubes, are materially better than those of multi-stage, cavity types.

The overall conclusion is that a hydrogen thyratron capable of meeting the objectives of the Program is a feasible proposition. No impediments to success are known to exist. However, further work is required to achieve maximum holdoff at the highest practical gas pressure, and multi-stage holdoff sections that are capable of fast recovery have yet to be developed.

Work under Phase II will continue and be extended to include building and testing a series of experimental tubes specifically designed to address those considerations that prompt the greatest practical concern. Among these are insulator integrity at voltages up to 250 kV, upper-stage arcing at high working voltages, and stage voltage addition under high field conditions.

Long range plans include studying those factors that presently serve to limit the pulse rate capabilities of high voltage, low inductance tubes and to extend those capabilities as far as possible. Our goal is to demonstrate high voltage operation at 10 kHz by the end of 1981.

3 REVIEW OF PHASE I

The objectives of Phase I were (1) to establish design principles for high voltage, low inductance tubes; and (2) to determine those areas where theory alone was inadequate, and new, experimentally generated information was required.* It was immediately apparent that physically short tubes fitted with coaxial current returns were required to achieve low inductance, and that command pulse charging was necessary to achieve high total holdoff from tubes having a relatively small number of gaps in series. Pulse charging required that the distribution of the applied voltage across the various gaps be determined by the interelectrode and stray capacitances. Both the stray capacitance and the tube/return inductance were functions of the tube and return diameters, as was the voltage stress in the insulating medium between the tube and the return.

It followed that a parametric study of the properties of a coaxial geometry and a study of capacitance-controlled voltage division were required to establish reasonable design boundaries. These studies showed that it would be necessary to stress the interstage ceramic insulators to levels well beyond standard practice. No experimental data were known to exist for the appropriate stresses and time scales, and existing data concerning the holdoff-pressure characteristic of deuterium under pulse charge conditions were inadequate; therefore, experimental work was necessary.

Finally, it remained to be experimentally demonstrated that a multi-stage tube having the short, tightly baffled, box-type gradient grids necessary for low inductance would exhibit stage voltage addition while simultaneously having the capacity to trigger and commutate like a conventional tube.

Parametric studies showed that a reasonable compromise could be obtained among inductance, stray capacitance, and tube-to-return electric fields, but the effect of tube inherent turn-on time on the rise of the circuit current

*The results of the Phase I effort are documented in Technical Report No. DELET-TR-77-2725-F dated March 1979.

remained to be determined. A model was developed for commutating gas discharge switches that considered their finite commutation time. Thus tube holdoff capability (a function of gas pressure and electrode spacing) could be related to its current rise time capability (a function of gas pressure and inductance). Comparisons of theory and experiment showed that the model accurately predicted tube performance over a wide range of operating conditions.

To perform the ceramic stress tests a 250 kV Marx generator was designed, built, and characterized, and a suitable collection of ceramic test pieces was processed. To demonstrate multi-gap, box-grid operation, a five-stage tube having this type of construction was designed and built. Actual testing of both the ceramics and the first experimental tube was performed during Phase II; the results are discussed later in this report.

The overall conclusion from the work of Phase I was that a 250 kV tube capable of delivering tens of kiloamperes in tens of nanoseconds was feasible, subject to the ability of the insulators to withstand the stress and the general efficacy of the (then) untried multi-stage, box-grid design. The work of Phase II was principally directed toward resolving the matter of ceramic stress and investigating the holdoff/commutation properties of multi-stage, box-grid tubes. The results of this work are described in detail in the remainder of this report.

4 OBJECTIVES OF PHASE II

The objectives of Phase II were to verify by experimentation the conclusions of Phase I, and to translate the general design concepts established during Phase I into detailed criteria that could be used to design practical high voltage, low inductance tubes. It was first necessary to determine the integrity of high alumina ceramics when they were subjected to high voltage stress on the time scales appropriate for thyatron insulators. Next it was required to demonstrate experimentally that a multi-gap tube comprised of several box-type gradient grids could trigger, commute, and recover holdoff in substantially the same manner as a conventional tube.

Theoretical and experimental investigations were conducted concerning the holdoff/commutation compromise, the design of box-type grids, stage voltage addition, operation at high pulse repetition rates, anode dissipation under high di/dt conditions, and various other aspects of high voltage, low inductance tube design. All of this work was directed toward gaining the theoretical and experimental information necessary to design a thyatron switch capable of meeting the requirements listed in Table 1.

Finally, an intermediately sized experimental tube was designed and is now being built for delivery to ERADCOM where further experimental data will be generated.

5 DESIGN OF MULTI-STAGE, BOX-GRID TUBES

The design of high voltage, low inductance tubes was generally addressed during Phase I. Multi-stage tubes and their coaxial current returns were treated as smooth, coaxial cylinders of infinite length. On this assumption, the effects of interstage and stray capacitance were studied at length, and were found to dominate the design of such tubes.

During Phase II, particulars of high voltage, low inductance tube design were addressed. Some aspects of this work were direct; others required considerable investigation. In this section the results of this work are summarized. First, general design principles are considered. Then the results obtained for those aspects of the project that required extended study are discussed.

a. General Design Principles

(1) Box-Type Gradient Grids

Three straightforward approaches to the design of multi-stage tubes are the nested cup approach, the cavity-type gradient grid, and the box-type gradient grid. Nested cups become unwieldy when more than a few stages are required. Concentricity problems are severe, and the discharge diameter decreases as additional stages are added. The cavity-type grid structure is truly iterative, but by its nature, it results in a physically long (and hence high inductance) structure. The box grid is both iterative and physically short, and for this reason, the box grid approach was chosen for the high voltage, low inductance designs.

Box grids are not, however, free of design difficulties. Cavity grids are usually operated with a small resistor (typically 1 K) connected from each gradient grid to its corresponding gradient anode, i.e., across the cavity. The voltage drop across this resistor during commutation materially increases the field in the cavity during the commutation interval, promoting the commutation process. In the box-type grid, the region within the box is field-free except to the extent that the field in the interelectrode space penetrates the box through its apertures. Compared with field enhancement occurring during commutation within the cavity grid, that occurring within the

box grid is low. It follows, therefore, that optimizing the aperture geometry of box-type grids is critical for the realization of the best compromise between tube holdoff and commutation characteristics. Therefore, box grid and aperture geometry have been studied at length. The results of this investigation are discussed elsewhere in this section.

(a) Apertures

Various basic geometries are used for the grid apertures of hydrogen thyratrons. They range in complexity from a single circular hole to the multiple annular slots chosen for the tubes under consideration. For any given configuration, the apertures must be baffled such that there is no line of sight between alternate electrodes.

Annular apertures are preferred for low inductance tubes. The assumption is that since the discharge must pass through the apertures, it can be constrained by the aperture positions to occur only at the outer reaches of the tube. This is clearly the case under short pulse conditions since even a magnetically driven plasma will move only about 1 cm in 100 nS. Constraining the discharge to occur only in a large-diameter, thin sheet that is coaxial with the external current return minimizes the inductance of the tube/return combination, subject to the requirement that the current density be uniform around the circumference of the sheet.

The total aperture area for any given electrode or electrode baffle determines the maximum current that the element will pass before the discharge cuts off or "quenches."* For hydrogen and deuterium over a wide range of aperture shapes and sizes, the maximum current density before quenching has been determined experimentally to be about 10^4 A/in.² (1550 A/cm²) at typical thyratron gas pressures and pulse widths (400 microns, 10 μ S). The critical current density increases approximately linearly with increasing gas pressure and decreases with increasing pulse width to a minimum of about half its 10 μ S value when the pulse width exceeds 100 μ S. For pulse widths below 10 μ S,

*For multiple annular apertures, it is common to increase the slot width in that element having the smaller diameter slots to compensate for the area loss that would otherwise result.

the critical current density increases markedly. Quenching has not been observed in the submicrosecond region, and it is not considered as being a factor in the operation of the tubes under consideration.

For multiple box-grid tubes, the apertures can be conveniently offset in either of two ways as shown in Figure 1. In Figure 1(a), the apertures within any one box are in line with one another but offset with respect to those of an adjacent box. The experimental tubes built during Phase II were all of this design. In Figure 1(b), the apertures are offset within each box, and all boxes are identical. This arrangement offers manufacturing economy and should work in principle, although it has yet to be experimentally demonstrated.

(b) Baffles

It is convenient to be able to alter the holdoff/commutation properties of a box grid without altering its external dimensions, wall thickness, or aperture arrangement. One way to accomplish this is shown in Figure 2, where an internal baffle of thickness "T" has been positioned perpendicular to the axis of the slots. The baffle can be supported by a wall parallel to the slot axis as shown, since field plots have proved that the wall does not alter the field pattern in the box as long as it is at least a slot-width away from the edge of the slot. Increasing the ratio of the baffle thickness to the interior height of the box markedly reduces the penetration of the interelectrode field into the box.

The baffle has an additional advantage in that its proximity to the discharge should enhance the pulse rate capabilities of the tube by reducing the minimum diffusion path. This hypothesis was experimentally confirmed, as discussed later in this report.

(c) Stress Equalization

For short, low inductance tubes where the interstage spacers must be stressed to the limit of endurance, it is necessary that the stress be applied as uniformly as possible over the length of the insulator. Figure 3 shows the techniques used to accomplish this for simple cylindrical insulators and a box-grid design. In the lower stages of the tube, mechanical considerations regarding grid stiffness and mechanical stress relief tend to set the minimum

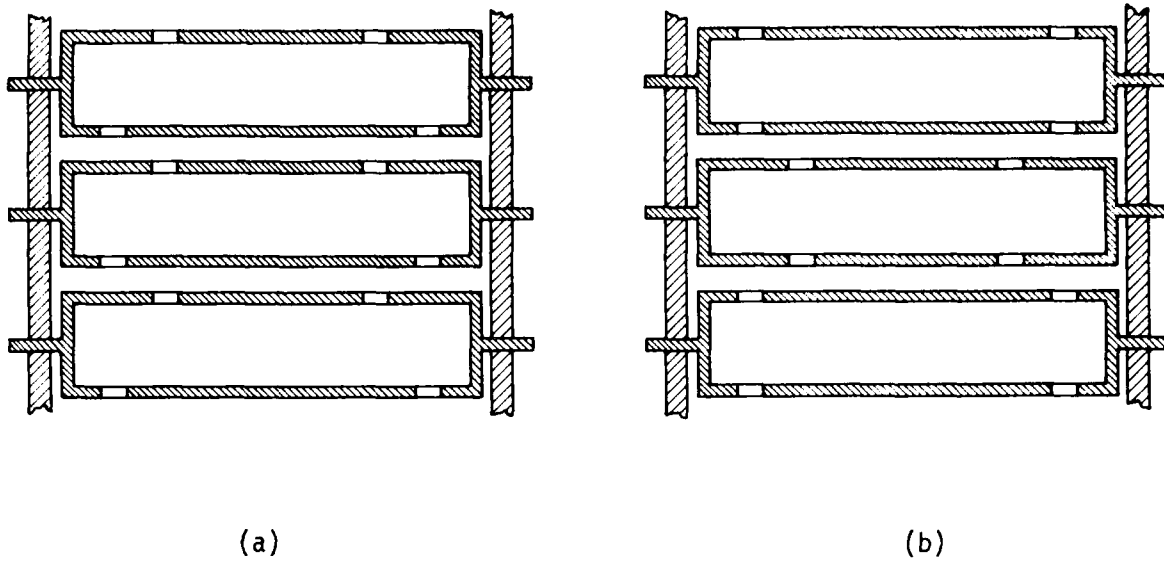


Figure 1. Typical aperture arrangements for box-type gradient grids. Type (a) is truly iterative and also economical since all boxes are identical.

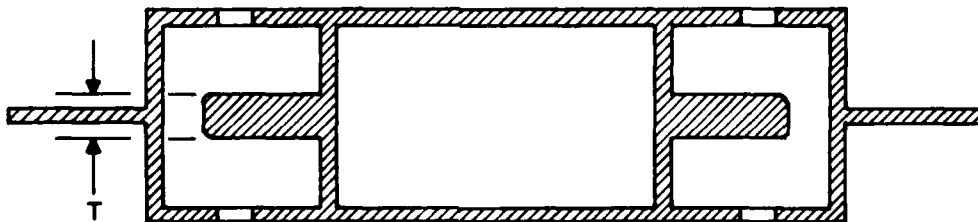


Figure 2. Internally baffled box-type grid. As baffle thickness T is increased, the isolation between adjacent gaps is increased.

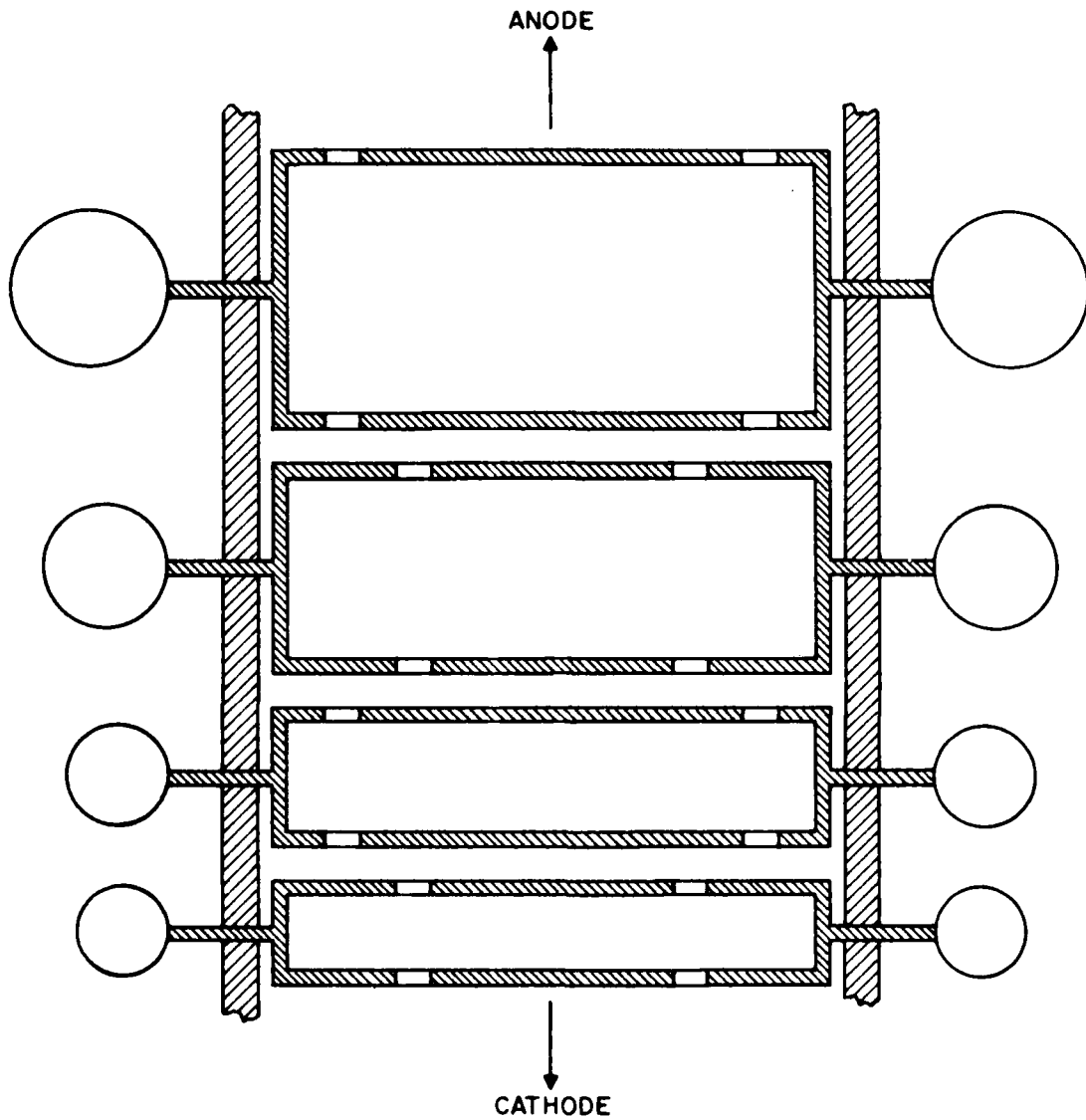


Figure 3. Basic configuration for minimizing insulator stress. The external equalizers minimize maximum stress in the insulators, but increase the stress in the medium external to the tube.

box height and, hence, the minimum insulator length. In the upper stages, the voltage stress in the insulator (both during dwell and commutation intervals) sets the minimum insulator length. To maintain the desired interelectrode spacing, the box height must be increased as the insulator length is increased. (The guard rings equalize the stress at the external surface; the required ring diameter increases as the insulator length increases.)

For the stage nearest the anode, the box height can be reduced and stress equalization maintained by resorting to the mechanism shown in Figure 52. The internal equalizer also serves to shield the ceramic from the discharge.

(2) Interstage and Stray Capacitance

The stage-to-stage distribution of the pulsed anode voltage will be most uniform when the ratio of interstage capacitance $C1$ to stage-to-return capacitance $C2$ is made large. Calculation of these capacitances is therefore an important aspect of low inductance, multi-stage tube design. Figure 4 schematically shows a section through a diameter of a typical stage. The insulator height, electrode spacing, E-E, and various diameters chosen for this example are typical of those used for the experimental tubes built during Phase II. Note from Figure 4 the use of stress-equalizing guard rings to minimize maximum stress in the ceramic insulator. As the ensuing discussion shows, the capacitance introduced by the rings is a significant component of the total interstage capacitance, and the effect of the rings must not be ignored.

There are four components to the total interstage capacitance that may be calculated as follows:

Electrode Capacitance

The electrodes are four inches in diameter and separated by 0.125 inch. The insulating medium is deuterium with a relative permittivity, ϵ_r , of unity. The electrode capacitance for parallel plates is

$$C_e = \epsilon_0 \epsilon_r A_e / d \quad (1)$$

where A_e is the area of the electrodes, d is the E-E spacing and ϵ_0 is the permittivity of free space. From Equation (1), $C_e = 22.6$ pF.

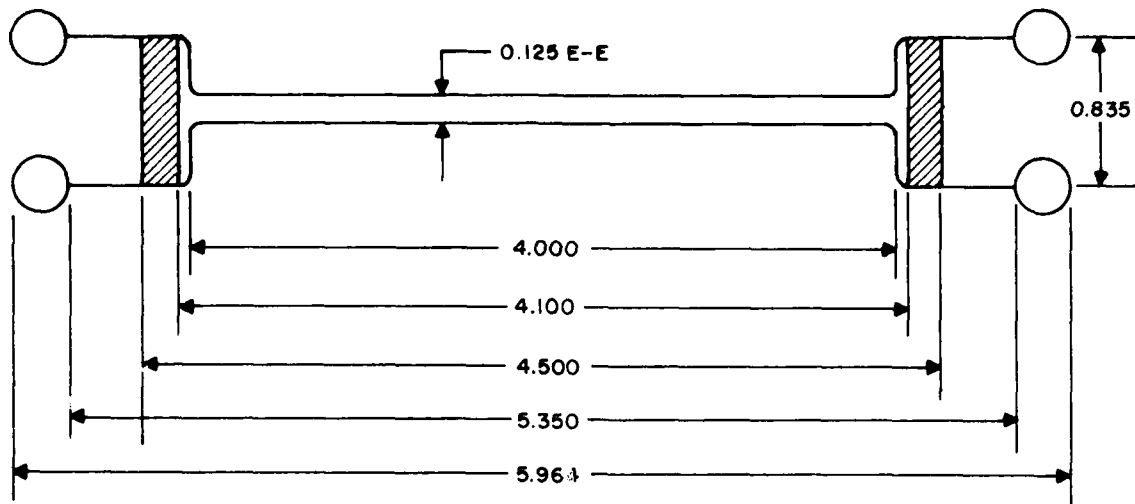


Figure 4. Model used to calculate interelectrode capacitance. In general, the capacitance introduced by the stress equalizers is a significant fraction of the total interstage capacitance.

Insulator Capacitance

The insulator is a ceramic annulus having an inner diameter of 4.100 inches and an outer diameter of 4.500 inches. It is 0.835 inch thick and has a relative permittivity of 9. Using Equation (1), where the appropriate area is that of the annulus and $d = 0.835$, insulator capacitance C_i is 6.54 pF.

Flange Capacitance

The flanges are an annulus having an inner diameter of 4.500 inches and an outer diameter of 5.350 inches. The insulating medium is oil ($\epsilon_r = 2.2$) and the flanges are separated by the insulator height, 0.835 inch. Again from Equation (1) flange capacitance C_f is 3.90 pF.

Guard Ring Capacitance

The capacitance of the guard rings can be approximated by treating them as being similar to a two-wire transmission line of length, L , where L is the mean circumference of the rings.* The per unit capacitance of a two-wire line is (1)

*When the capacitance is calculated on this basis, fringe fields are automatically taken into account.

$$C/L = \frac{\pi \epsilon_0 \epsilon_r}{\cosh^{-1}(d/2r)} \quad (2)$$

where C/L is the capacitance per unit length of the rings, d is the mean spacing between the rings, and r is the radius of the rings. Since approximately half the ring capacitance has been taken into account by the flange capacitance, the ring capacitance, Cr, can be estimated as C/2.

From Figure 4, d = 0.835 inch. Guard ring radius r is 0.1535 inch, and mean circumference L is 5.657 inches. Oil is the insulating medium between the rings, with $\epsilon_r = 2.2$. Substituting these values into Equation (2), C = 16.66 pF so Cr = 8.33 pF. Table 2 summarizes the results of the calculations.

Table 2. Calculated interstage capacitance for a typical box-grid assembly.

Component	Capacitance (pF)	% of Total
Electrodes, Ce	22.60	54.63
Insulator, Ci	6.54	15.81
Flanges, Cf	3.90	9.43
Guard Rings, Cr	<u>8.33</u>	<u>20.13</u>
Total, C1	41.37	100.00

Note from Table 2 that while the electrode capacitance dominates the total, the contributions due to the guard rings and insulators are significant.

To calculate stage-to-return capacitance C2, use the relation(2)

$$C2/d = \frac{2\pi\epsilon_0\epsilon_r}{\ln(b/a)} \quad (3)$$

where d is the stage length (0.835 inch), $\epsilon_r = 2.2$ for oil, b is the diameter of the current return, and a is the effective diameter of the tube. A typical current return diameter is 14 inches, but the effective stage diameter is not clearly identifiable. The effective diameter exceeds the 4.500-inch diameter of the insulator, but it is less than the 5.964-inch

outer diameter of the rings. The geometric mean of these diameters is 5.18 inches. Using this value for the effective stage diameter and the appropriate values for the remaining parameters, Equation (3) shows that $C2 = 2.61 \text{ pF}$.

The value of the ratio $C1/C2$ for a typical stage can now be found. For this example, it is $C1/C2 = 41.37/2.61 = 15.9$. This value for $C1/C2$ is sufficient to provide a reasonably uniform voltage division among the stages of a five-stage tube.

(3) Stage Voltage Addition

The work of Phase I showed that under pulse charge conditions, the stage voltages of a multi-stage tube are a function of ratio $C1/C2$, and that the upper stage bears a disproportionate share of the applied anode voltage. It follows that the dynamic breakdown voltage of the upper stage sets the maximum achievable epv for the tube, and that a point of diminishing returns exists as far as the number of stages is concerned. In general, the optimum number of stages increases with increasing $C1/C2$. When $C1/C2$ is very large, the stray capacitance loses significance. The voltage across each stage of an N -stage tube then approaches epv/N , and the optimum N is the minimum consistent with the desired epv and the DBV per stage.

It is implicit in the above discussion that the DBV for the individual stages be the same, and further, that the individual DBVs add algebraically as additional stages are operated in series. In practice, these constraints do not necessarily apply. Mechanical tolerances, imperfections in electrodes and insulators, deposits of cathode by-products, and density gradients in the tube can (and frequently do) result in differences in DBV among supposedly identical stages. Furthermore, the total DBV for a combination of stages in series is a strong function of the degree of baffling existing among them. This point is discussed at length later in this section, and also in connection with the experimental results. The implications of nonadditive DBV are illustrated below.

An expression for the anode breakdown voltage of a multi-stage tube can be derived in terms of the breakdown voltage of the weakest stage and the degree of isolation between adjacent stages.

Consider first the case where the applied voltage is distributed uniformly (or nearly so) among various stages of the tube. Let the breakdown voltage of the weakest stage (alone) be V_0 , and let the breakdown voltage of the combination consisting of the weakest stage in series with an adjacent stage be V_x . In the series case, the voltage across each stage (at breakdown) will be $V_x/2$.

Now define an isolation coefficient, α , as being the ratio of the voltage across the weakest stage at breakdown (series case) to the breakdown voltage of the weakest stage alone, i.e.,

$$\alpha = \frac{V_x}{2V_0} \quad (4)$$

The voltage across each series stage is $V_x/2 = \alpha V_0$, so for an N-stage device, the anode breakdown voltage will be

$$V_A = \alpha N V_0 \quad (5)$$

Equations (4) and (5) can be combined such that the anode voltage may also be expressed as

$$V_A = \frac{N}{2} V_x \quad (6)$$

For perfectly isolated stages, $\alpha = 1$, so from Equation (5), $V_A = N V_0$, i.e., the anode breakdown voltage will be N times the breakdown voltage of the weakest stage.

For a tube subjected to a nonuniform voltage distribution, the voltage across the weakest stage must not exceed αV_0 . In principle, the physical location of the weakest stage is arbitrary.* The anode breakdown voltage will be highest when the weakest stage is nearest the cathode, and lowest when the weakest stage is nearest the anode.

*In practice, the stage nearest the cathode is usually the weakest, due probably to contamination by cathode by-products or some low-level electron density.

Consider now two tubes that must operate at a given anode voltage, i.e., $(V_A)_1 = (V_A)_2$. From Equation (5)

$$\alpha_1(V_0)_1 N_1 = \alpha_2(V_0)_2 N_2 \quad (7)$$

If all individual stages of both tubes are physically identical, then (to a first approximation) the inductances of the tubes will be in proportion to their number of stages, i.e.,

$$\frac{(L_T)_1}{(L_T)_2} = \frac{N_1}{N_2} \quad (8)$$

Combining Equations (7) and (8),

$$\frac{(L_T)_1}{(L_T)_2} = \frac{\alpha_2(V_0)_2}{\alpha_1(V_0)_1} \quad (9)$$

For tubes where the breakdown voltage of the weakest stage is substantially the same, Equation (9) simplifies to

$$\frac{(L_T)_1}{(L_T)_2} = \frac{\alpha_2}{\alpha_1} \quad (10)$$

where the significance of achieving the highest isolation coefficient consistent with reliable commutation is at once obvious.

b. Extended Design Studies

(1) Box-Grid Geometry

Design of the gradient grids of a multi-stage tube is one of the most important aspects of tube design. The function of these grids is not only to grade the applied voltage across the tube, but to provide sufficient isolation between adjacent stages during the holdoff period, and yet not impede propagation of the triggering plasma during the commutation interval. In general these are inconsistent requirements, so compromises are necessary.

Until recently, only precedent and experimentation were available to aid in the design process. To design the multiple box grids required for high voltage, low inductance tubes, a more powerful technique was required. Therefore it was decided to model the box-grid structure and to use computer-generated field plots to predict how various grid designs would function relative to one another. By comparing the experimentally determined characteristics of a few such designs, and normalizing the computer results to the experimental data, the computer could then be used to generate such design deviations as might be required.

A transfer efficiency figure of merit, γ , has been devised where γ is defined as the ratio of the electric field at the center of the box to the electric field in the interelectrode space.* The transfer efficiency is readily calculable by computer in conjunction with a model for the grid. The model can be adapted to various geometries such as multiple, coaxial slots, offset and in-line slots within a given box, and boxes where internal baffles are employed. The basic approach is to assume that the ability of a box grid to hold off voltage (or conversely, to commutate through) depends on the extent to which the electric field in the adjacent gaps penetrates into the box through its apertures. When the field in the box is high (as would occur with wide apertures in a thin grid surface), the box can be expected to have poor holdoff characteristics but to commutate with relative ease. A box having narrow apertures in thick surfaces would have relatively low internal fields. Such a grid would be expected to provide good isolation between gaps but to inhibit the propagation of the triggering plasma during the commutation interval.

*It might be argued that the electric field just within the apertures might be a better measure of a given grid's characteristics. However, defining the transfer efficiency in terms of this field would complicate the calculation without materially increasing the understanding of how box grids should be designed. At present it is sufficient to be able to establish a unique numerical value for γ that depends only on the geometry of the grids.

Figure 5 is a computer-generated field plot (equipotentials) for a symmetrical box grid. (It is necessary to consider two gaps in order to determine the field in the box.) Figure 6 shows (on an expanded scale) the equipotentials within the box, and that the field at the center of the box is about 0.01% of the field in the interelectrode region. Figure 7 is a similar plot where the aperture width was increased to 0.150 inch, as opposed to the 0.125-inch width of Figure 6. From Figure 7 the 20% increase in aperture width doubles the electric field at the center of the box. Figure 8 shows the situation when the slot width is reduced to 0.075 inch. In this case field penetration has been greatly reduced, suggesting that commutation through such a grid would be relatively difficult.

Internal gradient grid baffles are useful mechanisms for establishing grid transfer efficiency. Consider Figure 9 which shows the field pattern in a box where a wall that is parallel to the electric field has been added. The wall has been positioned one slot-width away from the inner edge of the slot, and the outer edge of the slot is one slot-width away from the inner surface of the outer grid wall. As a result of this geometry, the field pattern is symmetrical with respect to the axis of the slots, and it can be shown that the pattern is essentially the same as that which would result if neither wall were present.

Consider Figure 10 which shows the effect of adding a symmetrically positioned baffle that is perpendicular to the electric field. A comparison of Figures 9 and 10 shows that the baffle has reduced the field at the grid midpoint by about a factor of four. Figure 11 shows the field pattern when a relatively thick baffle is employed. The thick baffle reduces the field by an additional factor of ten.

To appreciate the power of the field plotting technique, consider first Figure 12 which shows a baffled gradient grid design that is likely to be of considerable value in the design and construction of practical tubes. The apertures within a given box are offset such that when identical grids are properly stacked, the apertures between adjacent grids are automatically offset. Identical grids can thus be used as building blocks in an iterative structure. The various dimensions shown and defined in Figure 12 are typical of a practical tube and constitute a baseline design. Figure 13 shows the

effects on the transfer efficiency of the grid structure of Figure 12 when certain deviations are made from the baseline design. The slopes of the curves show the sensitivity of the transfer efficiency to changes in the parameters being varied.

Figure 14 depicts the calculated transfer efficiency for the structure of Figure 12 when selected dimensions are maintained constant at convenient values and others are changed from their baseline values. The objectives of this exercise were to establish a baseline design having $\gamma \approx 10^{-4}$ and then to investigate its sensitivity to readily made changes in the structure of the grid. (The significance of $\gamma = 10^{-4}$ is shown below.)

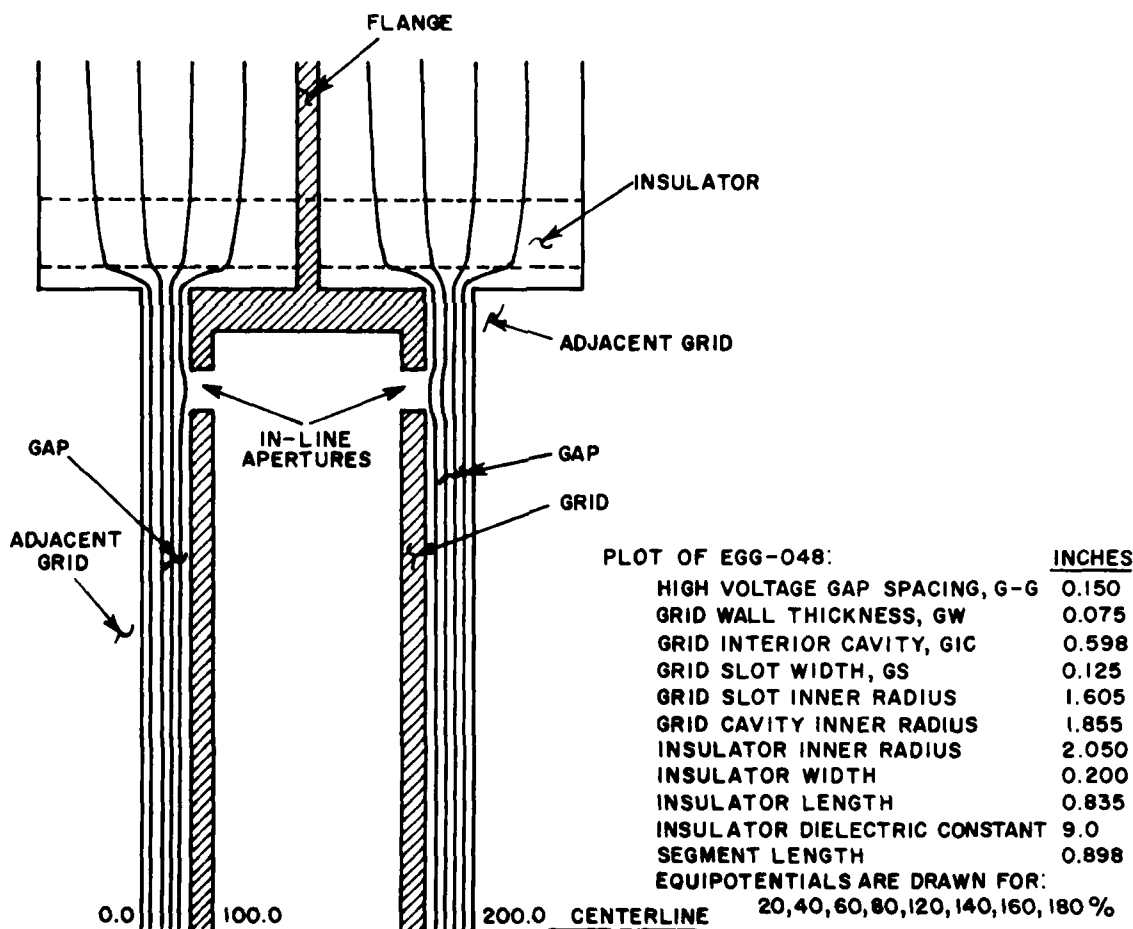
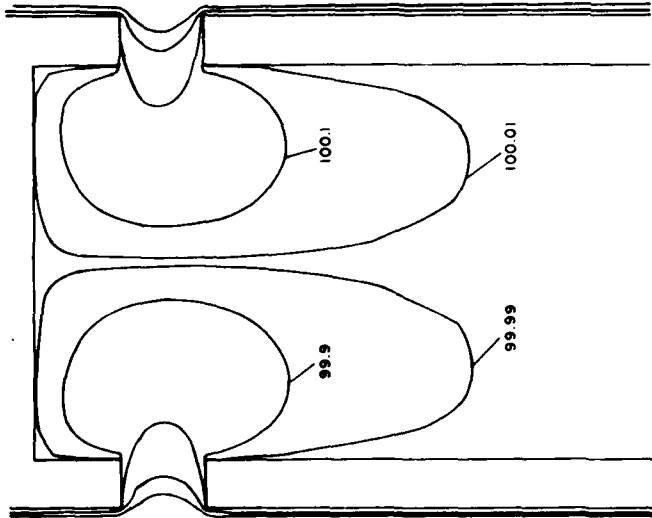


Figure 5. A typical computer-generated field plot. Two gaps must be considered to establish the field pattern in the box.

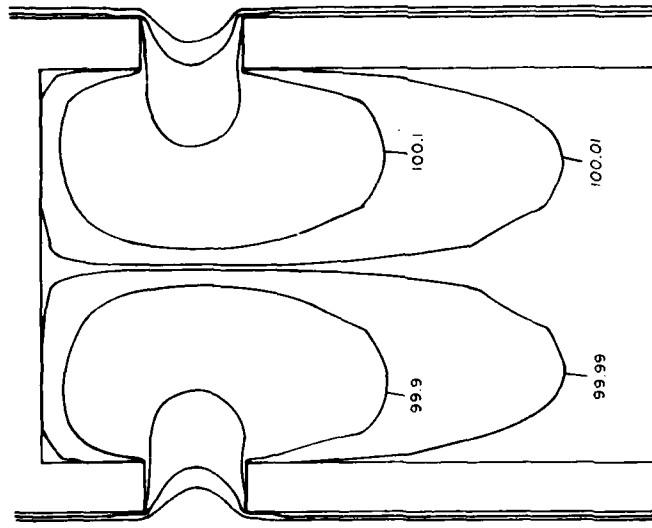


PLOT OF EGG-048: EXPANDED VIEW GRID SLOT REGION

	INCHES
HIGH VOLTAGE GAP SPACING, G-G	0.150
GRID WALL THICKNESS, GW	0.075
GRID INTERIOR CAVITY, GIC	0.598
GRID SLOT WIDTH, GS	0.125
GRID SLOT INNER RADIUS	1.605
GRID CAVITY INNER RADIUS	1.855
INSULATOR INNER RADIUS	2.060
INSULATOR WIDTH	0.200
INSULATOR LENGTH	0.835
INSULATOR DIELECTRIC CONSTANT	9.0
SEGMENT LENGTH	0.898

EQUIPOTENTIALS ARE DRAWN FOR:
 90, 95, 99, 99.9, 99.99, 100.01
 100.1, 101, 105, 110%

Figure 6. An expanded view of the equipotentials within the box grid of Figure 5. As long as the slots are at least a slot-width away from the wall, the wall exerts no significant influence over the field along the slot axis.

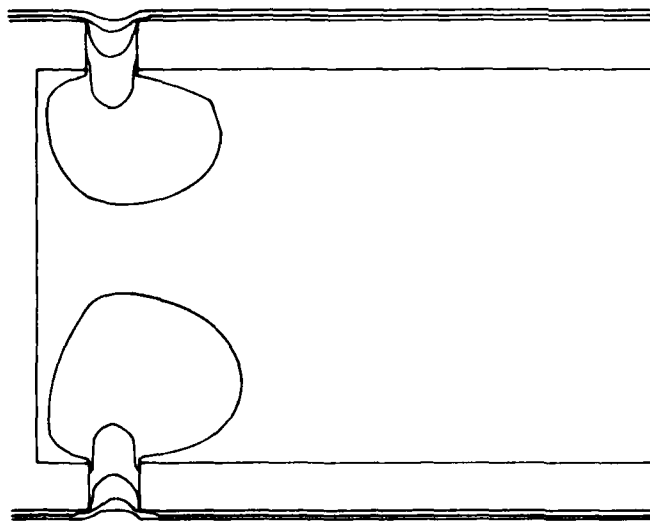


PLOT OF EGG-049: EXPANDED VIEW GRID SLOT REGION

	INCHES
HIGH VOLTAGE GAP SPACING, G-G	0.150
GRID WALL THICKNESS, GW	0.075
GRID INTERIOR CAVITY, GIC	0.598
GRID SLOT WIDTH, GS	0.150
GRID SLOT INNER RADIUS	1.555
GRID CAVITY INNER RADIUS	1.855
INSULATOR INNER RADIUS	2.050
INSULATOR WIDTH	0.200
INSULATOR LENGTH	0.835
INSULATOR DIELECTRIC CONSTANT	9.0
SEGMENT LENGTH	0.898

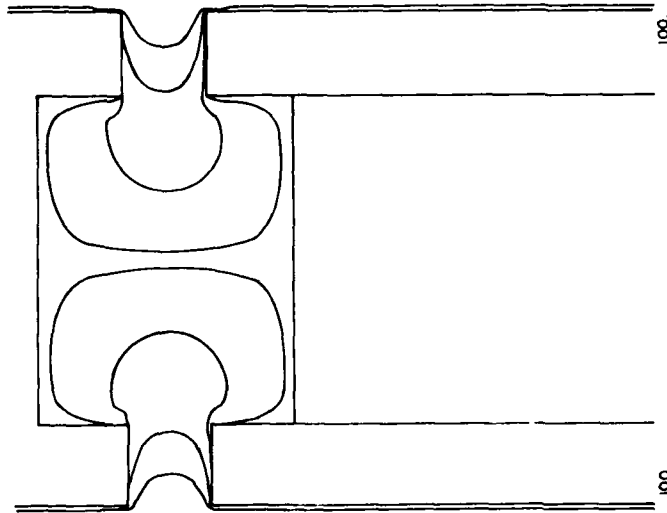
EQUIPOTENTIALS ARE DRAWN FOR:
 90, 95, 99, 99.9, 99.99, 100.01
 100.1, 101, 105, 110%

Figure 7. Effect of increasing slot-width by 20% (vs Figure 6). The field intensity midway between the slots has been doubled.



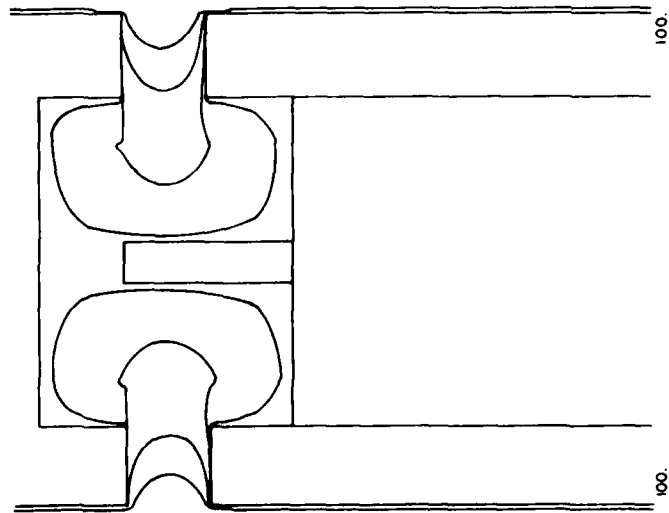
PLOT OF EGG-051: EXPANDED VIEW GRID SLOT REGION
 HIGH VOLTAGE GAP SPACING, G-G 0.150
 GRID WALL THICKNESS, GW 0.075
 GRID INTERIOR CAVITY, GIC 0.598
 GRID SLOT WIDTH, GS 0.075
 GRID SLOT INNER RADIUS 1.705
 GRID CAVITY INNER RADIUS 1.855
 INSULATOR INNER RADIUS 2.050
 INSULATOR WIDTH 0.200
 INSULATOR LENGTH 0.835
 INSULATOR DIELECTRIC CONSTANT 9.0
 SEGMENT LENGTH 0.898
 EQUIPOTENTIALS ARE DRAWN FOR:
 90, 95, 99, 99.9, 99.99, 100.01
 100.1, 101, 105, 110 %

Figure 8. Effect of reducing slot-width by 40% (vs Figure 6). The field intensity at the mid-point has been greatly reduced.



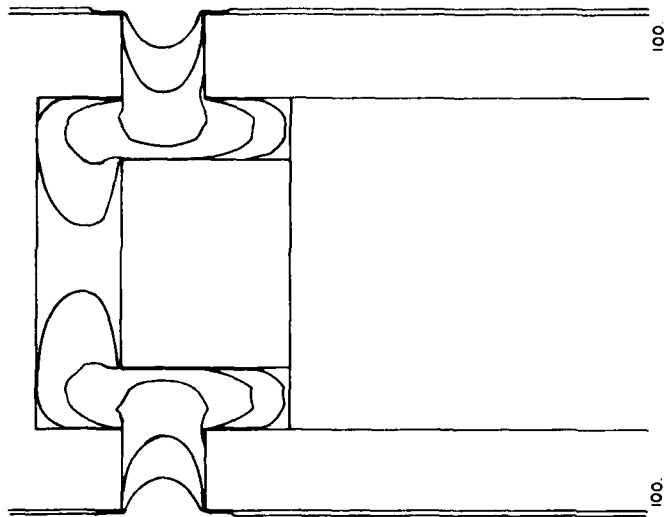
PLOT OF EGG-060: EXPANDED VIEW GRID SLOT REGION
 SAME CONDITIONS AS IN EGG-040 EXCEPT THE GRID INTERIOR CONTAINS A BAFFLE ELEMENT.
 EQUIPOTENTIALS ARE DRAWN FOR:
 95, 99, 99.90, 99.99,
 100.01, 100.1, 101, 105 %

Figure 9. A typical field pattern for a double-walled box grid. The field midway between the apertures is essentially the same as it would be if neither wall were present.



PLOT OF EGG-062: EXPANDED VIEW GRID SLOT REGION
 SAME CONDITIONS AS IN EGG-040 EXCEPT THE
 GRID INTERIOR CONTAINS A BAFFLE ELEMENT.
 BAFFLE INNER RADIUS = 1.480 INCH
 BAFFLE WIDTH = 0.063 INCH
 EQUIPOTENTIALS ARE DRAWN FOR:
 95, 99, 99.90, 99.99,
 100.01, 100.1, 101, 105%

Figure 10. Field pattern when a thin baffle is added to the grid of Figure 9. The field is reduced by about a factor of 4.



PLOT OF EGG-061: EXPANDED VIEW GRID SLOT REGION
 SAME CONDITIONS AS IN EGG-040 EXCEPT THE
 GRID INTERIOR CONTAINS A BAFFLE ELEMENT.
 BAFFLE INNER RADIUS = 1.480 INCH
 BAFFLE WIDTH = 0.311 INCH
 EQUIPOTENTIALS ARE DRAWN FOR:
 95, 99, 99.90, 99.99, 99.999, 100.001,
 100.01, 100.1, 101, 105%

Figure 11. Field pattern when a thick baffle is added to the grid of Figure 9. The field is reduced by about a factor of 40.

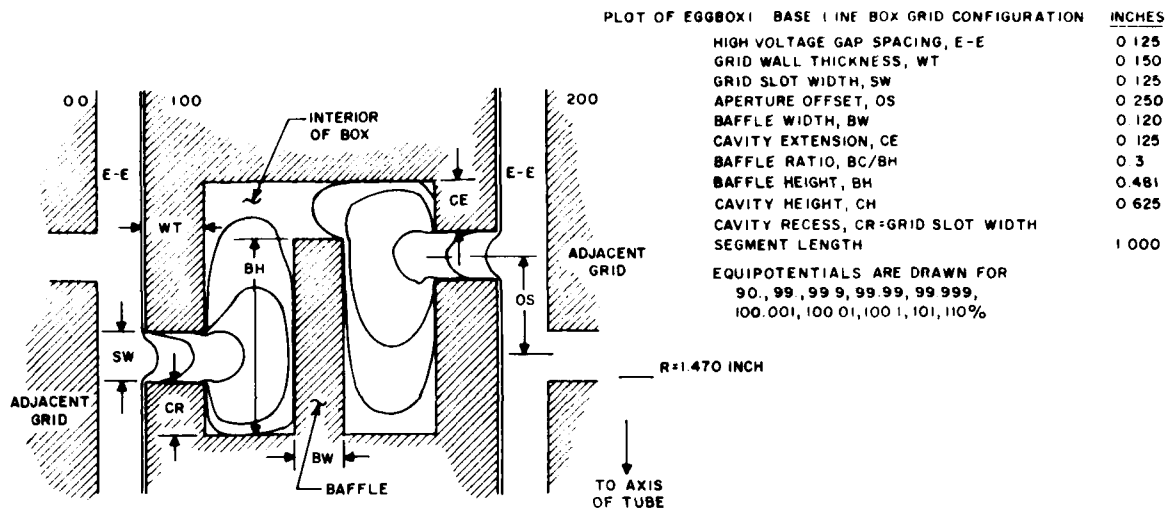


Figure 12. A baffled box-grid where the slots are offset within the box. This configuration may be of considerable value in the construction of practical tubes.

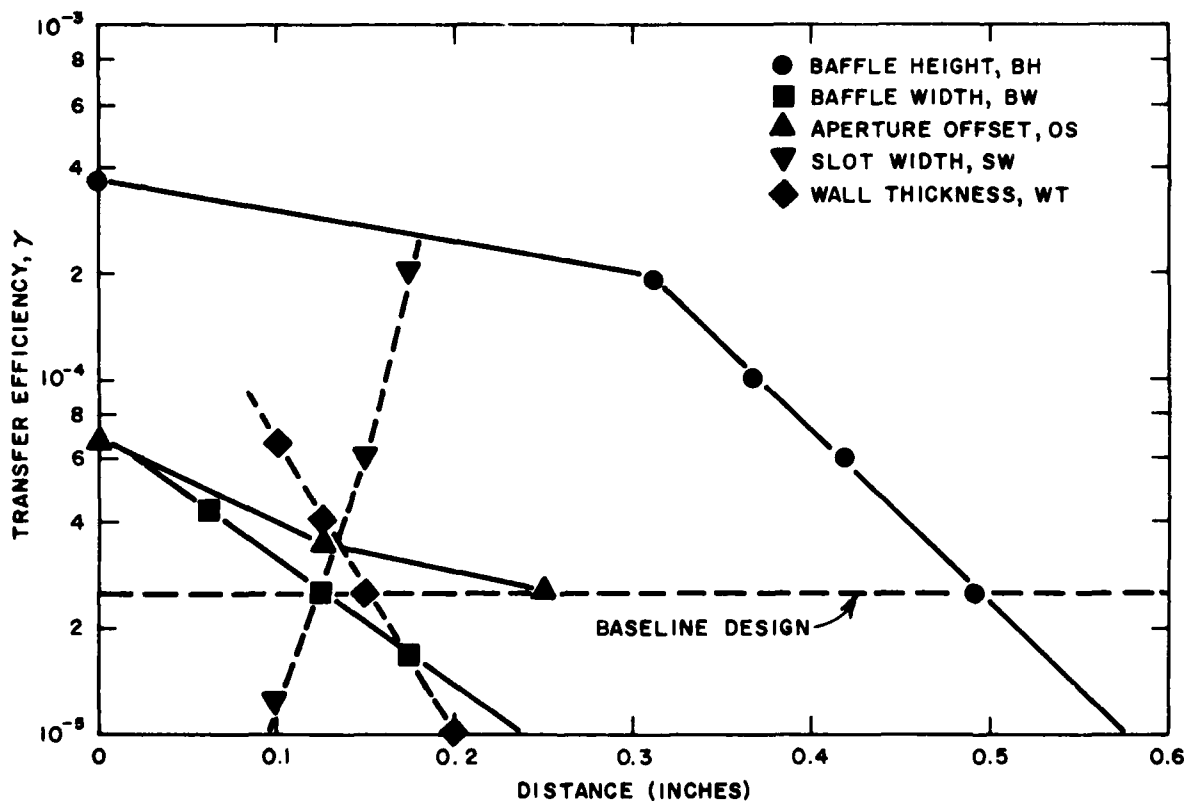


Figure 13. Results of a typical box-grid parametric study. Each curve intersects the transfer efficiency corresponding to the baseline design at that dimension corresponding to its value in the baseline design.

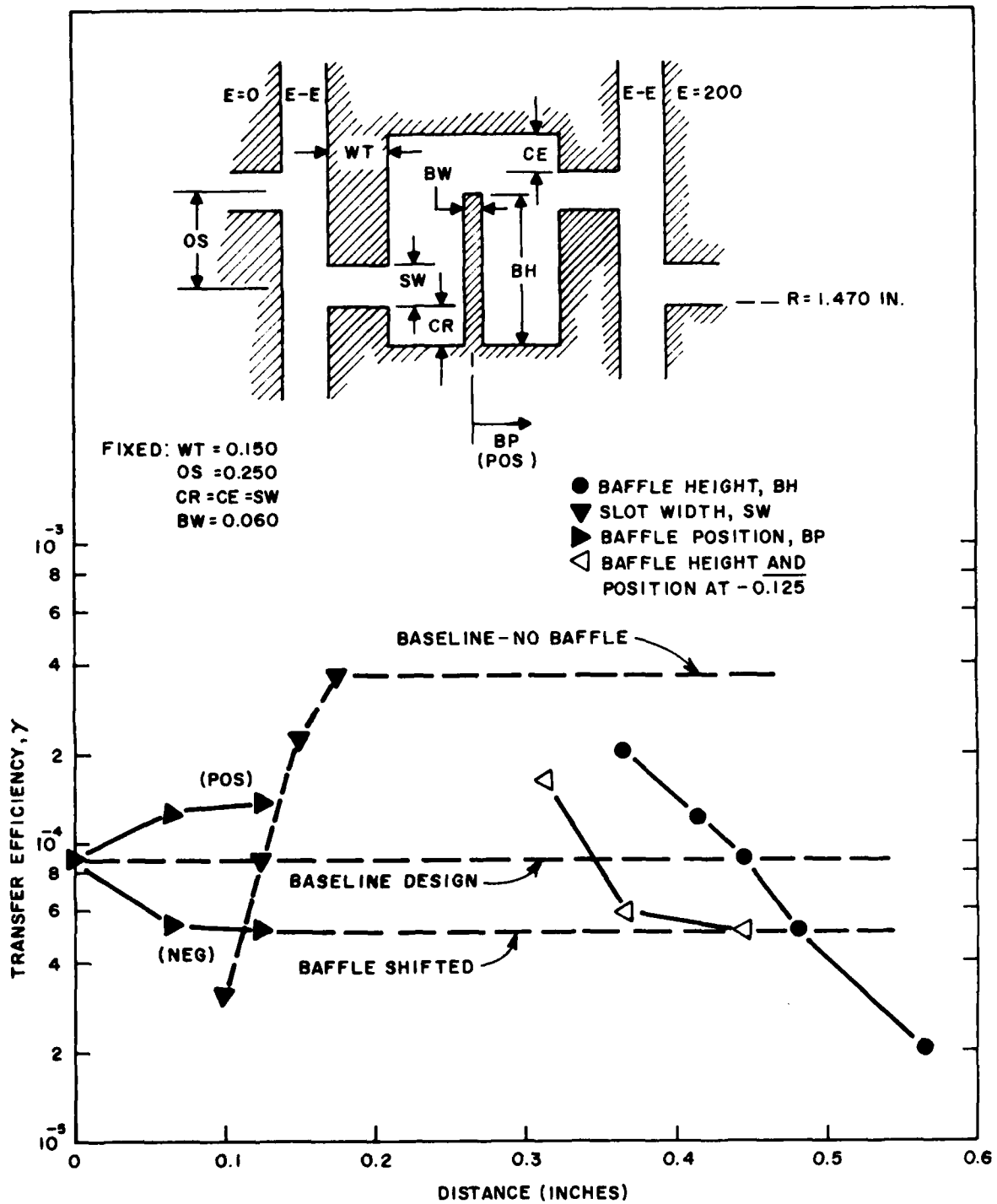


Figure 14. Results of a parametric study performed to investigate the sensitivity of the transfer efficiency to the dimensions and location of the grid baffle. The baseline transfer efficiency is about 10^{-4} - the near-optimum value.

The value of the computer field plotting technique lies in its power to investigate on paper the effects of design changes that would require enormous time and money to investigate experimentally. However, experimentation is still required to establish that value for the transfer efficiency that provides the best compromise between stage voltage addition and commutation characteristics. When this value for the efficiency is determined, field plotting can then be used to aid in the design of a grid structure that provides the necessary efficiency while simultaneously meeting the constraints imposed by the need for structural integrity and manufacturing efficiency.

Figure 15 gives the results of an attempt to correlate the calculated transfer efficiencies and the measured isolation coefficients for three experimental multi-stage tubes. The efficiencies were determined by exactly modeling the grid structure of each of the tubes, and the isolation coefficients were determined from experimental data. From Figure 15 it is clear that a transfer efficiency of 10^{-4} is required to obtain good stage voltage addition.*

However, what constitutes a condition of optimum transfer efficiency has yet to be determined. To date, only field ratio γ has been considered. It may be that a more meaningful parameter is the absolute field at either the center of the box or just inside the apertures. Furthermore, it may be that the transfer efficiency should be different for stages subjected to different fields when the tube commutates. For the upper stage of an N-stage tube, the ratio of the field during commutation to the field during charging and holdoff approaches N:1,** while for the lower stage, this ratio is unity. This suggests that it might be good to increase the transfer efficiency of the upper stages to promote the spread of the triggering plasma in those stages most likely to arc, although to do so would reduce the voltage addition properties of those stages where voltage addition is most beneficial.

*Without experimental work, the lower limit for the transfer efficiency cannot be determined. At $\gamma = \gamma(\min)$, a tube would have good stage voltage addition but it would not readily commutate. The only practical value in knowing $\gamma(\min)$ is that it would then be possible to determine the best possible stage voltage addition.

**The ratio is not exactly N:1 because of the capacitance-controlled voltage distribution.

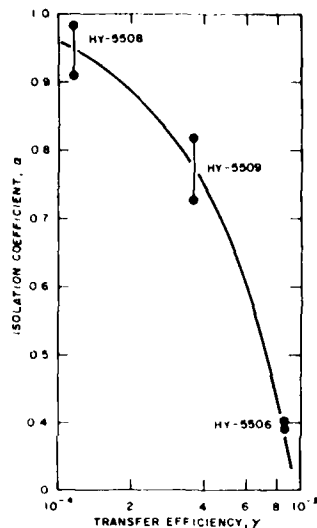


Figure 15. Relationship between isolation coefficient and transfer efficiency. The transfer efficiencies were calculated from field plots; the isolation coefficients were experimentally determined. A transfer efficiency of 10^{-4} provides near-perfect stage voltage addition.

It is thus clear that experimental work will be required to develop a firm understanding of those factors that determine the best combination of applied field and transfer efficiency.

(2) Anode Dissipation

Significant anode dissipation can occur during the commutation interval of any hydrogen thyratron, and anode damage is likely to be severe for tubes operated at high voltage, high di/dt , and high prr. During commutation, with the anode voltage falling but still high, the rising anode current is comprised of a stream of high energy electrons that strike the anode surface. The energy of these electrons is dissipated as heat, and the heating is proportional to the time integral of the instantaneous anode voltage and the instantaneous anode current. Under conditions where the anode fall time and the current rise time are comparable, i.e., high di/dt operation, the time scale is such that thermal conduction can neither cause heat to diffuse into the anode nor spread over its surface, so even liquid cooling of the anode offers no relief from the effects of the localized heating. Therefore, the anode surface at the point of impact (generally in line with the apertures of the grid nearest the anode) is flashed to the vaporization point at the beginning of each current pulse.* A buildup of vaporized anode material,

*Any filamentation or beam formation in the discharge (as may occur under high voltage, high di/dt conditions) can serve only to increase the anode damage.

either within the grid-anode space or on the inner surface of the grid-anode insulator, can serve ultimately to lower tube holdoff capability. Eventually the high speed electrons can erode the anode sufficiently to drill it through, such that the tube goes to air. Thus it occurs that although the fundamental limit on the pulse repetition rate is set by the time required for the tube to deionize and recover voltage holdoff, average anode heating and/or a reasonable anode life may limit the maximum prr to some lower value.*

To calculate the anode dissipation to be expected during the commutation interval, the switch model devised during Phase I was used.** This model is based on the assumption that any gas discharge switch undergoing commutation can be considered as a voltage source in series with the switch inductance. The polarity of the source is such that it acts to inhibit the rise of the discharge current. The instantaneous source voltage is

$$e(t) = V_0 (2 - e^{t/\tau_i}) \quad (11)$$

where V_0 is the voltage across the switch just prior to commutation, and τ_i is the time constant of the anode fall. It is assumed that τ_i depends solely on the gas pressure within the switch. Observation of the anode fall time of several types of gas discharge switches reveals that over nine decades of pressure, τ_i can be approximated by the relation

$$\tau_i = 23P^{-0.42} \quad (\text{nanoseconds}) \quad (12)$$

where P is the switch pressure in torr.*** Time constant τ_i would be that corresponding to the anode fall time if the switch inductance were zero, and it is in fact that observed when di/dt is low.

*Under high RMS conditions, resistive losses in the cathode usually determine the maximum prr. Under long pulse conditions, the average heating in the plasma column is usually the limiting factor. It seldom arises that the maximum achievable prr approaches that determined by deionization and recovery.

**The model is described in the Final Report for Phase I.

***Equation (12) can be inferred from Figure 2 of the Final Report for Phase I.

Equation (11) is assumed to apply over the interval $0 < t < \tau_i \ln 2$. Note that at $t = 0$, $e(t) = V_0$. At $t = \tau_i \ln 2$ (defined as $t = T$), $e(t) = 0$. Thus the "steady-state" tube drop is ignored and it is further defined that $e(t) = 0$ for $t > T$; i.e., Equation (11) does not apply for the post-commutation period. A plot of Equation (11) (normalized) is shown in Figure 16.

Hydrogen thyratrons operate over the approximate pressure range of 0.2 to 0.8 torr. Corresponding values for τ_i are 45 to 25 nS, and for T , 31 to 17 nS.

The term "resistive fall time" has been coined to refer to the pressure-dependent component of the anode fall.

The resistive anode fall time, T , will not in fact be measurable for a tube being operated at high di/dt because the instantaneous anode voltage is the sum of the voltage $e(t)$ and the voltage drop $L_T di/dt$, where L_T is the effective inductance of the tube and its current return. Under high di/dt conditions, the inductive component is significant.

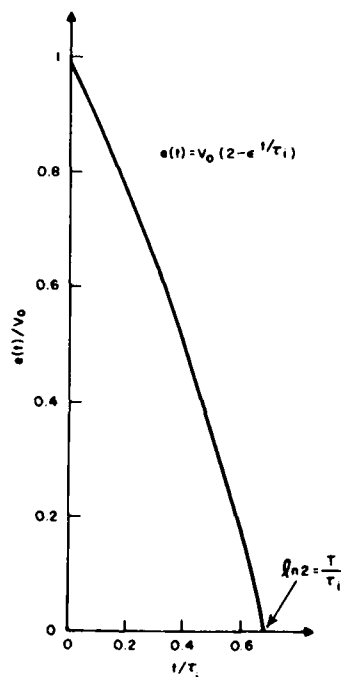


Figure 16. Waveform assumed for the anode fall. At $t = \tau_i \ln 2$, the anode potential is zero.

To calculate anode dissipation, the model to calculate circuit current $i(t)$ during the commutation interval was used. Then the integral of the volt-ampere product (using the resistive voltage only) was evaluated to obtain the energy deposited at the anode. Thus

$$W = \int_0^T e(t) i(t) dt \quad (13)$$

from which the dissipation in watts is readily determined.

Worst-Case Commutation Loss

The maximum anode dissipation possible occurs when the total circuit inductance is negligible, i.e., when the circuit time constant $L/R \ll \tau_i$. Under this condition the rise time of the anode current is limited only by the anode fall. Consider the circuit of Figure 17(a) where a thyratron is used to discharge a transmission line into a resistive load. Assume that the two-way travel time of the line is greater than total anode fall time T , and assume further that the stray inductance is zero. The circuit of Figure 17(b) applies during the commutation interval. The discharge current is

$$i(t) = \frac{1}{R} [V_0 - e(t)] \quad (0 \leq t \leq T) \quad (14)$$

From Equation (11)

$$\begin{aligned} i(t) &= \frac{1}{R} [V_0 - V_0 (2 - e^{t/\tau_i})] \\ &= \frac{V_0}{R} (e^{t/\tau_i} - 1) \end{aligned} \quad (15)$$

Note that at $t = 0$, $i(t) = 0$, while at $t = \tau_i \ln 2 = T$, $i(t) = V_0/R = ib$.

From Equation (13)

$$W = \int_0^{\tau_i \ln 2} V_0 (2 - e^{t/\tau_i}) \cdot \frac{V_0}{R} (e^{t/\tau_i} - 1) dt \quad (16)$$

Performing the integration of Equation (16) gives

$$W = 0.1137 \frac{V_0^2}{R} \cdot \tau_i \quad (17)$$

or, since $\frac{V_0}{R} = ib$ and $V_0 = epy$

$$W = 0.1137 epy \cdot ib \cdot \tau_i \quad (18)$$

The dissipation in watts is simply

$$P_A = 0.1137 epy \cdot ib \cdot \tau_i \cdot prr \quad (19)$$

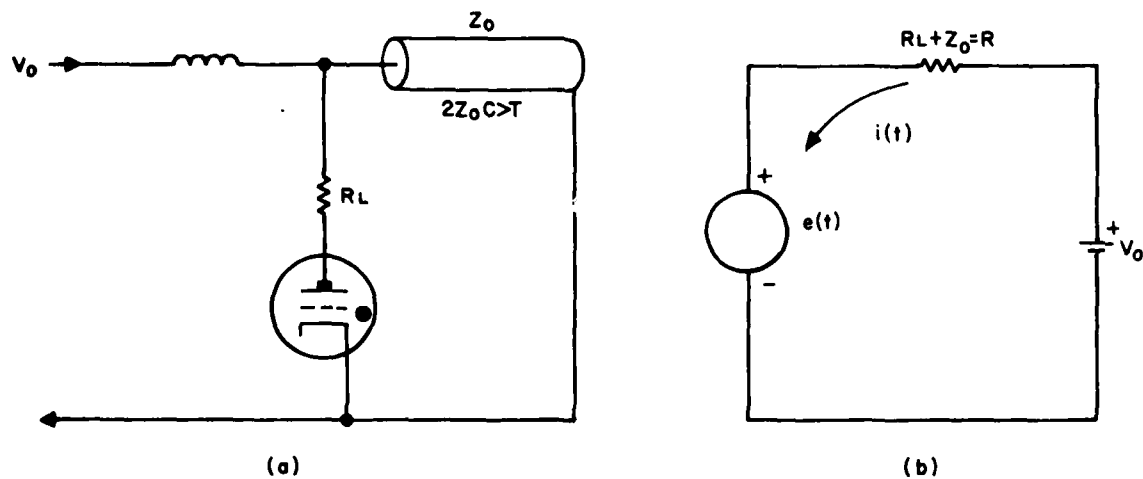


Figure 17. Circuits for a thyatron discharging a transmission line into a resistive load. Voltage $e(t)$ opposes the rise of the discharge current.

Assume that $e_{py} = 250$ kV and $i_b = 20$ kA. A typical value of τ_i at high pressure is 25 nS. Equation (19) gives the anode dissipation to be 125 watts per hertz. Even if the ionization time constant could be reduced by an order of magnitude, the anode dissipation would still be 12.5 kW per kHz; thus, some value of stray inductance is desirable to limit P_A .

Switching Efficiency

A straightforward expression for the switching efficiency and an expression for the ratio of the commutation loss to the steady-state loss can easily be derived.

Assume that the efficiency is not too bad, i.e., most of the energy stored in the line eventually is delivered to the load, i.e., $W_{Line} \approx W_{Load}$. Assume also that the load is matched to the line, i.e., $R_l = Z_0 = R/2$. The load voltage (after commutation and neglecting the steady-state tube drop) is thus $e_{py}/2$, and the load current is i_b . The energy delivered to the load is thus

$$W_{Load} = 1/2 e_{py} \cdot i_b \cdot t_p \quad (20)$$

where t_p is the pulse width. By assumption of a reasonable efficiency, this is also the energy stored in the line.

The energy lost in the conducting tube is

$$W_S = e_{td} \cdot i_b \cdot t_p \quad (21)$$

where e_{td} is the steady-state tube drop.

The worst-case commutation loss is given by Equation (18) as $W_C = 0.1137 e_{py} \cdot i_b \cdot \tau_i$, where the subscript has been added to distinguish between the conduction loss and the commutation loss. The tube loss, W_T , is the sum of the two losses, i.e.,

$$\begin{aligned}
 W_T &= W_S + W_C \\
 &= 0.1137 \text{ epy} \cdot \text{ib} \cdot \tau_i + \text{etd} \cdot \text{ib} \cdot \text{tp}
 \end{aligned} \tag{22}$$

Combining Equations (20) and (22),

$$\begin{aligned}
 W_T/W_{\text{Load}} \approx W_T/W_{\text{Line}} &= \frac{0.1137 \text{ epy} \cdot \text{ib} \cdot \tau_i + \text{etd} \cdot \text{ib} \cdot \text{tp}}{1/2 \text{ epy} \cdot \text{ib} \cdot \text{tp}} \\
 &= 2 \left(0.1137 \frac{\tau_i}{\text{tp}} + \frac{\text{etd}}{\text{epy}} \right)
 \end{aligned} \tag{23}$$

The switching efficiency, ϵ , is simply $1 - W_T/W_{\text{Line}}$, or

$$\epsilon = 1 - 2 \left(0.1137 \frac{\tau_i}{\text{tp}} + \frac{\text{etd}}{\text{epy}} \right) \tag{24}$$

As epy is increased, both the energy storage and the commutation loss increase as epy^2 , while the conduction loss increases only proportionally to epy. At high epy, Equation (24) may be simplified to

$$\epsilon \approx 1 - 0.227 \frac{\tau_i}{\text{tp}} \tag{25}$$

For a typical case where $\tau_i = 25 \text{ nS}$ and $\text{tp} = 100 \text{ nS}$, Equation (25) yields $\epsilon = 94.3\%$. Assuming $\text{etd} \approx 30 \text{ volts/cm}$ and $\text{epy} \approx 20 \text{ kV/cm}$ (for low inductance designs), and applying Equation (24) with $\tau_i = 25 \text{ nS}$ and $\text{tp} = 100 \text{ nS}$, a switching efficiency of 94.0% is computed.

Commutation Loss — Transmission Line with Stray Inductance

Assume that the circuit of Figure 17 is modified to include a finite stray inductance, L , that includes the inductance of the tube. Using the tube model, it can be shown that the circuit current during the commutation interval is given by(3)

$$i(t) = \frac{ep\gamma}{R} [K_A e^{t/\tau_i} + (1 - K_A) e^{-t/\tau_L} - 1] \quad (26)$$

where $R = R_1 + Z_0$, $\tau_L = L/R$ and $K_A = \tau_i/(\tau_i + \tau_L)$.

Combining Equations (11), (13), and (26), the anode energy deposit is written as

$$W_C = \frac{ep\gamma^2}{R} \int_0^{\tau_i \ln 2} (2 - e^{t/\tau_i}) [K_A e^{t/\tau_i} + (1 - K_A) e^{-t/\tau_L} - 1] dt \quad (27)$$

Performing the integration of Equation (27),

$$W_C = \frac{ep\gamma^2}{R} \cdot \tau_i \left\{ \frac{K_A}{2} + 1 - \ln 4 - \frac{2(1 - K_A)^2}{K_A} \left[\frac{-K_A}{2(1 - K_A)} - 1 \right] - \frac{(1 - K_A)^2}{(1 - 2K_A)} \left[\frac{1 - 2K_A}{2(1 - K_A)} - 1 \right] \right\} \quad (28)$$

Equation (28) is the general expression for the anode energy during commutation when a gas discharge switch discharges a long transmission line into a resistive load.* It is convenient to replace the cumbersome expression shown within braces in Equation (28) with the simple expression $f(K_A)$. Equation (28) then becomes

$$W_C = \frac{ep\gamma^2}{R} \cdot \tau_i \cdot f(K_A) \quad (29)$$

*As τ_L approaches zero, K_A approaches unity. Taking the limit of Equation (28) as K_A approaches unity yields $W_C = 0.1137 \frac{ep\gamma}{R} \cdot \tau_i$. This is consistent with the worst-case anode energy as given by Equation (17).

Equation (29) shows that W_c is proportional to the product $\tau_i \cdot f(K_A)$, and it is clear that parameter K_A is important. A plot of $f(K_A)$ is shown in Figure 18.

The function $f(K_A)$ changes character at $K_A = 0.5$ ($\tau_i = \tau_L$), and increases rapidly with increasing K_A .* This is (more or less) the boundary between low di/dt ($\tau_L > \tau_i$) and high di/dt ($\tau_L < \tau_i$) operation.

Equation (17) may be rewritten as

$$W_c = 0.1137 \frac{e p y^2}{R} \cdot \tau_i \quad (30)$$

Dividing Equation (29) by Equation (30) gives

$$\beta = 8.795 f(K_A) \quad (31)$$

where β is the ratio of the anode energy with inductance in the circuit to the anode energy with no inductance in the circuit. Equation (31) is shown in Figure 19.

Consider a case where $K_A = 0.1$ ($\tau_L = 9\tau_i$). By arbitrary definition, this is a condition of low di/dt . If this condition is used as a base and it corresponds to one unit of anode energy, K_A can then be increased and the corresponding increases in the anode energy can be observed. Figure 20 shows the results of such a calculation. Note from Figure 20 that increasing K_A from 0.1 to 0.5 ($\tau_i = \tau_L$, arbitrary boundary) increases the anode energy by a factor of 7.9, and enters the high di/dt regime. As the inductance is decreased toward zero, τ_L approaches zero, and K_A approaches unity. At $K_A = 1$, it is calculated that there is over fifty times the anode energy corresponding to the low di/dt case.

*At $K_A = 0.5$, the last term of K_A is an indeterminate form. It can be shown that at $K_A = 0.5$, $f(K_A) = 0.017$.

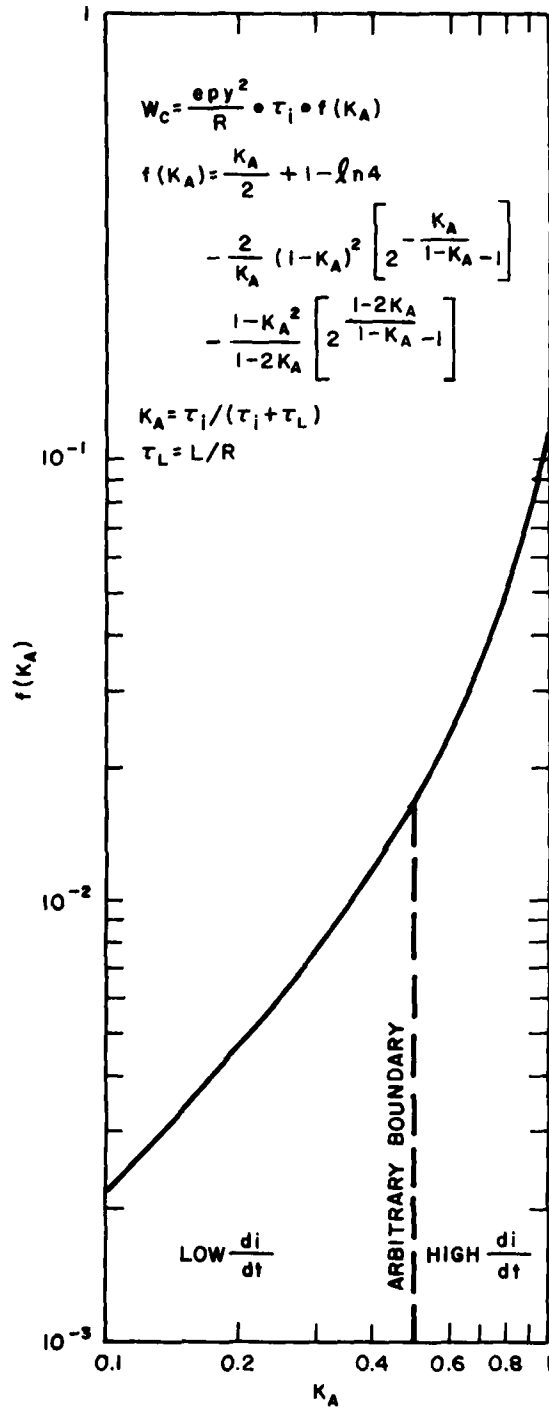


Figure 18. Plot of the function $f(K_A)$. The curve changes character at $K_A = 0.5$, so the anode energy increases rapidly with increasing K_A .

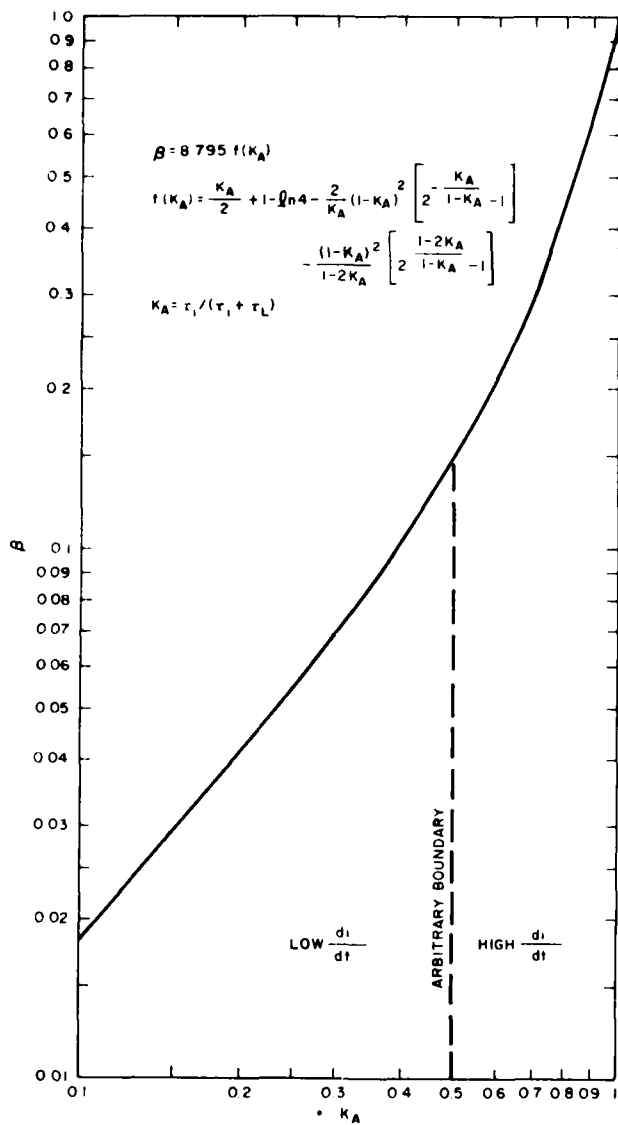


Figure 19. Ratio of the anode energy with inductance in the circuit to the anode energy with no inductance in the circuit. As the inductance approaches zero, K_A approaches unity.

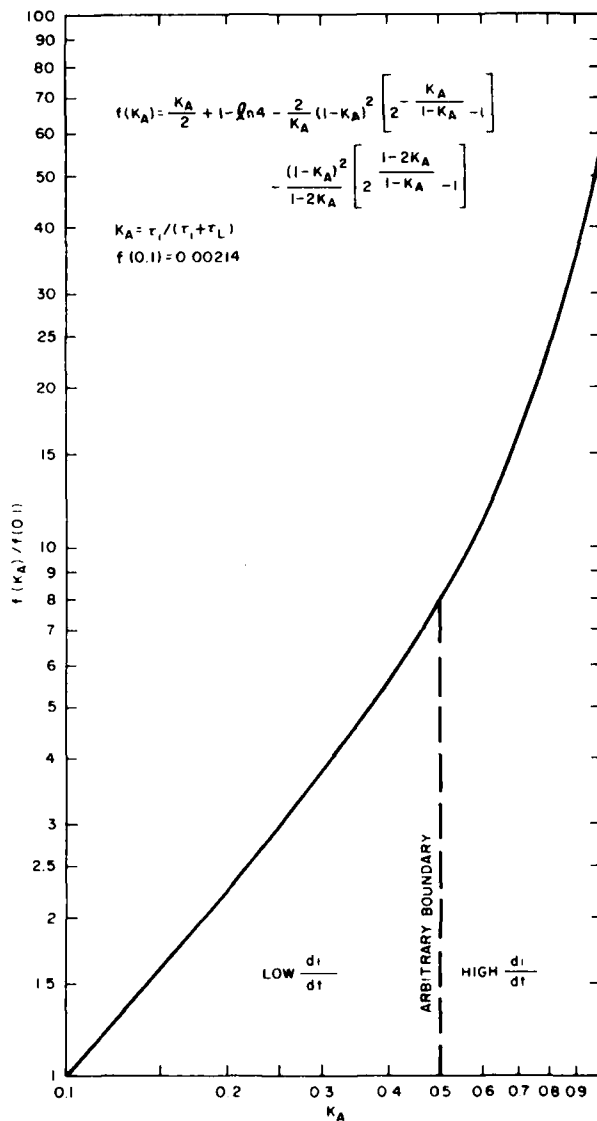


Figure 20. Plot of the ratio $f(K_A)/f(0.1)$. At $K_A = 1$ (zero inductance), the anode energy is over 50 times that of the low di/dt case.

Commutation Loss - Series RLC Circuit
With Negligible Damping

It frequently arises in high voltage pulse work that the energy storage mechanism is a charged capacitor instead of a charged transmission line. In this case the discharge circuit consists of capacitor C (charged to voltage, V_0) in series with inductance L (usually stray), with this combination in series with load resistor R.

Using the switch model, it can be shown that the circuit current during the commutation interval is

$$i(t) = \frac{V_0}{L} \cdot \frac{\gamma - \alpha}{\beta^2 + \gamma^2} e^{-\alpha t} \left(e^{\gamma t} - \cos \beta t - \frac{\gamma}{\beta} \sin \beta t \right) \quad (32)$$

where $\alpha = R/2L$, $\beta = [1/(LC) - \alpha^2]^{1/2}$ and $\gamma = \alpha + 1/\tau_i$.

It commonly occurs that the damping factor, α , is negligibly small.* In this case, Equation (32) simplifies to

$$i(t) = \frac{V_0}{L} \cdot \frac{\delta}{\psi^2 + \delta^2} \left(e^{\delta t} - \cos \psi t - \frac{\delta}{\psi} \sin \psi t \right) \quad (33)$$

where $\delta = 1/\tau_i$ and $\psi = 1/\sqrt{LC}$.

*A typical example is when the load is a gas discharge.

To determine the energy deposited at the anode over the commutation interval, recall Equations (11) and (13). Remembering that $T = \tau_i \ln 2$ and that $\delta = 1/\tau_i$, combine Equations (11), (13) and (33) to write

$$W = \int_0^{(\frac{1}{\delta}) \ln 2} \frac{V_0^2}{L} \cdot \frac{\delta}{\psi^2 + \delta^2} (2 - e^{\delta t}) (e^{\delta t} - \cos \psi t - \frac{\delta}{\psi} \sin \psi t) dt \quad (34)$$

Integrating Equation (34) and remembering that $\psi = 1/LC$, gives

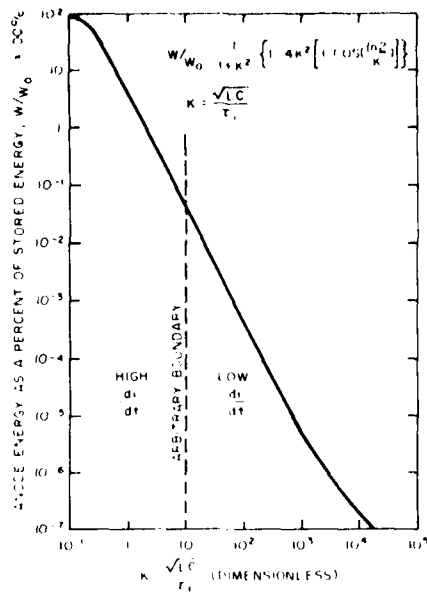
$$W = \frac{1}{2} CV_0^2 \cdot \frac{1}{1 + \frac{\delta^2}{\psi^2}} \left\{ 1 - 4 \frac{\delta^2}{\psi^2} \left[1 - \cos \left(\frac{\psi}{\delta} \ln 2 \right) \right] \right\} \quad (35)$$

where $\frac{1}{2} CV_0^2$ is recognized as energy W_0 , initially stored in the capacitor. If parameter $K = \delta/\psi$ is defined, Equation (35) can be rewritten as

$$\frac{W}{W_0} = \frac{1}{1 + K^2} \left\{ 1 - 4K^2 \left[1 - \cos \left(\frac{1}{K} \ln 2 \right) \right] \right\} \quad (36)$$

where $K = \delta/\psi = \sqrt{LC}/\tau_i$.

Parameter K is a dimensionless ratio relating the half-cycle time (divided by π) and the time constant of the anode fall. Equation (36) represents the fraction of the stored energy that is deposited at the anode of the switch during the commutation interval. For large K , only a modest fractional energy loss at the anode is expected because the relatively slow circuit will not allow buildup of high current during the comparatively short commutation interval. For small K , the opposite would apply. These characteristics are illustrated by Figure 21 which shows the percentage of the stored energy



CARISTI ET AL., ED-26, NO.10, OCT. 1979

Figure 21. Percentage of the stored energy that is lost to the commutation process as a function of parameter K. As K increases without bound (low di/dt case), W/W₀ approaches 1/K².

that is lost to the commutation process over several decades of K. At K = 10, an arbitrary boundary has again been defined between high di/dt and low di/dt operation. For small K (high di/dt), W/W₀ approaches unity. As K increases without bound, W/W₀ approaches 1/K².

Power dissipated at the anode can be significant at high di/dt and high prr. Consider, for example, a circuit where K = 3. From Equation (36), W/W₀ = 4.34 x 10⁻³. This means that the anode must dissipate 4.34 watts per joule of stored energy per kilohertz. For a 10 joule energy storage and a 10 kHz repetition rate, the anode must dissipate 434 watts — a nontrivial heat load.

Theoretical Basis for Anode Heating Factor — IIb

For years thyatron ratings have included the plate breakdown factor, Pb, defined by Equation (37).

$$P_b = epy \cdot ib \cdot prr \tag{37}$$

It had generally been recognized that Pb provided an inadequate measure of the anode heating situation, and from the results of experimental investigations, a new anode heating factor, Π_b , has been devised and is defined by Equation (38).

$$\Pi_b = epy \cdot \frac{di}{dt} \cdot prr \quad (38)$$

Using the relationships established earlier in this section for the switching of a charged transmission line, the validity of Π_b can be established, and useful approximations for the anode energy and the anode power dissipation can be devised.

The general expression for the anode energy is given by Equation (29) as

$$W_c = \frac{epy^2}{R} \cdot \tau_i \cdot f(K_A) \quad (29)$$

where $K_A = \tau_i / (\tau_i + \tau_L)$ and $f(K_A)$ is a cumbersome expression.

It is convenient to avoid K_A and instead consider W_c as a function of the ratio τ_i / τ_L . Figure 22 shows $f(K_A)$ as a function of τ_i / τ_L over four decades of τ_i / τ_L .

From Figure 22, for $10^{-2} \leq \tau_i / \tau_L \leq 1$ (low di/dt operation), $f(K_A)$ can be approximated by the relation

$$f(K_A) = 0.0185 \tau_i / \tau_L \quad (10^{-2} \leq \tau_i / \tau_L \leq 1) \quad (39)$$

This expression is accurate to within $\pm 10\%$ over the indicated range. Combining Equations (29) and (39) gives

$$W_c = 0.0185 \frac{epy^2}{R} \cdot \frac{\tau_i^2}{\tau_L} \quad (40)$$

Since $\tau_L = L/R$, Equation (40) may also be written

$$W_c = 0.0185 \frac{epy^2}{L} \cdot \tau_i^2 \quad (41)$$

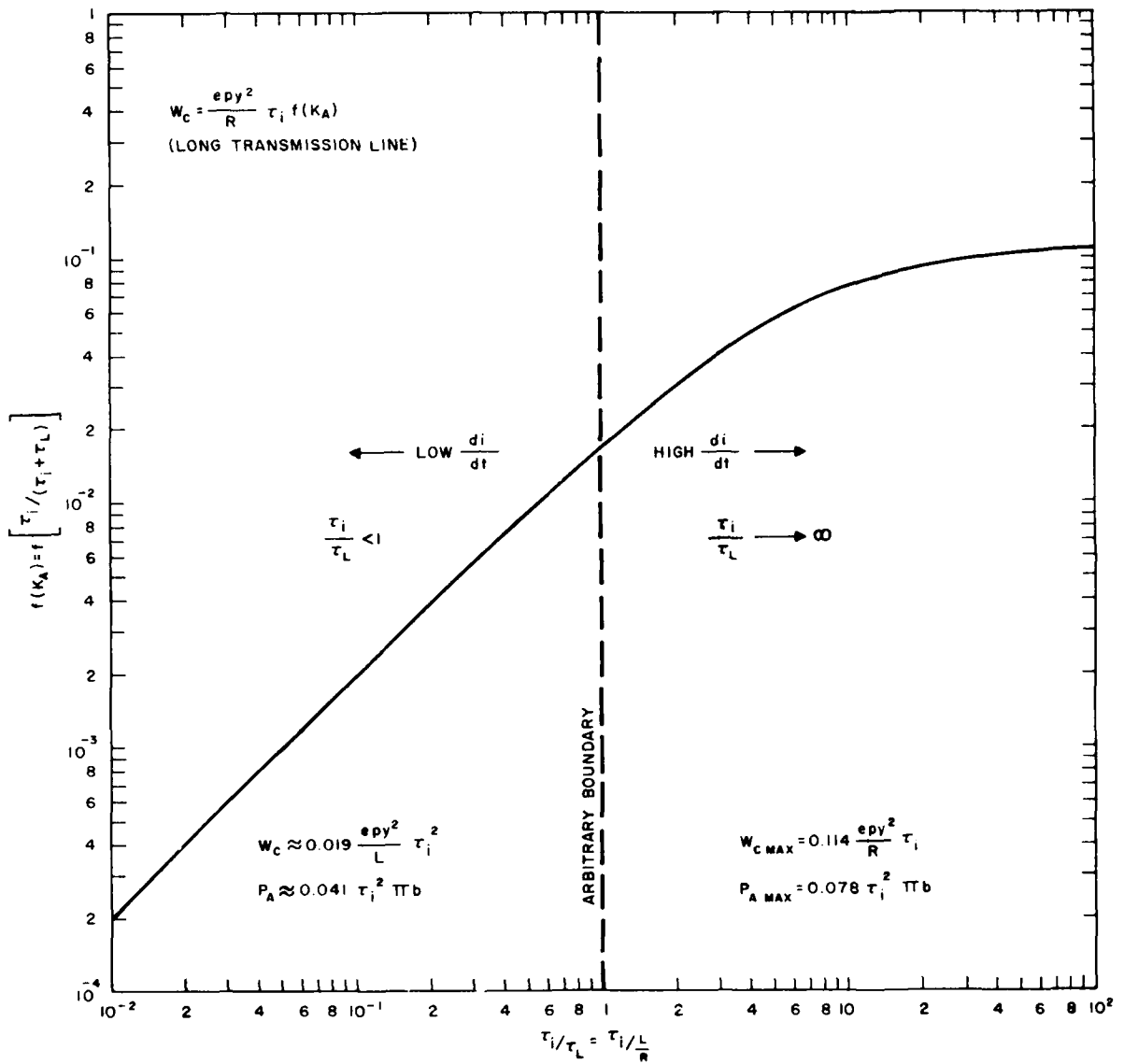


Figure 22. Function $f(K_A)$ vs ratio τ_i/τ_L . As τ_i/τ_L increases without bound, the anode energy approaches its maximum value.

Since $\frac{epy}{R} = ib$, Equation (40) can be written as

$$W_C = 0.0185 \text{ epy} \cdot ib \cdot \frac{\tau_i^2}{\tau_L} \quad (42)$$

Since we are considering the low di/dt case, the rise of ib is inductance-controlled, and the usual relation for the rise time (10% - 90%) of an inductance-controlled circuit can be used,

$$tr = 2.2 \tau_L \quad (43)$$

Combining Equations (42) and (43)

$$W_C = 0.0407 \text{ epy} \cdot ib \cdot \frac{\tau_i^2}{tr} \quad (44)$$

But $ib/tr \approx di/dt$. Thus Equation (44) can be rewritten as

$$W_C = 0.0407 \text{ epy}^2 \cdot \tau_i^2 \cdot \frac{di}{dt} \quad (45)$$

The anode power is thus

$$P_A = 0.0407 \tau_i^2 \cdot \text{epy} \cdot \frac{di}{dt} \cdot prr \quad (46)$$

Combining Equations (38) and (46)

$$P_A = 0.0407 \tau_i^2 \cdot \Pi b \quad (47)$$

Thus the anode dissipation is proportional to Πb , and this was the point to be demonstrated.

A similar approach can be used to validate the πb dependency of P_A in the high di/dt case. Under high di/dt conditions $\left(\frac{\tau_i}{\tau_L} > 1\right)$, the effects of τ_L diminish until finally the rise of i_b is determined solely by τ_i . The current during commutation is then as given by Equation (15)

$$\begin{aligned} i(t) &= \frac{V_0}{R} (\epsilon^{t/\tau_i} - 1) \\ &= i_b (\epsilon^{t/\tau_i} - 1) \quad \left(\frac{\tau_i}{\tau_L} \gg 1\right) \end{aligned} \quad (15)$$

where the notation has been changed for consistency.

It can easily be shown that the rise time corresponding to Equation (15) is

$$tr = 0.547 \tau_i \quad \left(\frac{\tau_i}{\tau_L} \gg 1\right) \quad (48)$$

Using Equation (48), di/dt can be approximated by the relation

$$\begin{aligned} \frac{di}{dt} &\approx \frac{\Delta[i(t)]}{\Delta t} = \frac{0.9 i_b - 0.1 i_b}{tr} \\ &= \frac{0.8 i_b}{0.547 \tau_i} \end{aligned}$$

or

$$\frac{di}{dt} = 1.46 \frac{i_b}{\tau_i} \quad \left(\frac{\tau_i}{\tau_L} \gg 1\right) \quad (49)$$

Recalling Equation (19)

$$P_A = 0.1137 \text{ epy} \cdot i_b \cdot \tau_i \cdot \text{pr} \quad (19)$$

Combining Equations (19) and (49)

$$P_A = 0.0779 \tau_i^2 \cdot e_{py} \cdot \frac{di}{dt} \cdot p_{rr}$$

or

$$P_A = 0.0779 \tau_i^2 \cdot \Pi_b \left(\frac{\tau_i}{\tau_L} \gg 1 \right) \quad (50)$$

Equation (50) shows the dependence of P_A on Π_b for the high di/dt case. Again, this was the point to be demonstrated.

Various relationships developed or utilized in this subsection are shown in Table 3. Pertinent parameters and applicable constraints have been defined in the text. In general, V_0 and e_{py} have been used interchangeably.

Accuracy and Significance of Dissipation Equations

The dissipation equations depend for their accuracy on the extent to which the switch model predicts the performance of an actual device. The model has successfully been used to predict pulse width, anode current rise time, peak current, and the time of the peak current under low di/dt and high di/dt conditions.

The keys to developing a successful model appear to be the observations that, over most of its fall, the anode potential decreases at an exponentially increasing rate, and that the time constant of the exponential depends only on the gas pressure in the tube.* Relying (as we did) on these basic observations, Goldberg and Rothstein⁽⁴⁾ assumed that the anode fall could be approximated by the relation

$$e(t) = e_{py} - A e^{t/\tau_i} \quad (51)$$

*It is actually the plasma density that determines the time constant, but the simpler concept of gas pressure is sufficient for the purposes of this discussion.

Table 3. Summary of equations related to anode dissipation.

<u>Description</u>	<u>Equation</u>	<u>Equation No.</u>
Resistive Anode Fall	$e(t) = V_0 (2 - e^{t/\tau_i})$	(11)
τ_i - P Relationship	$\tau_i = 23 P^{-0.42}$	(12)
Worst-Case Commutation Loss, Long Transmission Line	$W_C = 0.1137 \frac{V_0^2}{R} \tau_i$	(17)
	$= 0.1137 \text{ epy} \cdot i_b \cdot \tau_i$	(18)
Worst-Case Commutation Dissipation, Long Transmission Line	$P_A = 0.1137 \text{ epy} \cdot i_b \cdot \tau_i \cdot \text{pr}$	(19)
Switching Efficiency, Long Transmission Line	$\eta = 1 - 2 \left(0.1137 \frac{\tau_i}{t_p} + \frac{\text{etd}}{\text{epy}} \right)$	(24)
Exact Commutation Loss, Long Transmission Line	$W_C = \frac{\text{epy}^2}{R} \cdot \tau_i \cdot f(K_A)$	(29)
	$= \text{epy} \cdot i_b \cdot \tau_i \cdot f(K_A)$	*
Exact Commutation Dissipation, Long Transmission Line	$P_A = \text{epy} \cdot i_b \cdot \tau_i \cdot f(K_A) \text{ pr}$	*
Fractional Energy Loss at Anode, Underdamped RLC Circuit	$\frac{W}{W_0} = \frac{1}{1 + K^2} \left\{ 1 - 4K^2 \left[1 - \cos \left(\frac{1}{K} \ln 2 \right) \right] \right\}$	
	where $K = \sqrt{LC}/\tau_i$	(36)
Anode Heating Factor	$h_b = \text{epy} \cdot \frac{di}{dt} \cdot \text{pr}$	(38)
Approximate Commutation Energy, Long Line, Low di/dt	$W_C = 0.0185 \frac{\text{epy}^2}{L} \cdot \tau_i^2$	(41)
Approximate Anode Dissipation, Long Line, Low di/dt	$P_A = 0.0407 \cdot \tau_i^2 \cdot h_b$	(47)
Approximate Anode Dissipation, Long Line, High di/dt	$P_A = 0.0779 \cdot \tau_i^2 \cdot h_b$	(50)

*Not derived in the text, but apparent from first principles.

where A was an experimentally determined, constant voltage and τ_a was a pressure-dependent time constant equal to about 15% of our τ_i . Using Equation (51), an equation was derived for the anode energy (transmission line discharge) such that

$$W_C = 0.5 \text{ epy} \cdot ib \cdot \frac{\tau_a^2}{\tau_a + \tau_L} \quad (52)$$

Using Equation (52), and remembering that $\tau_a \approx 0.15\tau_i$, commutation energies are calculated within a factor of two of those calculated by the methods of this section, and this agreement applies over a reasonable range of operating conditions.

There is in fact little justification to seek dissipation relations that are accurate to better than a factor of two. Many factors that contribute to anode dissipation may do so in a noncalculable manner. Among these are inverse dissipation, heat radiated to the anode from other regions of the tube, and the establishment of density gradients in the tube such that the time constant of the anode fall is itself a function of the temperature in the grid-anode region. The value of the equations lies in their ability to provide a reasonable lower bound for the dissipation, and also in their illustration of pertinent functional dependencies. Since the analysis has shown that very high dissipation will occur at high di/dt and high prr, it is clear that considerable experimental work will eventually be required for tubes operated under these conditions.

6 TEST KITS FOR HIGH VOLTAGE, LOW INDUCTANCE TUBES*

a. 80 kV Pulse Charge System

The first test kit built for use on the program was an 80 kV pulse charge system built to determine the holdoff characteristics of single and multi-stage tubes at relatively low voltages under pulse charge conditions. The design of the kit was straightforward as is shown by the circuit of Figure 23. A charged capacitor was switched by a thyratron across the primary of a step-up pulse transformer. The secondary of the transformer charged a high voltage, lumped-element pulse forming network through a holdoff diode. The anode voltage run-up time depended on the resonant frequency of the transformer inductances and the circuit equivalent capacitances, and the dwell (or time on charge) depended on when the TUT was triggered after the run-up was completed.

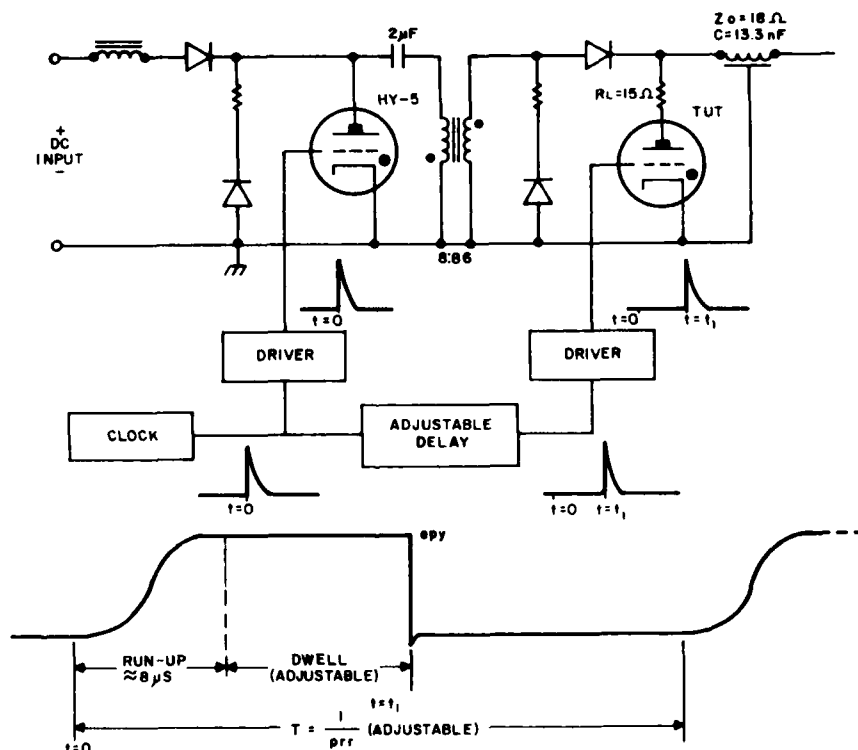


Figure 23. Schematic and waveforms — 80 kV test kit. Both the time on charge and the prr were adjustable.

*The test kits described in this section were funded by EG&G, Inc.

Since the kit was intended to be used only for investigations of voltage holdoff, the shape of the anode current pulse was of little consequence. A two-section, half-microsecond pulse forming network was used, and the impedance levels were chosen to provide a 2.4 kA current pulse at $e_{py} = 80$ kV. The anode voltage reversal was 9%.

The TUT was housed in an oil-filled, 15-inch diameter current return, and its anode waveform was monitored by a capacitance voltage divider (20 pF input capacitance). All other high voltages were monitored with frequency-compensated high voltage probes (100 megohms shunted by 3 pF). The cathode and reservoir heater voltages could be adjusted at will, and were measured directly at the pins of the TUT. Each tube had been calibrated during fill (P vs Eres), so the pressure in the TUT could be inferred from Eres in the kit.

The kit was operable in either of two modes. For normal operation, the circuit and waveforms of Figure 23 applied. The time, t_1 , was determined by the adjustable delay, and was set equal to the sum of the run-up time and the desired time on charge. The time, T, was the reciprocal of the prr as set by the clock. The capability of the power supply limited the maximum prr to a few tens of hertz, but this was adequate for the investigation.

To investigate tube operation at high prr, the clock of Figure 23 was replaced by a burst generator to obtain the anode voltage waveform shown in Figure 24. Both the number of pulses in the burst and the time between pulses could be adjusted, as could the burst rate itself. Operation in this mode was limited by the power supply to burst rates of only a few hertz, but it allowed examination of the TUT holdoff characteristics at high prr under a condition where the average heating was low.

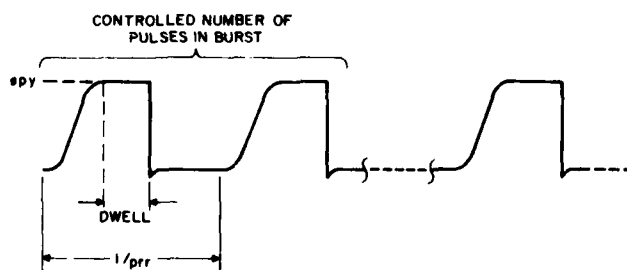


Figure 24. Anode waveform used to investigate prr characteristics. The number of pulses in the burst could be set at will.

b. 50 kV High di/dt System

Early in the Program, it was decided to perform high di/dt investigations at moderate voltages as opposed to attempting to build a 250 kV, high di/dt test kit, thus avoiding a situation where the test kit itself became a major project. A voltage of 50 kV was considered to be high enough to tax the tubes at the high gas pressures required for high di/dt, and yet low enough so that the test kit could be constructed with a minimum of difficulties.

Prior experience with Blumlein circuits and low inductance, liquid loads had shown that they introduced complexity and operational problems without enhancing the value of the experimental results. Therefore, a straightforward transmission line pulser with a resistive load was designed. The kit circuit and the appropriate waveforms are shown in Figure 25, and the mechanical aspects of the design are shown (simplified) in Figure 26.

The transmission line and load consisted of seven coaxial cables, each approximately 22 feet long, and seven coaxial resistors, with the seven line and load combinations in parallel as shown schematically in Figure 25. The nominal line impedance was 35 ohms (per cable) and each resistor was 31.3 ohms. The calculated equivalent line-plus-load impedance was thus $(35 + 31.3)/7 = 9.5$ ohms, and the calculated voltage reversal was 5.6%. The calculated total line capacitance was 9.24 nF, and the calculated pulse width was 92 nS. The observed pulse width was 90 nS and the observed pulse shape was indicative of near-perfect impedance matching, so the actual line impedance was less than its nominal value. The line was charged by the output of the pulse transformer used in the 80 kV pulse charge system. This arrangement provided a run-up time of about 6.5 microseconds.

The 90 nS pulse width was chosen because it was greater than the sum of the expected anode fall time and several L/R time constants where L was the estimated total circuit inductance (including that of the TUT) and $R = Z_0 + R_L = 9.5$ ohms. Under this condition, the whole of the current rise could be studied without any consideration being given to the finite length of the line. This condition was in fact achieved as discussed later in this report.

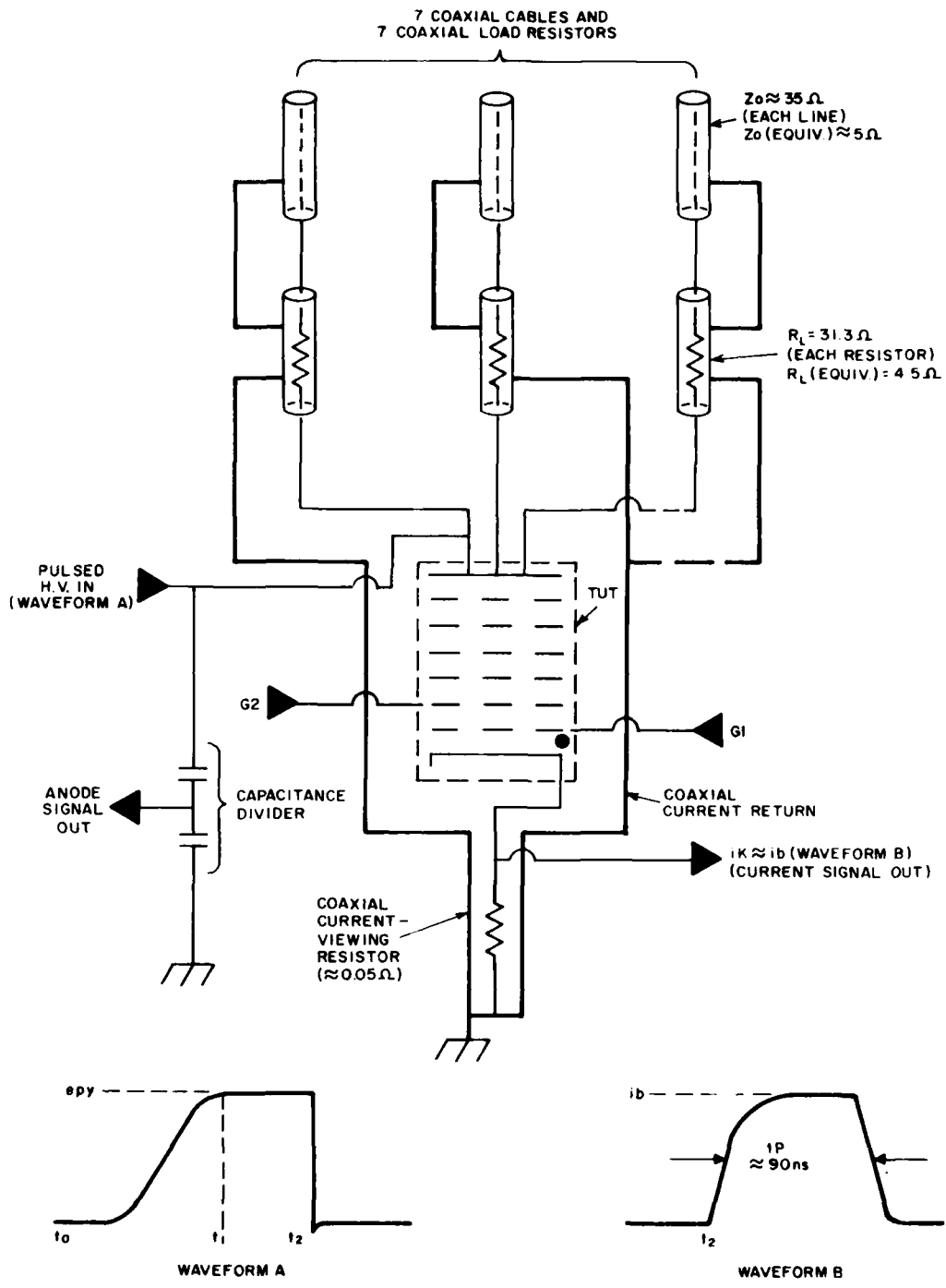


Figure 25. Schematic and waveforms - high di/dt test kit. The load was substantially matched to the line.

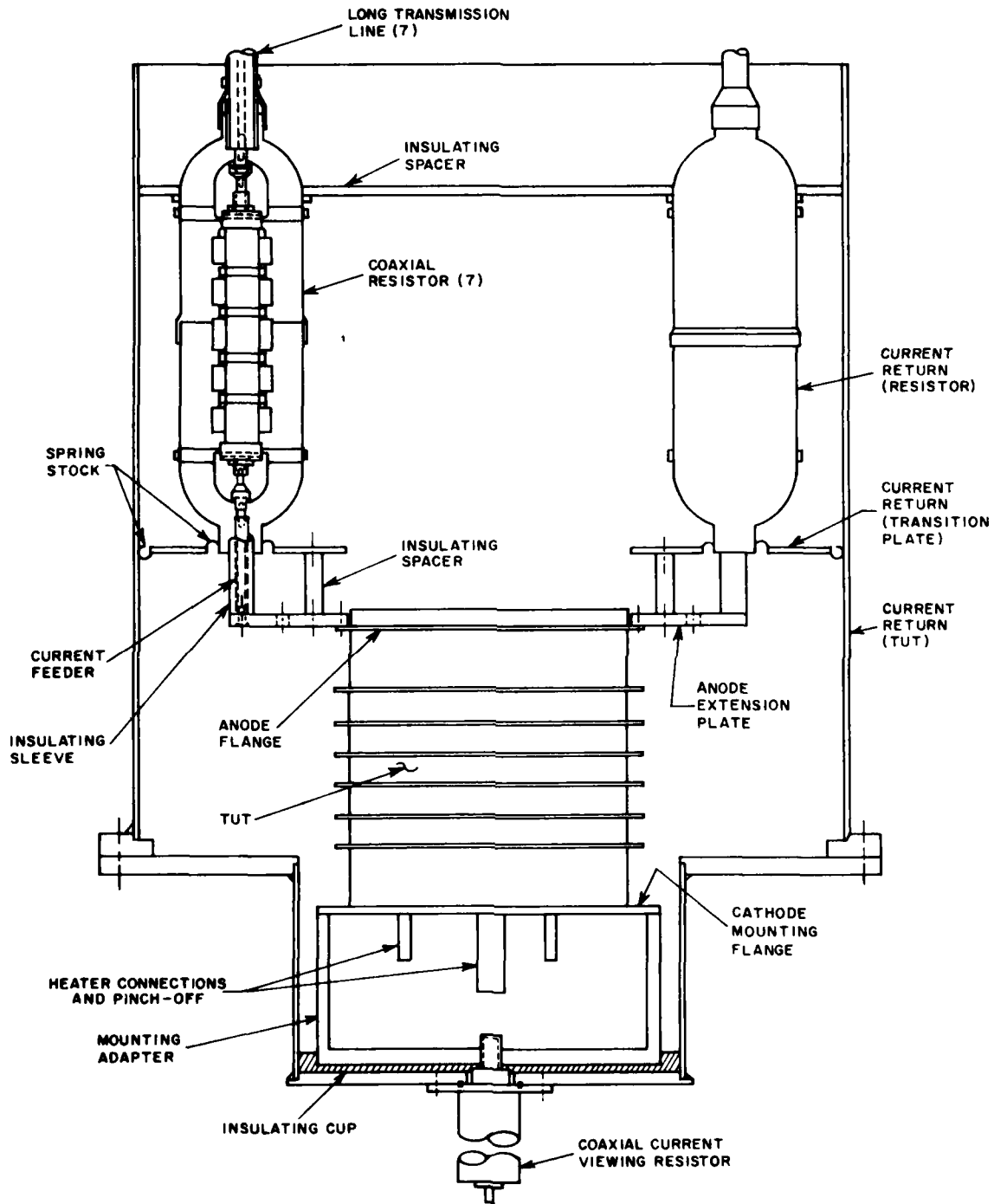


Figure 26. Construction of high di/dt kit. The entire tank was filled with insulating oil.

To duplicate the environment of a 250 kV tube, a 14-inch diameter current return with oil insulation was used. This established the appropriate voltage distribution across the tube, and also allowed room within the current return to include oil-insulated coaxial resistors. The resistors added inductance to the discharge loop, but allowed control of the inverse voltage on the TUT and also limited its anode dissipation. In the low voltage region of the tube, a smaller diameter return was used as shown in Figure 26. The mounting adapter (Figure 26) was necessary to provide clearance for the heater pins and pinch-off, but because of its large diameter (compared with that of the return in this region), it added little inductance to the circuit. The TUT current was measured with a coaxial current viewing resistor (0.05 ohm, 2-5 nH) as shown.

The anode flange was extended to a diameter convenient for mating with the load resistors, and a ground return transition plate was used to transfer the return current from the tank to the coaxial return of the resistors. The transition plate was fitted with a spring finger stock arrangement to accommodate tubes of different heights.

The load resistors required careful design. Fifty 2-watt carbon resistors (10 in parallel, 5 in series) arranged around a teflon core for each of the seven loads were used. Each core assembly was then fitted with its own coaxial return such that the impedance of the structure thus formed was 35 ohms to match the individual cables. Holes in the current return allowed the insulating/cooling oil to enter the resistor structure.

Each resistor was designed to withstand the stress when the line was charged (50 kV to ground), and its voltage drop during the current pulse (~25 kV). The kit performed well throughout the investigation.

It was estimated that each resistor had an inductance between 25 and 50 nH. Using the geometric mean (35 nH), the equivalent inductance of the load was estimated to be 5 nH, and that of the kit (less the TUT) to be 10 nH. The results of current rise rate measurements proved this estimate correct.

c. 250 kV Pulse Charge System

The essence of the design of the 250 kV system is shown in Figure 27. The philosophy of the design was substantially the same as that of the 80 kV kit previously described. The pulse forming network was designed to generate a half-microsecond current pulse of 1.7 kA at 250 kV with a 4% voltage reversal. The run-up time is 5 microseconds, and the time on charge is adjustable as with the 80 kV system.

The lower voltage components of the system are mounted in an air-insulated rack adjacent to an oil-insulated high voltage tank. The high voltage components (including the TUT and its coaxial current return) are mounted in the tank.

At the time of this writing, this kit has not been operated beyond $V_{\text{ep}} = 120$ kV. At that voltage, a breakdown occurred in the step-up transformer. A new winding of an improved design was procured for the transformer and the kit was repaired, but not in time to provide any data for this report beyond that shown in Figure 40.

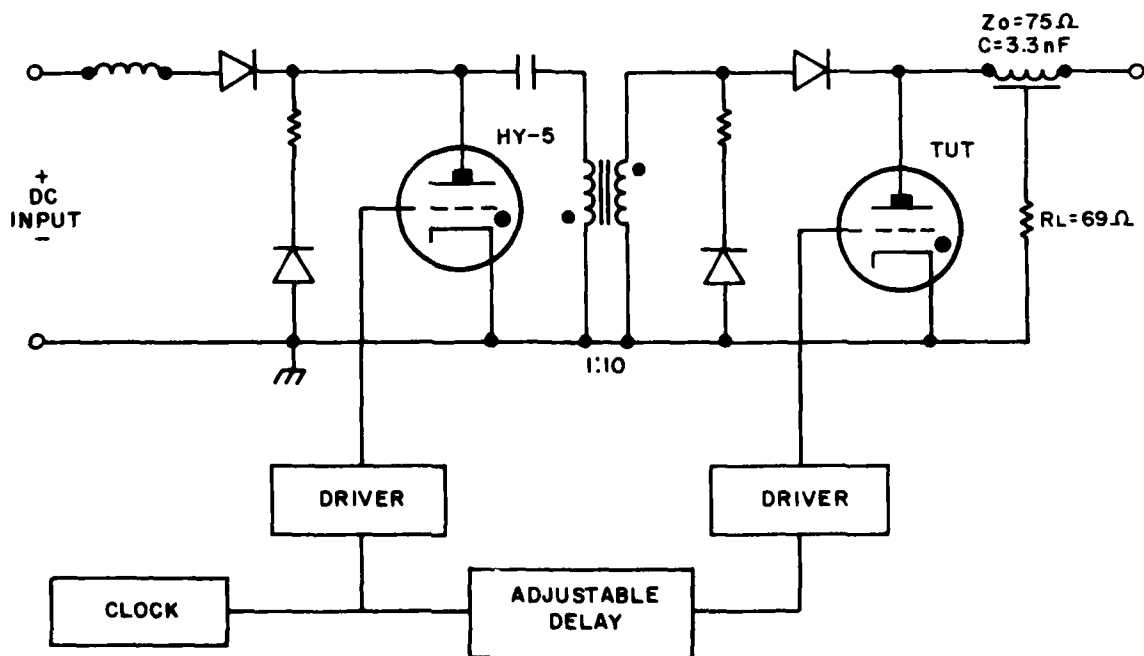


Figure 27. Schematic of 250 kV test kit. Run-up time is about 5 microseconds.

7 EXPERIMENTAL TUBES AND TEST RESULTS

a. Objects of the Experimental Work

The experimental work of Phase II was directed toward determining the characteristics of multi-stage hydrogen thyratrons having a plurality of short, box-type gradient grids. At the beginning of Phase II, it remained to be shown that such tubes could in fact be made to trigger and commute "through" in substantially the same manner as conventionally designed tubes. It also remained to be shown that short ceramic insulators could withstand the voltage stress attendant to tube operation under the desired conditions. These two considerations had to be addressed experimentally before a very high voltage, low inductance tube could be considered as being a feasible proposition.

It further remained to characterize multiple box-grid tubes with respect to stage voltage addition, voltage holdoff as a function of pressure and time on charge, anode current rise time, operation at high prr, and general triggering properties. The experimental tubes designed, built, and tested during Phase II served as the vehicles for determining these characteristics.

b. Experimental Tubes

A total of seven multi-stage tubes were designed under the auspices of the Program. Data were obtained from five of the seven; two have yet to be tested. Several single-stage low inductance tubes were also characterized. The multi-stage tubes were as follows:

(1) HY-5505

This five-stage tube was designed during Phase I and operated during Phase II. Its primary purpose was to demonstrate that a multi-stage device could trigger and commute through. The tube performed this function and was in fact operated at 40 kV, 1.6 Adc in a standard production test kit. Due to a mechanical design defect (insufficient stress relief in the grid structures), the envelope cracked and the tube went to air shortly after its first operation.

(2) HY-5506

Like the HY-5505, the 5506 was a five-stage device having unbaffled gradient grids. The tube was filled with deuterium and was operable over a pressure range of 300 to 600 microns. Each of the five gaps was 0.125 inch. A photograph of this tube is shown in Figure 28.

(3) HY-5507

The HY-5507 was a five-stage tube having unbaffled gradient grids. The tube was equipped with a "hollow" anode (deep slots cut into the anode, with these slots being in line with the apertures of the uppermost gradient grid) to reduce damage from electron bombardment. The 5507 also had varying gap spacing (0.122-inch at the control grid to 0.091-inch at the anode). The nonuniform spacing was chosen to alter the ratio C1/C2 along the length of the tube so as to force a reasonably uniform distribution of the charging voltage across the various stages of the tube.

During DC aging of this tube, it went into a high impedance glow mode such that there was a significant tube drop in conjunction with a significant anode current. The resultant power caused an internal hot spot, the envelope cracked, and the tube went to air.

Prior to tube failure it was established that the voltage division was in fact substantially uniform, although no detailed studies were performed, nor did the tube operate at high di/dt. Therefore, the efficacy of the hollow anode concept remains to be verified.*

(4) HY-5508

The HY-5508 was a three-stage device having relatively tight gradient grid baffling. Like the 5506, the 5508 had 0.125-inch gaps and a deuterium fill. The tube was operable over the pressure range of 300 to 600 microns.

(5) HY-5509

The HY-5509 was identical to the HY-5508 except that its gradient grids were less tightly baffled.

*A single-stage tube is being built to investigate the utility of this concept.

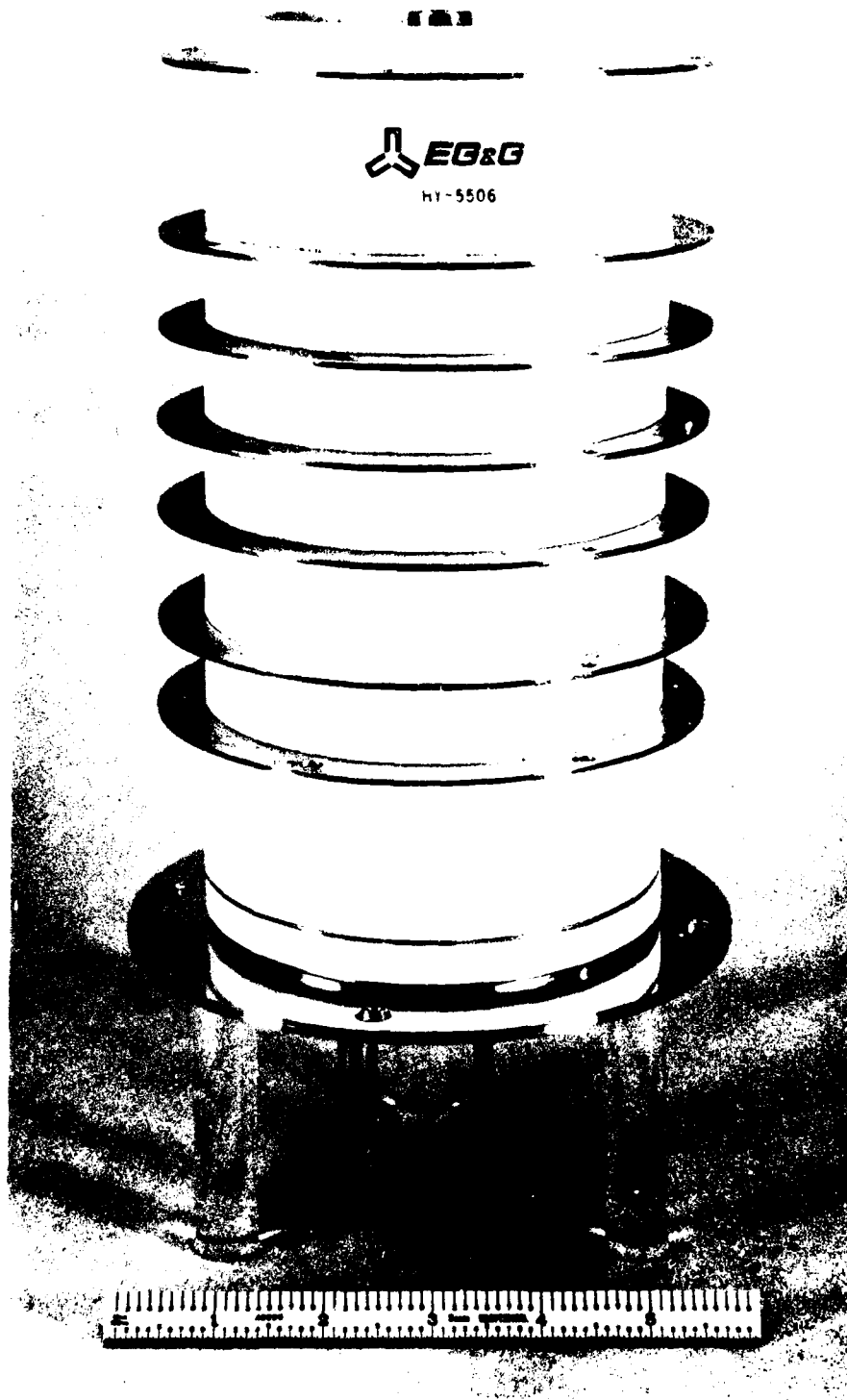


Figure 28. Five-stage HY-5506. Seated height of the tube is less than 10 inches.

(6) HY-5515

The HY-5515 is a three-stage device having 0.125-inch gaps and an aperture width 25% larger than the other 55 series tubes. The 5515 was left unassembled in the event that testing the other tubes showed that some particular modification would be required. It is presently planned to incorporate special gradient and control grid baffles into this tube and to test the device before the end of Phase III.

(7) HY-5525

The HY-5525 is a five-stage tube designed to operate at 150 kV and to have an inductance of about 40 nH (with 12-inch-diameter current return). The HY-5525 is the intermediate experimental tube to be delivered to ERADCOM under the contractual requirements for Phase II. The design of this tube is discussed at length elsewhere in this report.

From the above discussion, it is clear that three tubes were available for extended experimental studies during Phase II — the HY-5506, 5508, and 5509. These tubes proved to be ideal vehicles for the generation of desired data. The experimental results are discussed below.

c. Test Results and Interpretation

(1) Ceramic Stress Tests

In conventional ceramic-metal hydrogen thyratron designs, the interelectrode spacing is established as desired and the insulator length is independently chosen by varying the length of a suitable electrode "cup." The usual criterion for insulator length is the absence of breakdown between the cup flanges in the medium (usually air) external to the tube. Because of the short stage lengths required for low inductance tubes, operation in air is, in general, precluded at any appreciable epy, and the proximity of the grounded coaxial current return would require operation in oil or insulating gas even if flange-to-flange breakdown were not a consideration. For very low inductance, high voltage tubes, the breakdown properties of the ceramic insulators strongly influence the lower limit for the stage length, and thus the minimum inductance for a practical high-voltage tube.

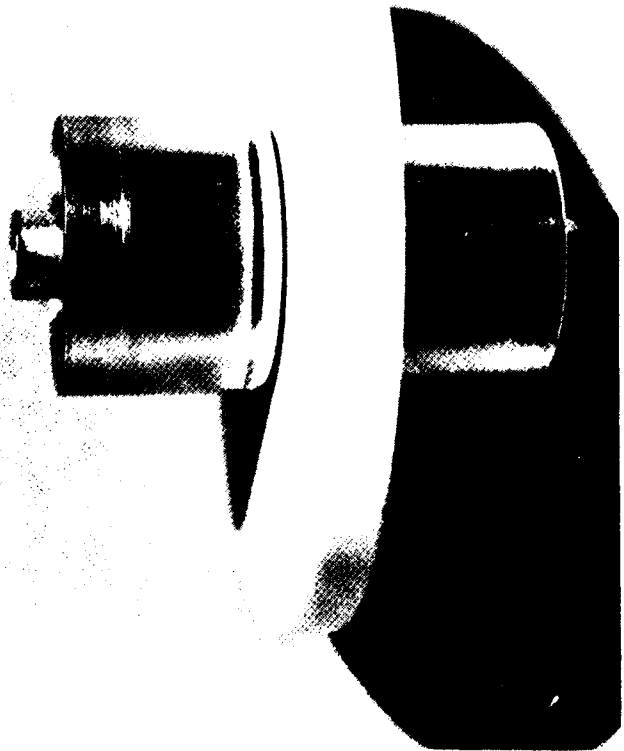
Breakdown data for high alumina ceramics were not known to exist for the temporal and spatial stress conditions applicable to high voltage, low inductance thyatron operation. Therefore breakdown data were compiled, but were limited to ceramics that were processed and metallized in a manner substantially identical to that normally used for the insulators incorporated into a tube. The samples were subjected to stress conditions having the temporal characteristics expected in actual operation.

A typical sample is shown in Figure 29. A quarter-inch thickness was chosen. This was thin enough so that breakdown was likely to occur (thus providing definitive data), but thick enough so that the results could confidently be scaled to typical interstage insulator lengths (of the order of 1 inch). Each sample was metallized over an area corresponding to the central one-third of its diameter. Electrodes were then brazed to the metallized area using substantially the same apparatus and techniques that would be used to assemble an actual tube.

To stress the samples, the four-stage Marx generator shown in Figure 30 was built and characterized. The characteristics of the device were as shown in Table 4. The decay time of the Marx was controlled by varying a pre-load, and the rise time at the sample by varying a series resistor, thus taking advantage of the sample capacitance and that of the capacitance voltage divider that was used to monitor the voltage across the sample. For most of the testing, the samples were mounted within an oil-filled lucite vessel having internal dimensions materially larger than those of the sample under test.

The approach to the breakdown testing was strongly influenced by the characteristics of the Marx and by the stray inductance and capacitance of the experimental apparatus as a whole. The equivalent series inductance of the loop formed by the Marx, the sample, and the connections between the two were about 1.5 μH , while the stray capacitance to ground (including that of the sample) was a few tens of pF.

Unless damping resistors were used in series with the sample under test, the series inductance and the stray capacitance would resonate such that the voltage across the sample would reach nearly twice the output voltage of the



CARISTI ET AL., ED-26, NO. 10, OCT. 1979

Figure 29. Typical ceramic sample with electrodes. The samples were 1/4-inch thick.

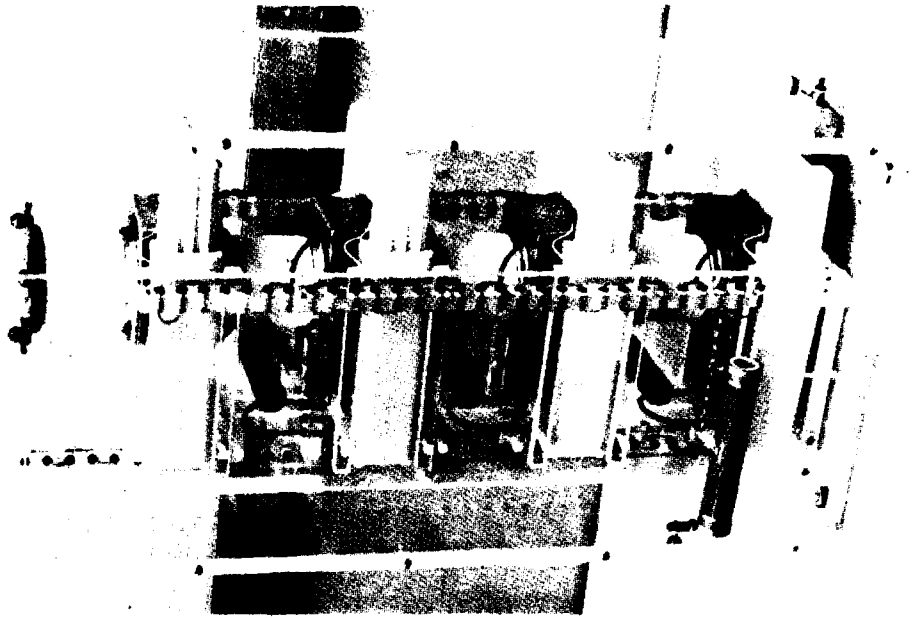


Figure 30. Marx generator used for sample testing. The characteristics of the Marx influenced the approach to the breakdown tests.

Table 4. Characteristics of Marx generator used for ceramic sample evaluation.

Number of stages	4
Capacitance per stage	0.04 μ F
Equivalent capacitance when erect	0.01 μ F
Charging time	16 sec
Maximum input voltage	65 kV
Maximum output voltage	260 kV
Maximum working output voltage (Note 1)	240 kV
Energy stored at 60 kV input	288 joules
Total time to erect (Note 2)	800 nS
Output voltage rise time	100 nS
Short circuit current (Note 3)	14 kA
Equivalent shunt resistance	10 K ohms
Equivalent series inductance (Note 4)	1.5 μ H

Notes:

- 1) For input voltages greater than 60 kV, the spark gaps occasionally flash over externally. This limits the output voltage to 240 kV for trouble-free operation.
- 2) Total of gap delays and output voltage rise time at 240 kV (open circuit).
- 3) Measured when discharging the device into a 9-inch arc with 55 kV input.
- 4) Calculated from measurements of the ringing frequency under the conditions of Note 3.

Marx. For some tests, this mode of operation was desirable since very high voltages could be applied to the sample for tens of nanoseconds – conditions that would apply for the upper-stage insulators of a tube that was undergoing commutation.

In other cases, it was necessary to include a series resistor to preclude the resonant charging effect. The resistance served to limit the voltage at the sample and also reduced the voltage rise time, but such operation made it possible to make an accurate determination of the stress-time conditions. By properly adjusting the circuit constants, it was thus possible to approximate the ceramic stress situation that would apply during the pulsed charging (on a microsecond time scale) of an actual tube.

The breakdown properties of three types of ceramic were investigated: Alberox 94% alumina, Wesgo 97% alumina, and Diamonite conductive alumina. The Alberox and Wesgo ceramics were tested because these two firms supply many of the ceramic insulators used in standard EG&G tubes. The Diamonite ceramics were tested to determine if their relatively high conductivity might result in better holdoff due to charge equilibration throughout their volumes – at least on the microsecond time scales corresponding to pulsed charging. Of ten Wesgo samples, five were metallized by Alberox using a Mo-Mn process, and five were metallized by EG&G using a titanium hydride process. This was done because both processes are used for metallizing the insulators used in EG&G tubes, and because the properties of ceramics are in general a function of their processing history. The Alberox ceramics were Mo-Mn metallized by Alberox, and the Diamonite pieces were hydrided by EG&G. Electrodes were vacuum brazed to the metallized surfaces of each sample by EG&G, with the time-temperature profile being identical for all pieces.

For most of the breakdown testing, the samples were immersed in clean, motionless transformer oil at room temperature and atmospheric pressure. A few samples were also tested in distilled water as discussed further below.

The breakdown voltages of 32 samples when immersed in oil are shown in Table 5, where the data have been arranged according to ceramic type and metallization process.*

*To generate the data of Table 5, resistors were located in series with the Marx to preclude resonant charging effects. The rise time of the voltage at the sample was typically 2 μ s.

Table 5. Breakdown voltages of ceramic samples when immersed in transformer oil.

Alberox 94% Alumina (Mo-Mn Process)	
Sample No.	Breakdown Voltage (kV)
5	86
6	90
7	85
8	94
9	86
11	92
20	84
25	88
28	94
29	89
30	84
<u>31</u>	<u>82</u>
12 Samples	88 ± 6 kV

Diamonite Conductive Alumina (Hydride Process)	
Sample No.	Breakdown Voltage (kV)
2	90
10	88
12	96
13	94
14	88
15	94
16	92
17	96
19	92
<u>21</u>	<u>96</u>
10 Samples	92 ± 4 kV

Wesgo 97% Alumina (AL-300) (Mo-Mn Process)	
Sample No.	Breakdown Voltage (kV)
37	102
38	96
39	90
40	104
<u>41</u>	<u>116</u>
5 Samples	103 ± 13 kV

Wesgo 97% Alumina (AL-300) (Hydride Process)	
Sample No.	Breakdown Voltage (kV)
26	100
27	100
34	90
35	97
<u>36</u>	<u>96</u>
5 Samples	95 ± 5 kV

The most striking characteristic of the data of Table 5 was that the breakdown voltages of all samples were substantially the same. For the 32 samples shown, the breakdown voltage was 99 ± 17 kV, with a typical breakdown time of 3-5 μ S after the start of the voltage rise. The uniformity of the data suggested a point-to-plane type of breakdown as opposed to parallel-plate breakdown where a deviation of $\pm 50\%$ would be representative of good data. Furthermore, all of the samples punctured just outboard of the electrodes — in a region where a high local field might be expected to exist in the oil because of its relatively low dielectric constant ($\epsilon_r = 2.2$) compared to that of the ceramics ($\epsilon_r = 9$). It is believed that this field ionized the gases dissolved in the oil, the ionized region then acted as a needle, and the enhanced field intensity that resulted caused ceramic breakdown to ensue. This analysis was also consistent with the fact that samples that had previously been stressed in oil to 100 kV DC without incident would break down at voltages less than 100 kV under pulsed conditions.

In the DC case, charges in the oil were able to migrate to the ionized region of the oil where they could neutralize the ionization by space charge shielding. Under pulsed conditions, there was insufficient time for charge migration to occur. The overall conclusion was that uncontrollably high fields were being generated in the ceramics, and that this condition would mask any differences in breakdown strength that might exist due to different ceramic types or metallizing processes.*

To verify that the samples were breaking down because of enhanced fields created by ionization in the oil, three samples were tested when they were immersed in distilled water ($\epsilon_r = 80$) instead of oil. The reasoning was that the high dielectric constant of the water would force a uniform distribution of the applied field throughout the ceramic, and thus provide a better indicator of the ceramic inherent breakdown strength. Three arbitrarily

*The data did suggest, however, that the Wesgo ceramics had a somewhat higher breakdown strength than the Alberox ceramics. The Wesgo ceramics contained more crystalline glass or "glass ceramic" than did the Alberox samples; they were in general a denser material. Subsequent partial discharge tests were performed on both types, and while the tests showed that both were good insulators having high corona inception and extinction voltages, the Wesgo samples were in fact quieter at any given stress level.

chosen samples were also tested; the results are shown in Table 6 and Figure 31(a). Note that breakdown did not occur for any of the samples at voltages of 165 to 170 kV — the highest voltages that could be generated in a controlled fashion. The same three samples were then tested in oil where they promptly broke down as shown in Table 7 and Figure 31(b). These data verified our hypothesis, and suggest that under ideal conditions, the breakdown strength of the ceramic exceeds 600 kV/inch.

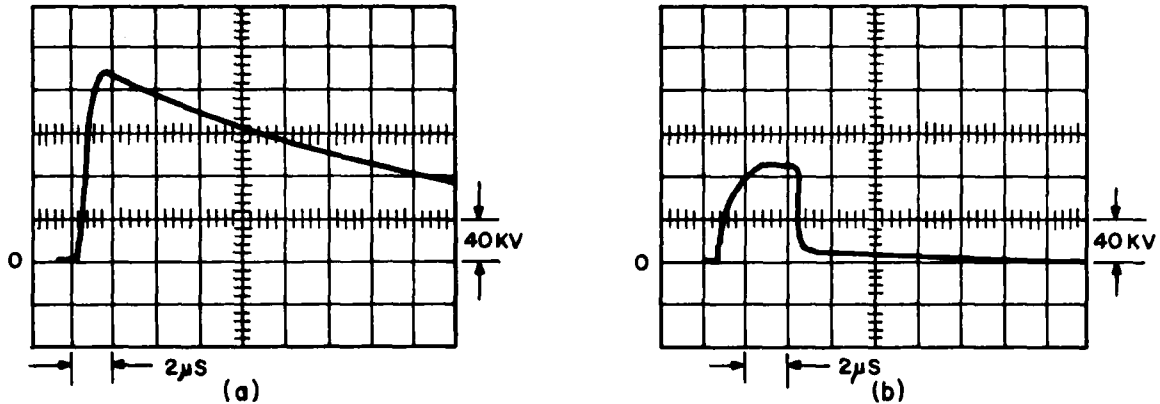


Figure 31. Waveforms showing sample holdoff (a) and sample breakdown (b). Breakdown occurred because of high local fields in the oil.

Table 6. Holdoff properties of ceramic samples when immersed in distilled water. The samples were Alberox alumina with Mo-Mn metallizing.

Sample No.	Holdoff Voltage (kV)
29	170
30	168
31	165

Table 7. Breakdown voltages for the samples of Table 6 when the samples were immersed in transformer oil.

Sample No.	Breakdown Voltage (kV)
29	89
30	84
31	82

To gain additional breakdown information, two solid ceramic cylinders, 0.97-inch long, were each fitted with electrodes that were sized and shaped to promote stress equalization along their lengths. Each assembly was immersed in oil and pulsed with essentially the full output of the Marx. Because of the resonant charging effects previously described, the peak of the applied voltage could not be accurately measured but it was estimated to be several hundred kilovolts for tens of nanoseconds. Neither sample failed after repeated exposure to such stresses, thus supporting the view that fields of at least hundreds of kilovolts per inch can be sustained by high alumina ceramics that are exposed on short time scales.

Although the data are encouraging, an actual tube insulator must always operate in an environment where for at least one of its surfaces (that facing the inside of the tube), the relative permittivity of the adjacent medium is low pressure gas with $\epsilon_r = 1$. This points to the need to shape both the insulator and the electrodes such that field enhancement is kept to a minimum. From the existing data, the absolute stress at which ceramic breakdown took place cannot be inferred. However, no sample failed below 82 kV and all samples were 0.250-inch thick. Thus all samples successfully sustained fields of at least 328 kV/inch. Fields such as this are well above those required for a tube that can meet the objectives of this Program, provided that localized field enhancement can be avoided by proper shaping of both the insulators and the electrodes.

(2) Holdoff vs Time on Charge

Gas discharge devices do not effectively operate as DC switches. Under true DC conditions (many minutes on charge), random breakdowns will usually limit their absolute holdoff to some value materially lower than that achievable under pulsed conditions.

Most thyatron ratings for peak forward voltage are based on the holdoff capability of the device when it is resonantly charged on millisecond time scales. In the regimes of pressure and gap spacing where thyatrons are usually operated (200-500 microns, 2-4 millimeters), this leads to typical ratings of 25-40 kV for a single gap device.

Four time-related thyratron holdoff modes can be established (somewhat arbitrarily) as shown in Table 8. Only the dynamic holdoff mode is relevant to this Program. This mode provides the highest achievable epy in conjunction with kick-out-free operation, while simultaneously minimizing the high voltage exposure time of the system as a whole.

Table 8. Time related thyratron breakdown regimes.

Holdoff Mode	Time on Charge	General Breakdown Characteristics
Long-Term DC	Minutes or longer	Random kick-outs; holdoff capability depends on definition (allowable kick-outs over chosen time interval)
Short-Term DC	Few seconds	Reasonably repeatable breakdown voltage; occasional kick-outs
Normal Operation	Tens of microseconds to several milliseconds	Well-defined breakdown voltage; essentially zero kick-outs
Dynamic Holdoff	Tens of microseconds or less	Significant holdoff enhancement when compared with "normal" operation; zero kick-outs

Table 9 shows the normalized dynamic breakdown voltage (at high pressures) as a function of the time on charge (dwell) for a typical single-stage tube — the EG&G Type HY-5.* To generate Table 9, the dynamic breakdown voltage at various pressures was determined for dwell times of 2 mS down to 2 μ S, and the DBV at each dwell and pressure was then normalized to the DBV for a 2 mS dwell at the corresponding pressure. The data of Table 9 represent the enhancement in epy that is typically achieved when the dwell is reduced from that corresponding to "normal" operation (Table 8) to that corresponding

*Unless it is specifically stated to the contrary, all DBV data discussed in this report were obtained at low pulse repetition rates — a few tens of hertz. Such operation is useful to determine the absolute characteristics of the tubes under test, i.e., their characteristics under conditions where residual ionization can play no role. It is to be understood that a subsequent and major effort will be required to extend the capabilities of multi-stage tubes to high prr.

Table 9. Dynamic breakdown voltage as a function of time on charge, DBV (T), normalized to dynamic breakdown voltage for 2 mS on charge.*

Time on Charge (T)	Gas Pressure, P (microns)	DBV (T)/DBV (2 mS)
1 mS	594	1
	610	1
	622	1
	640	1
	660	1
100 μ S	594	1
	610	1
	622	1
	640	1
	660	1
10 μ S	594	1.05
	610	1.06
	622	1.05
	640	1.04
	660	1.06
2 μ S	594	1.15
	610	1.18
	622	1.18
	640	1.19
	660	1.25

*Data for EG&G Type HY-5; 0.140-inch gap; run-up time, 8 μ S.

to true dynamic conditions. As the data show, the DBV for dwells of 2 mS, 1 mS, and 100 μ S are identical. Holdoff enhancement begins with a dwell time of 10 μ S and becomes significant at 2 μ S.

Data of a similar nature (but only for short dwells and for a wider pressure range) are shown graphically in Figure 32 for another single-stage tube — the EG&G HY-5313. Note from Figure 32 that reducing the dwell becomes increasingly beneficial as the pressure is increased — a trend also shown by the 2 μ S data of Table 9.

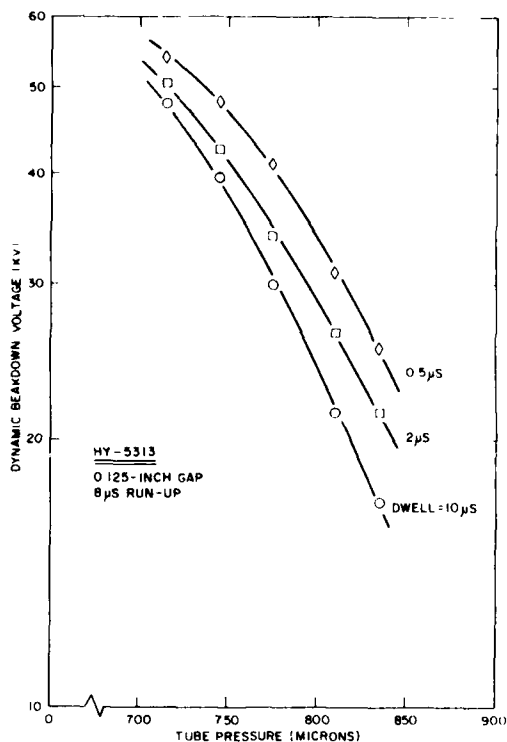


Figure 32. Dynamic breakdown voltage (DBV) as a function of pressure, with time on charge (dwell) as a parameter. Shorter dwells are most effective at high pressures.

Figure 33 shows the short-term (static) holdoff characteristic (5 seconds on charge) and the dynamic holdoff characteristic (2 μ S on charge) for both the lower stage and all five stages of the HY-5506. Note from the one-stage data that pulse charging serves to avoid the apparent vacuum-breakdown-limited holdoff condition that occurs at pressures below 300 microns. Note also that pulsed charging is again most beneficial at the higher pressures.

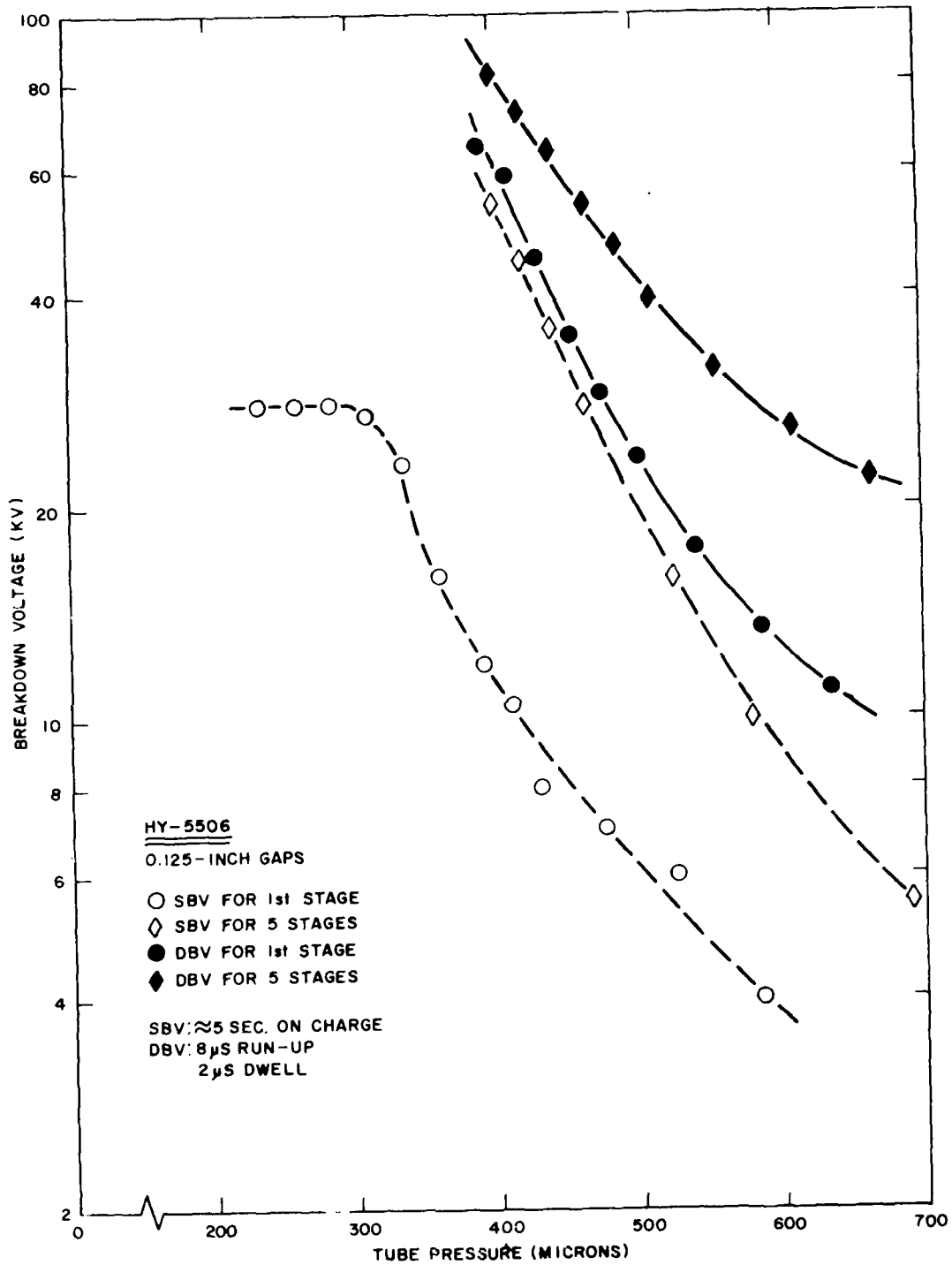


Figure 33. Dynamic and static breakdown — HY-5506. Pulse charging is most effective at high pressures.

Reducing the run-up time (as well as the dwell) might lead to additional improvements in holdoff. However, reducing the run-up time places increasingly severe requirements on the charging circuit, and the existing data suggest that any resultant improvements in holdoff would be minimal.

Trends discussed in this subsection were widely observed for various tubes tested during Phase II. The overall conclusion is that pulsed charging with a few microseconds on charge does allow tube operation at increased peak forward anode voltages. The enhancement of epy is significant. It is equally important that pulsed charging precludes kick-outs and simultaneously reduces the high voltage exposure time for the system as a whole.

(3) Holdoff vs Gas Pressure

The holdoff-pressure characteristic is central to the design of all types of gas discharge switches. Hydrogen thyratrons operate to the left of the Paschen minimum so that reducing the product of pressure and electrode spacing increases the achievable holdoff until vacuum breakdown occurs. (In the vacuum breakdown regime, the breakdown voltage becomes independent of the pressure-spacing product.) The Paschen curve for deuterium is somewhat higher than that of hydrogen, so most high voltage "hydrogen" thyratrons are deuterium filled.

Operation to the left of the Paschen minimum has other ramifications. As the pressure is reduced to increase holdoff, the deionization time of the gas decreases. This promotes tube operation at high repetition rates, but it inhibits the generation of the triggering plasma that initiates the commutation process. Similarly, it materially lengthens the time constant of the anode fall; the tube takes longer to "turn on." In low inductance circuits, a long turn-on allows a condition of simultaneous anode voltage and anode current, promoting high anode dissipation and, frequently, a short tube life.

At high pressure the reverse conditions apply. The recovery time is long, thus limiting the prr. The tube triggers easily and with a short delay

and low jitter, and the turn-on time is materially decreased. The shortened ionization time constant allows operation at high rates of anode current rise, and anode heating is reduced.*

In most thyratron designs, a compromise is obtained between holdoff and triggering characteristics; for a given electrode spacing, the nominal gas pressure is chosen such that the holdoff is adequate and the triggering characteristics are acceptable.

In high voltage, low inductance tubes where a certain current rise time is specified, no pressure compromise is possible. The gas pressure must be high enough to ensure a sufficiently fast anode fall. The holdoff per stage and the isolation between stages must be maximized so that a minimum number of stages will provide the required total holdoff. If that minimum number of stages entails so much inductance that the required anode current rise time cannot be achieved, the design fails.

Because it is absolutely required that a low inductance thyratron operate at high pressure, investigation of holdoff was limited to the high pressure regime. As a practical matter, investigations would have been limited to high pressure in any event since, except for a brief period, available test equipment was limited to $e_{py} = 80$ kV. The three experimental multistage tubes that served as vehicles for most of our investigations were clearly capable of operation with e_{py} far in excess of 80 kV at gas pressures where each would have easily triggered and commutated through.

Test Procedure

Each of the experimental tubes was processed in a standard manner except that, before pinch-off, the reservoir was ranged to generate a deuterium pressure/reservoir voltage calibration curve. (One such curve is shown in Figure 34.) For all of the experimental work, the tube pressure was inferred from such curves.

*It is assumed that the total circuit inductance is not zero. In a zero-inductance case, the anode heating is severe.

After pinch-off, each tube was operated in a standard test kit to condition its cathode and to provide at least some degree of pre-aging. Although the tubes were of multi-gap construction, their minimum epy was reasonably low even at low gas pressures (see data for HY-5509 — Figure 35), so operation in a standard kit was readily accomplished. After a few hours' operation at $e_{py} = 30\text{-}40\text{ kV}$ and $I_b = 1\text{ A}$, the tubes were installed in the 80 kV test kit where the aging process began in earnest.

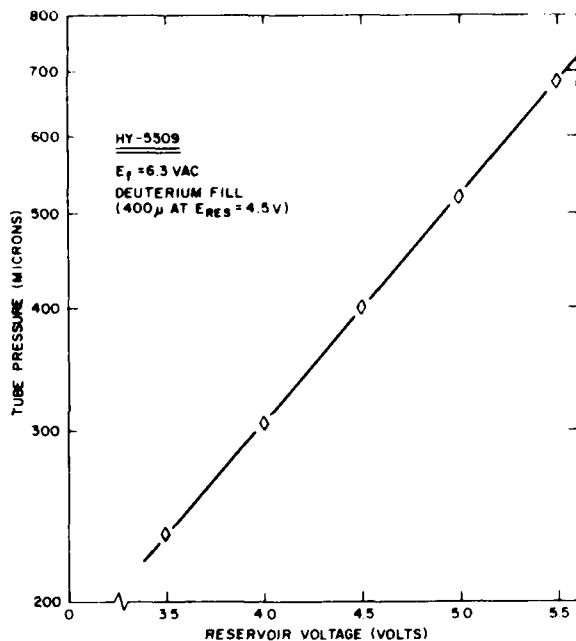


Figure 34. Typical reservoir calibration curve. The breakdown data obtained through the use of this curve were highly repeatable.

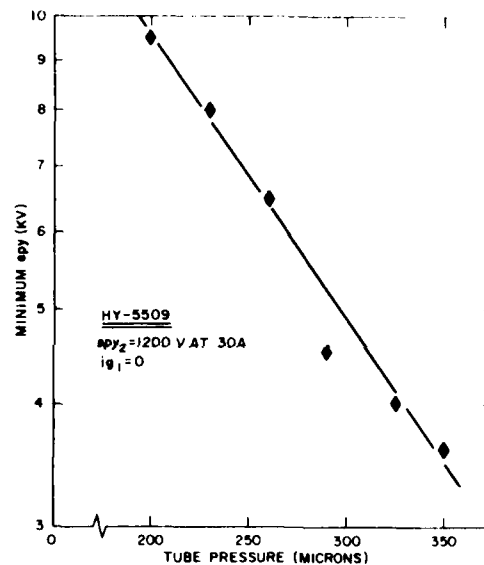


Figure 35. Minimum epy for the HY-5509. Although the tubes were of multi-gap construction, minimum epy was reasonably low.

It required typically 40 hours or more to pulse-age each tube. In general this was done stage-by-stage, starting with only the lower stage in operation and all other stages short-circuited to the anode. (In this case, the first gradient grid served as the actual anode.)

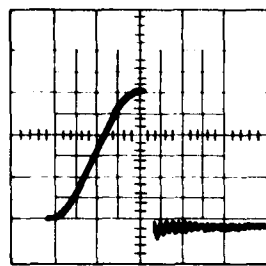
It was also possible to age the upper stages individually by resistively loading the lower stages such that the voltage across them was low by comparison with that across the stage being aged, and yet high enough so that commutation could occur.

It was also possible to generate some experimental data even when the tubes were not fully aged. This saved time and also provided insight into the tube operating characteristics that was useful to accelerate the aging process itself. One example of this was an investigation to verify that the applied anode voltage was capacitively distributed across the various gaps, and that the distribution could in fact be predicted from the geometries of the tube and its coaxial current return without taking their finite lengths into account. Data showing the stage-to-ground voltages of the 5-stage HY-5506 appear in Figure 36. (The dwell had been set to zero to minimize the stress on the probe used to measure the grid voltages.) The difference between the calculated and observed voltages was approximately 10%, and even this small discrepancy could be resolved when the capacitive loading introduced by the probe was taken into account.

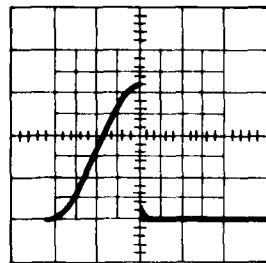
Breakdown Characteristics — Data

After the tubes had been fully aged, their high-pressure breakdown characteristics were established with the results shown in Figures 37 (HY-5506), 38 (HY-5508), and 39 (HY-5509).^{*} These tests were limited to 80 kV by the characteristics of the test kit, and not by those of the tubes themselves. For a brief period, the 250 kV kit was accessible, but at that time it was operable up to only 120 kV. The HY-5509 was operated in the high voltage kit with epy up to 118 kV as shown in Figure 40. Note from Figure 40

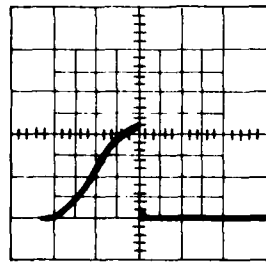
^{*}The DBV data were generated with a dwell of 2 μ S in accordance with the results discussed in Section 7c(2). No SBV data were generated for the HY-5508.



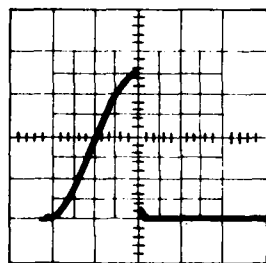
V₅
16 KV/MAJ. DIV.



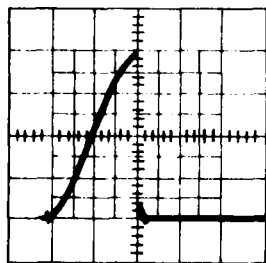
V₄
10 KV/MAJ. DIV.



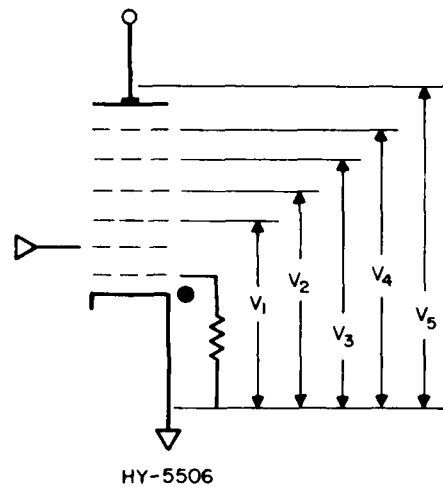
V₃
10 KV/MAJ. DIV.



V₂
4 KV/MAJ. DIV.



V₁
2 KV/MAJ. DIV.



	CALCULATED KV	OBSERVED KV	%ERROR
V ₁	7.8	7.9	-1.3
V ₂	16.1	14.0	13.0
V ₃	25.4	22.0	13.4
V ₄	36.3	32.5	10.5
V ₅	—	49.5	—

Figure 36. Distribution of charging voltage — HY-5506. The calculated and observed stage voltages were in reasonable agreement.

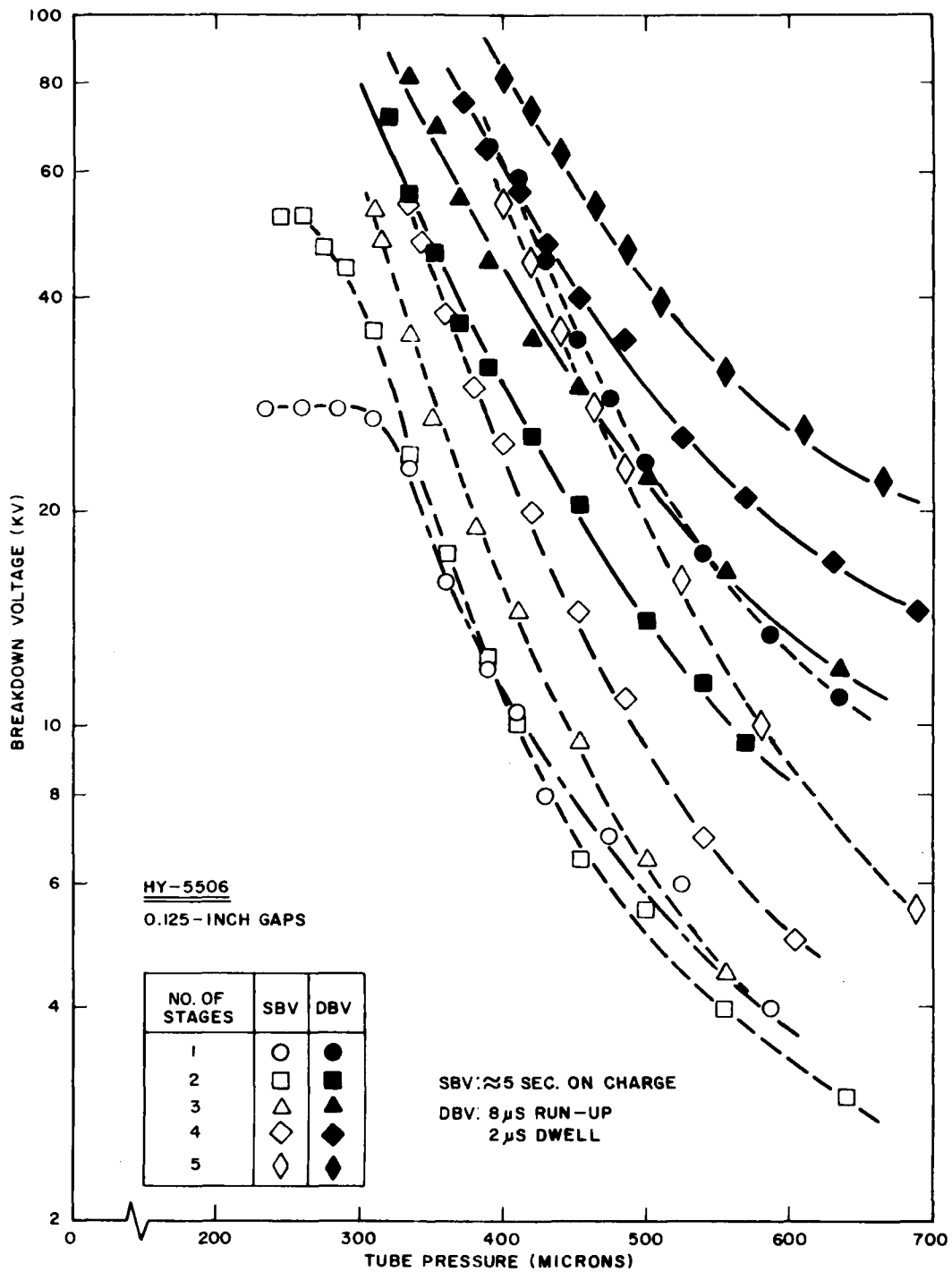


Figure 37. Breakdown characteristics - HY-5506. The stage voltages were not additive.

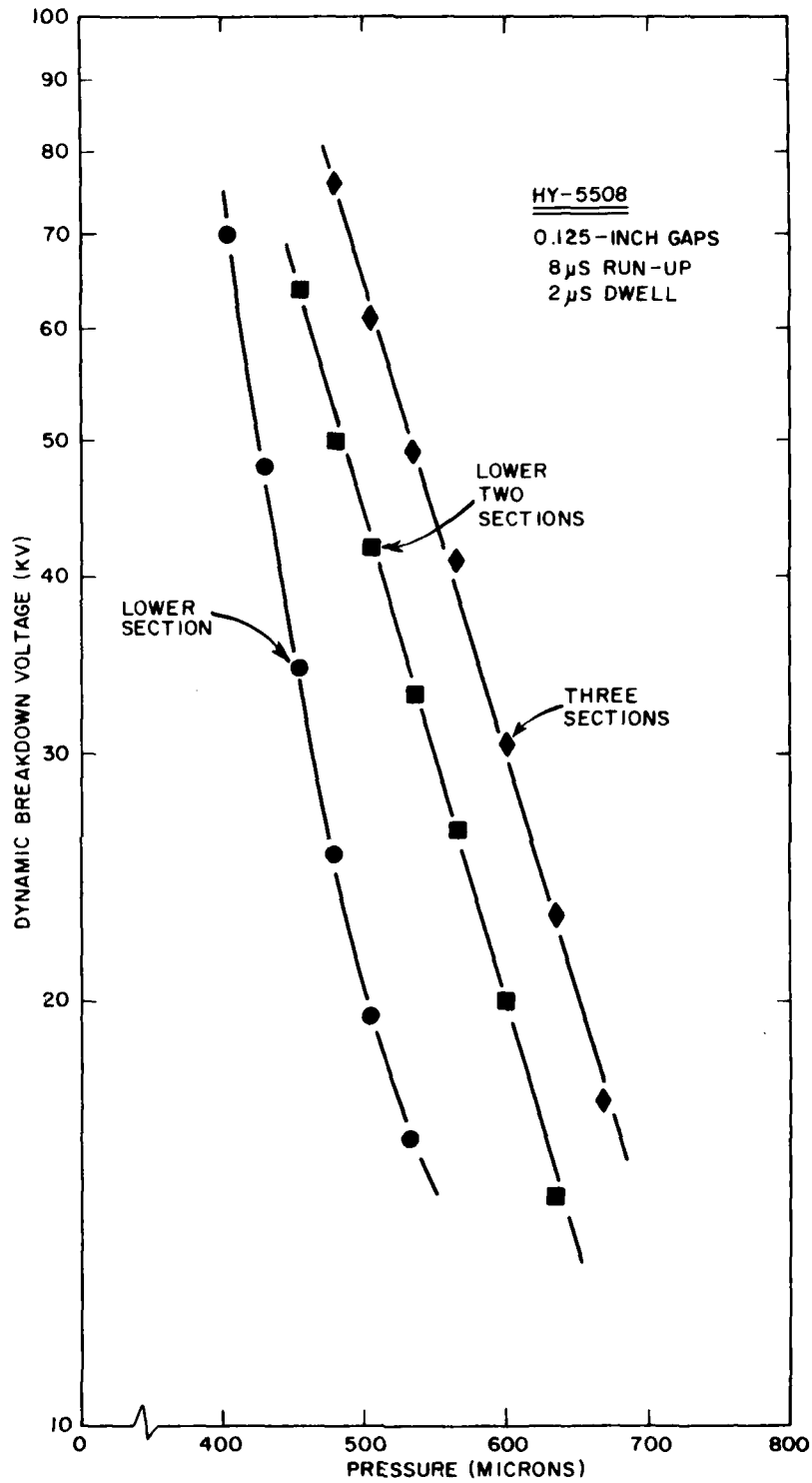


Figure 38. Breakdown characteristics — HY-5508. Near-perfect stage voltage addition was achieved.

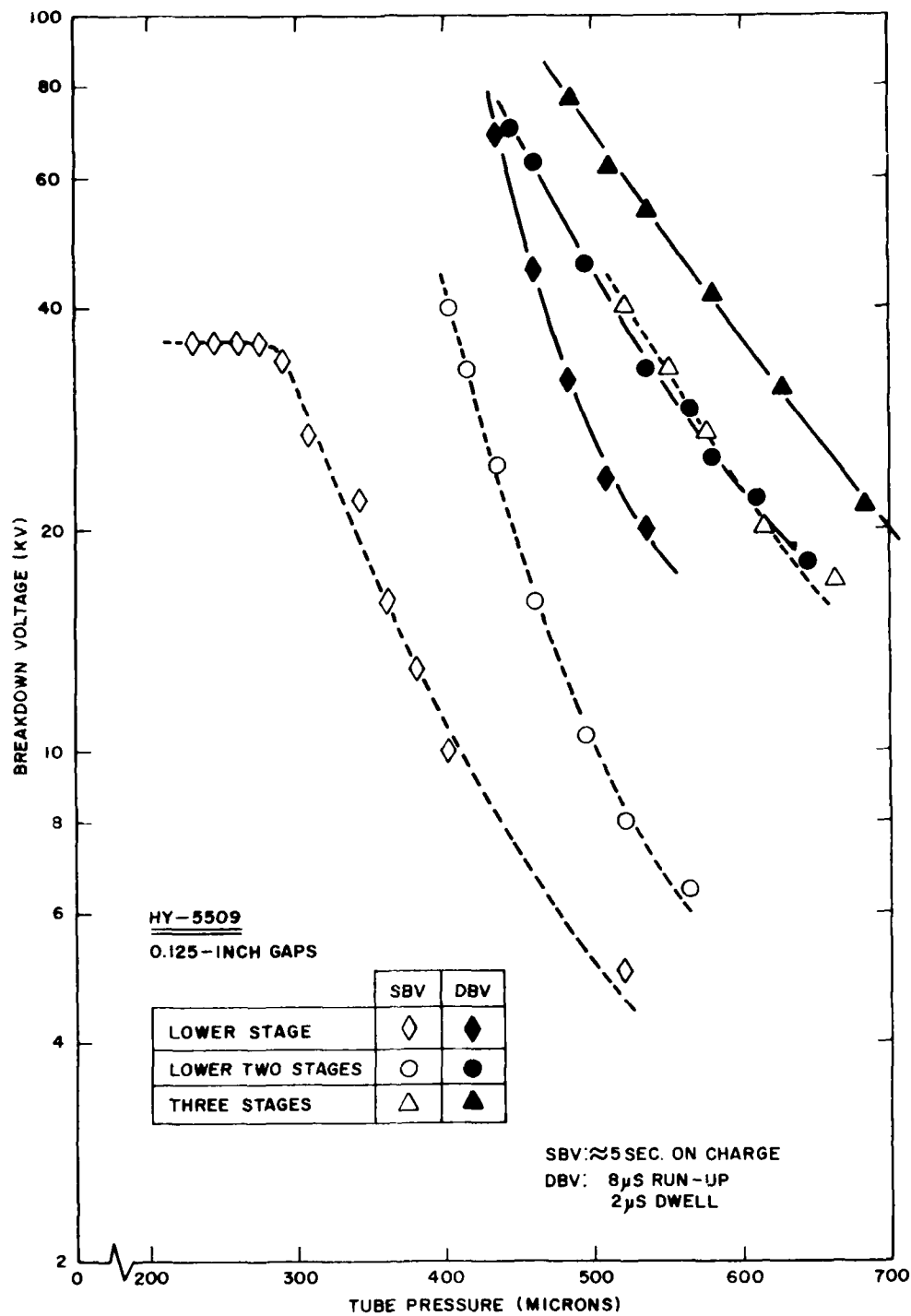


Figure 39. Breakdown characteristics - HY-5509. This moderately baffled tube had reasonable stage voltage addition properties and high total holdoff.

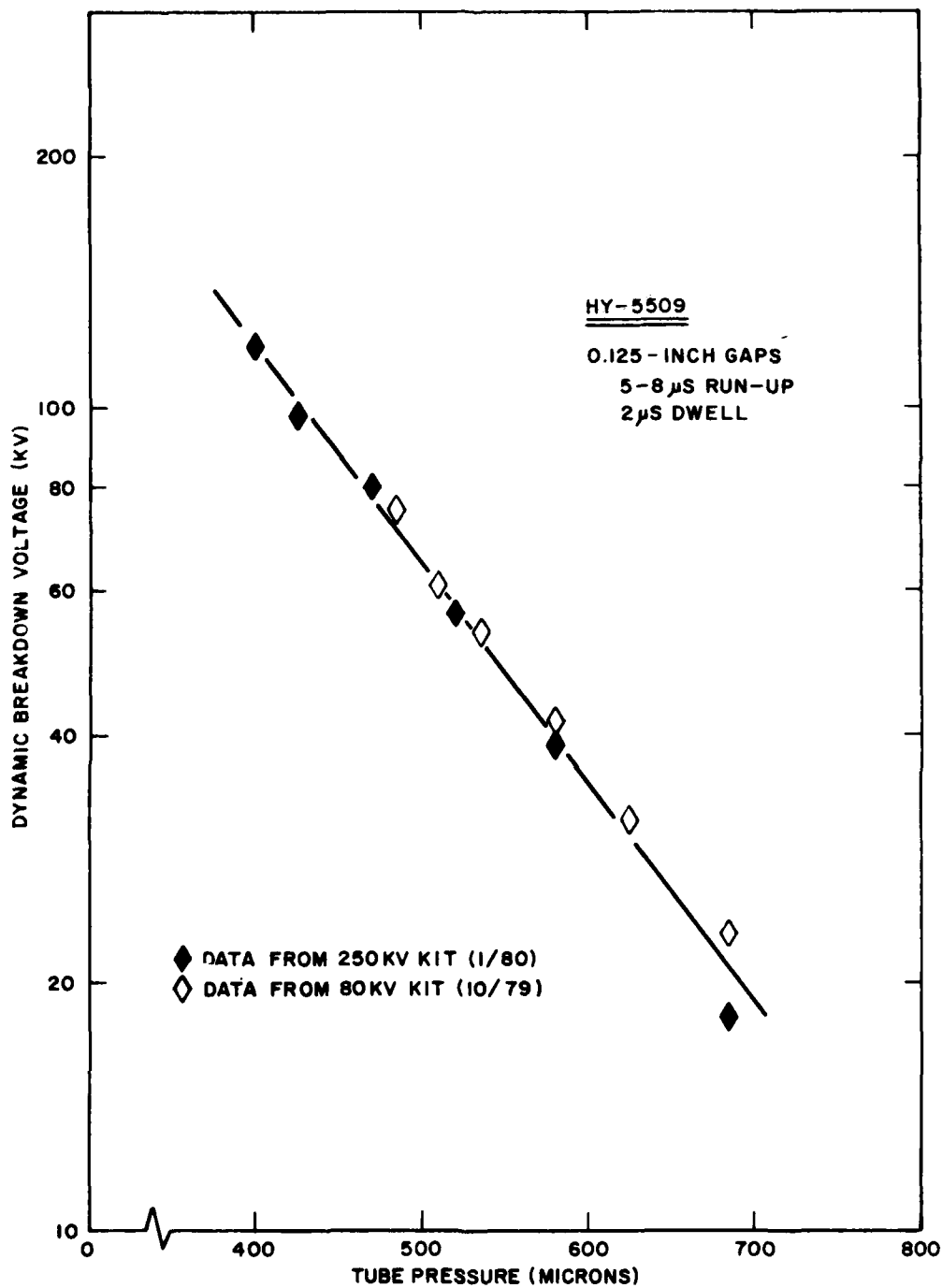


Figure 40. Dynamic breakdown characteristics — HY-5509. The 118 kV holdoff at 400 microns was the highest achieved during Phase II. The curve extrapolates to 200 kV at 315 microns — a pressure where the tube commutated readily and had an anode fall time of 40 nanoseconds.

that the data can be extrapolated to $ep_y = 200$ kV at 315 microns — a pressure where the tube commutated readily and had an anode fall time of 40 nS.* The subsequent failure of the test kit precluded any further testing of the experimental tubes at high ep_y .**

Breakdown Characteristics — Discussion

Considerable experimental work was required, first to generate, and then to understand the various curves of Figures 37 through 39. Section 7c(2) of this report discusses the effects of the dwell time on the dynamic holdoff voltage. Section 5a(3) presents the principles of stage voltage addition, and Section 7c(4) gives the experimental results that support the voltage addition analysis.

Even a cursory examination of Figure 37 (HY-5506) shows why such a heavy emphasis has been placed on grid transfer efficiency and on stage voltage addition in general. It is clear that the various stages of the HY-5506 were insufficiently isolated from one another — so much so that under dynamic charging conditions, four stages were required to equal or exceed the holdoff of the first stage alone. In contrast, the tightly baffled HY-5508 operated with near-perfect stage voltage addition as an examination of Figure 38 reveals.

Figure 41 shows (on a single plot) the DBV for the first stage and the DBV for all stages of each of the three tubes. Figure 41 shows that despite the near-perfect stage voltage addition properties of the HY-5508, the intermediately baffled HY-5509 provided the best total holdoff. This situation is attributed to the relatively poor performance of the 5508 first stage, as shown by the appropriate curves of Figure 41. This is not to say that the first stage always dominates tube performance; it is the weakest stage that does so. In general, however, the first stage is usually the weakest and therefore the dominant stage.

The various DBV curves corresponding to "all stages" as discussed so far in this subsection do not necessarily represent the maximum possible ep_y for the particular tube in question. In general, it was possible to operate each

*See Figure 51.

**See Section 6c.

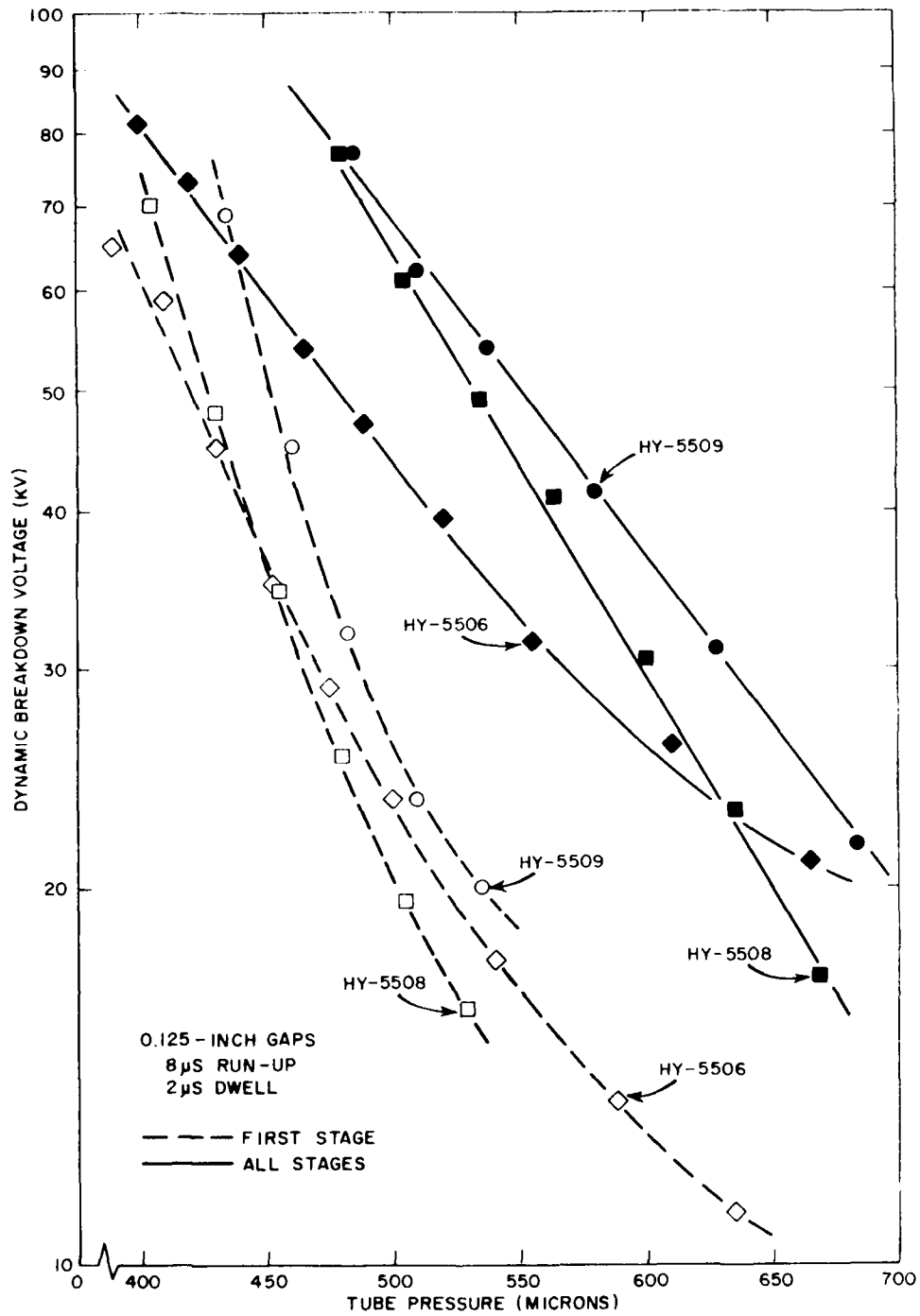


Figure 41. Comparison of DBV - HY-5506, HY-5508, and HY-5509. The HY-5509 had the best anode characteristic because of its relatively strong first stage and good stage voltage addition properties.

tube under conditions where higher epy could be achieved. Figure 42 shows an example of such operation with the HY-5509. To avoid the limitation imposed on epy by the relatively weak first stage, this stage was resistively shunted with a 40 K resistor. This forced the applied voltage to be substantially distributed across the relatively strong upper stages, while also providing a first-stage voltage just high enough to promote commutation. The result was a higher total breakdown voltage as Figure 42 shows.

The most important single advance that could be made during this Program would be to devise a means for increasing the DBV per stage at high gas pressures. Figure 43 shows the results of an investigation of the high-pressure dynamic breakdown characteristics of four well-aged, single-gap tubes as a function of their gap spacings. As expected, and in accordance with the Paschen curve, the dynamic breakdown voltage at any given gas pressure is an inverse function of the gap spacing, except for the 75 mil gap. It was not clear why the small gap yielded anomalous data, so the tube was repumped and the data retaken. The second data agreed with the first, suggesting that (barring mechanical irregularities in the holdoff region) some form of field enhancement may exist in these tubes, and that its effects dominate holdoff at small gap spacings. Field irregularities introduced by the walls or by the grid apertures could lower the DBV, and there is other support for speculating that subtle breakdown mechanisms might be possible.

Consider, for example, the DBV curve for the 125-mil gap (HY-5313) of Figure 43, and that for the first stage of any of the multi-gap tubes (Figure 41). To generate the first-stage data, the multi-gap tubes were operated with their first gradient grids serving as anodes; they were in effect single-gap tubes with E-E spacings of 125 mils. Yet the DBV characteristic of the HY-5313 is far superior to that of any of the multi-stage tubes. This suggests that the apertures of the first gradient grid (anode for single-stage operation) serve to lower the DBV, either by field enhancement, or by creating a long discharge path between the bottom of the gradient grid baffle and the top of the control grid. Furthermore, a large volume of gas is contained within a box grid that is being operated as an anode. Even a very low level of residual ionization in this gas may be sufficient to reduce the DBV of the stage below. Certainly such an effect is to be expected at high pulse repetition rates (see Section 7c(5)).

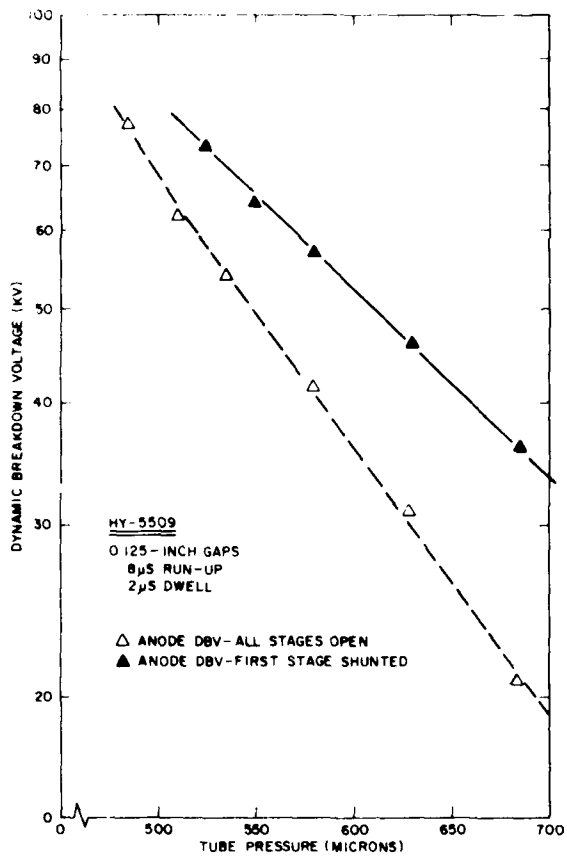


Figure 42. Anode DBV — HY-5509 with first stage shunted. Most of the applied voltage was distributed across the relatively strong upper stages.

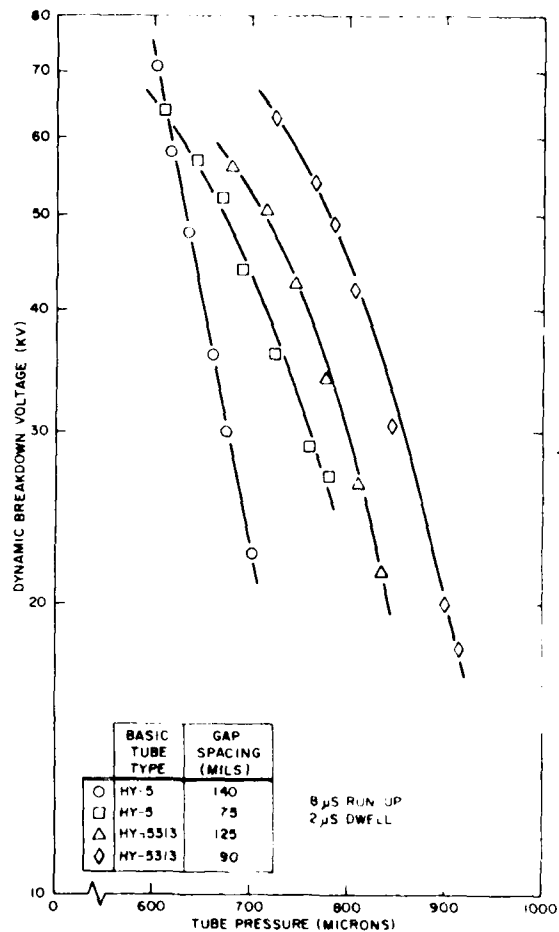


Figure 43. DBV as a function of pressure, with gap spacing as a parameter — various single stage tubes. The data for the 75-mil gap did not follow the trend set by the larger gaps.

Wall-related field effects and the discharge debris that collects on and near the walls could also be involved in establishing the breakdown characteristics of hydrogen thyratrons. After even a relatively short aging period, a thin film of previously vaporized anode material (generally molybdenum) collects on the inner surface of the holdoff section insulator. After prolonged operation, the thickness of this film becomes significant. While such deposits are not known to degrade holdoff, it is also not known what the holdoff might be if such deposits were not present. Much the same can be said of ablated wall material that collects on the surfaces of the electrodes.

Two insulator/electrode designs have been developed that (in principle) avoid both field enhancement and the buildup of debris near the discharge space. It is planned to test both designs during the coming year, and to use the computer field plotting technique to evaluate the effects of various known mechanisms that might provide significant field enhancement in the inter-electrode space.

(4) Stage Voltage Addition

It is implicit in the concept of multi-stage tubes that the holdoff voltages of the individual stages be additive to yield a high anode holdoff voltage. However, algebraic addition does not necessarily occur, as the breakdown characteristics of the HY-5506 (Figure 37) clearly show.

In Section 5a(3) simple expressions were derived for the anode breakdown voltage of a multi-stage tube in terms of the breakdown voltage of its weakest stage and the degree of isolation between its adjacent stages. The analysis yielded the relations

$$\alpha = \frac{V_x}{2V_0}, \quad (4)$$

$$V_A = \alpha NV_0 \quad (5)$$

and

$$V_A = \frac{N}{2} V_x \quad (6)$$

where N is the number of stages, V_0 is the breakdown voltage of the weakest stage (alone), V_x is the breakdown voltage of the combination consisting of the weakest stage in series with an adjacent stage, and V_A is the anode breakdown voltage.

Equation (4) defines the tube isolation coefficient, α . When $\alpha = 1$, $V_x = 2V_0$ and $V_A = NV_0$; perfect voltage addition occurs.

The data shown in Tables 10 through 12 illustrate the voltage addition properties of multi-stage tubes having different gradient grid baffling, and therefore different isolation coefficients. Consider first Table 10, which shows data for the HY-5506.* Note that V_x , DBV for two adjacent stages (including the weakest), is less than V_0 , the breakdown voltage of the weakest stage alone. As a result, the isolation coefficient, α , is materially less than unity. Various columns of Table 10 show the calculated and observed DBVs for three, four, and five stages. Note that the observed DBVs exceed the calculated DBVs in every case. This is consistent with capacitance-controlled voltage division and our observation that the upper stages of a multi-stage tube tend to have a higher DBV than do the lower stages. As a result, the percentage of error increases as more stages are added. Data of the same general nature are shown in Tables 11 and 12 for the HY-5508 and the HY-5509, respectively. The isolation coefficient of the moderately baffled 5509 is about 0.8, while that of the highly baffled 5508 approaches unity.

The complete breakdown characteristics of the HY-5508 were shown in Figure 38. In general, the two-stage DBV was twice the single-stage DBV, and the three-stage DBV exceeded the two-stage DBV by 50%. Near-perfect stage voltage addition was thus achieved with this tube.

When the isolation coefficient, α , of a given grid structure is known from experimental data, the grid voltage addition properties can be related to its calculated transfer efficiency, γ , as discussed in Section 5b(1). Using the data of this subsection, the curve of α vs γ shown in Figure 15 was generated, and from this curve an optimum $\gamma \approx 10^{-4}$ was inferred. Once the α vs γ characteristic is known, the computer can aid in the design of specific grid structures having good stage voltage addition properties, since any grid having $\gamma \approx 10^{-4}$ should yield near-perfect stage voltage addition.

*The blanks in the tables correspond to conditions where the characteristics of the test kit precluded the generation of data.

Table 10. Calculated and measured anode breakdown voltages for HY-5506.

Pressure (Microns)	V ₀ (kV) (Note 1)	V _x (kV) (Note 2)	α	V _{A3} (kV) (Note 3)		V _{A4} (kV)		V _{A5} (kV)	
				Calculated	Observed	Calculated	Observed	Calculated	Observed
352	64	51	0.40	76.8	--	--	--	--	--
370	54	42	0.39	63.2	64	--	--	--	--
390	44	34	0.39	51.5	54	68.6	77	--	--
410	--	28	--	42	44	56	63.5	--	--
430	--	25	--	37.5	38	50	54	62.5	73

Note 1. Weakest stage is Stage 2. All data for 2 μs dwell times.

Note 2. Stage 2 and Stage 1 in series.

Note 3. Subscript A3 indicates holdoff for three stages, A4 indicates four stages, etc. Voltages were calculated from relations $V_A = \alpha N V_0$ or $V_A = \frac{N}{2} V_x$ as appropriate.

Table 11. Calculated and measured anode breakdown voltages for HY-5508.

Pressure (Microns)	V_0 (kV) (Note 1)	V_x (kV) (Note 2)	α	V_A (kV) (Note 3)	
				Calculated	Observed
454	35	64	0.91	95.6	--
467	30	57	0.95	85.5	--
480	27	52	0.96	77.8	80
492	23.5	46	0.98	69.1	70
520	--	37	--	55.5	56
550	--	30	--	45	45
582	--	23	--	34.5	36

Note 1. Weakest stage is Stage 1. All data for 2 μ S dwell times.

Note 2. Stage 1 and Stage 2 in series.

Note 3. V_A indicates holdoff for three stages. Voltages were calculated from relations $V_A = \alpha N V_0$ or $V_A = \frac{N}{2} V_x$ as appropriate. Tube was not fully aged at time data were taken.

Table 12. Calculated and measured anode breakdown voltages for HY-5509.

Pressure (Microns)	V_0 (kV) (Note 1)	V_x (kV) (Note 2)	α	V_A (kV) (Note 3)	
				Calculated	Observed
447	48	70	0.73	105	--
470	35	55	0.79	83	--
494	27	44	0.82	66.4	68
522	21.5	34	0.79	51	57

Note 1. Weakest stage is Stage 1. All data for 2 μ S dwell times.

Note 2. Stage 1 and Stage 2 in series.

Note 3. V_A indicates holdoff for three stages. Voltages were calculated from relation $V_A = \alpha NV_0$.

There is a significant advantage in being able to predict the multi-stage tube overall breakdown characteristics on the basis of the characteristics of just a few of its stages. From admittedly sparse data, the isolation coefficient appears to be somewhat pressure-sensitive, with the trend being such that better voltage addition occurs at higher pressures. (See, for example, Table 11 and the DBV curves of Figures 37 and 38.) Alternatively, it might be that the higher fields attendant to operation at low pressures cause the voltage addition properties to degrade. In either case, costly and time-consuming errors can be avoided in the implementation of very high voltage tubes by first building and characterizing a three-stage device. When the exact voltage addition properties of the three-stage tube have been determined, the properties of the full-scale device can be predicted with confidence.

(5) Operation at High Pulse Repetition Rates

The fundamental limit on thyratron repetition rate capability is set by the time required for the gas in the tube to deionize such that high voltage holdoff is recovered. Although only a fraction of the gas in the tube is ionized during conduction, this ionization must decay to near-zero before recovery can occur. Deionization and recovery are strongly affected by both the tube geometry and the nature of the external circuit.

Deionization results from ambipolar diffusion to the electrode surfaces such that wall-assisted recombination can occur. The time constant of the plasma decay varies with the gas pressure and with the square of the physical dimensions that define the volume of the gas discharge.

Tubes having physically large discharge dimensions will thus operate with relatively long recovery times. Multi-gap, cavity-type tubes are an example. In general, their recovery characteristics are an order of magnitude slower than those of single-stage tubes capable of operating at the same power level. Although the discharge dimensions of multi-stage, box-gridded tubes are in general much smaller than those of cavity types having equivalent voltage ratings, they are materially larger than those of single-stage tubes. It is therefore reasonable to assume that the recovery characteristics of box-gridded tubes will fall naturally into position between those of the slower cavity types and those of the faster single-stage tubes.

To investigate the recovery characteristics of the multi-stage tubes built during Phase II, the tubes in the 80 kV test kit were operated under burst-mode conditions (refer to Figure 24). Operation in the burst mode permitted examination of the effects of residual ionization on tube dynamic breakdown characteristics without encountering such complications as might arise under conditions where the average heating was significant.

To establish a control case, a standard EG&G Type HY-5 was tested first, and the results are shown in Figure 44. To generate the data of Figure 44, a burst of two pulses (at a low burst rate) was applied to the tube, with the period between pulses (t_1) being more than long enough so that $DBV_2 = DBV_1$ at a given gas pressure, P . The interpulse time was then decreased until any further reductions caused DBV_2 to be less than DBV_1 . The value of t_1 so determined was thus the minimum period required for the tube to recover holdoff to DBV_1 . Further reductions of t_1 caused DBV_2 to decrease in the manner shown by Figure 44.

The data of Figure 44 are difficult to analyze in a phenomenological sense. To aid in the analysis, a figure of merit, recovery factor, ρ , was devised, where ρ is defined by the relation

$$\rho = \frac{P(DBV)}{t_1} \quad (53)$$

where P is the tube pressure in microns, DBV is the low-prr dynamic breakdown voltage at the pressure P , and t_1 is the minimum interpulse time such that $DBV_2 = DBV_1 = DBV$.

Tubes having a large recovery factor will operate at high pressure (for high di/dt and low anode dissipation), have a high dynamic breakdown voltage (for high epv), and yet have a short recovery time (for high prr).

When the recovery factor as defined above is computed from the data of Figure 44, the curve of Figure 45 results. Figure 45 shows the extent to which the steepness of the DBV characteristic and the pressure dependence of diffusion-controlled recovery combine to limit tube capabilities at high gas pressures.

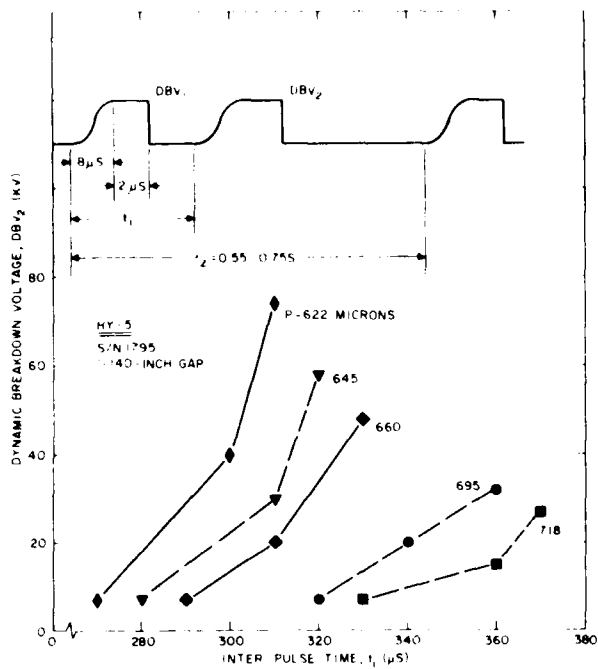


Figure 44. Breakdown characteristics at high pr - HY-5. Average heating was low, thus the breakdown characteristics were dominated by residual ionization only.

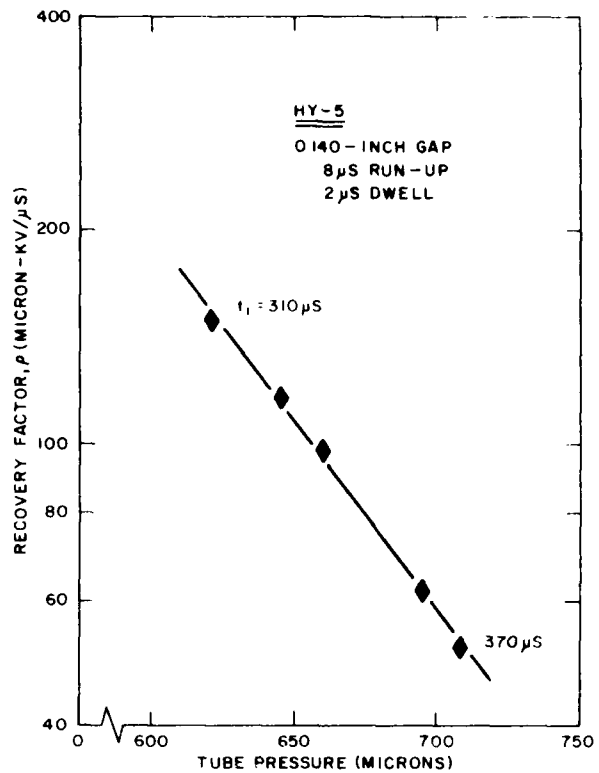


Figure 45. Recovery factor at high pressures - HY-5. A high recovery factor means a high DBV at high pressure, coupled with a short recovery time.

Data similar to that shown in Figure 44 were generated for the HY-5506, 5508, and 5509, and the results are shown in Figures 46 through 48, respectively. Figure 49 shows the recovery factor for each of the multi-gap tubes and also that of the HY-5 for purposes of comparison. As expected, all of the multi-gap tubes operated with recovery factors materially poorer than that of the single-stage HY-5. It is, however, important to note the trend of improvement from the 5506 to the 5509 to the 5508. The five-stage, unbaffled 5506 had the poorest DBV characteristic (Figure 41) and the largest physical dimensions. It is therefore not surprising that the 5506 had the poorest recovery factor. Both the 5508 and the 5509 (three-stage tubes) had the same physical dimensions except for the thicker gradient grid baffles used in the 5508. Of the latter two tubes, the 5508 had the best recovery factor (as

shown by Figure 49) despite the fact that the 5509 had a slightly better DBV characteristic as shown by Figure 41. It is suspected that the 5508 higher recovery factor was due to the shorter diffusion distances that resulted from the thicker gradient grid baffles.

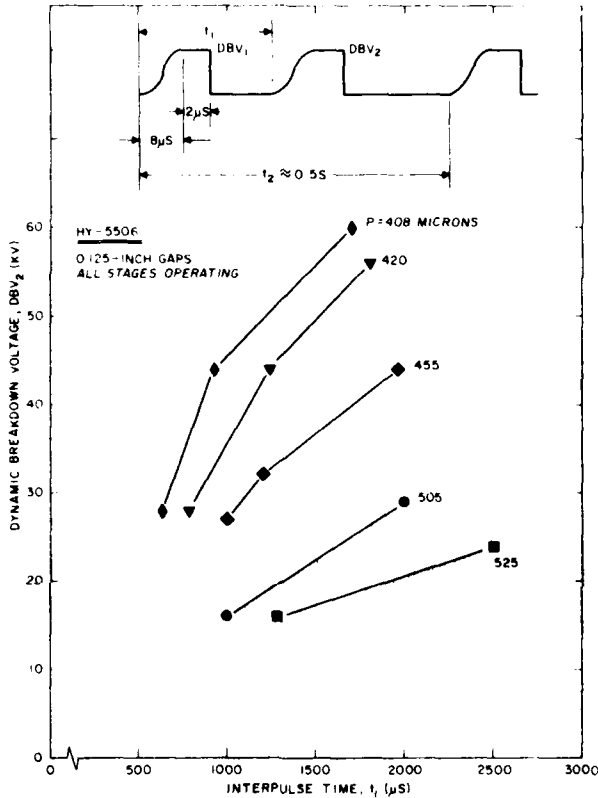


Figure 46. Breakdown characteristics at high prr - HY-5506.

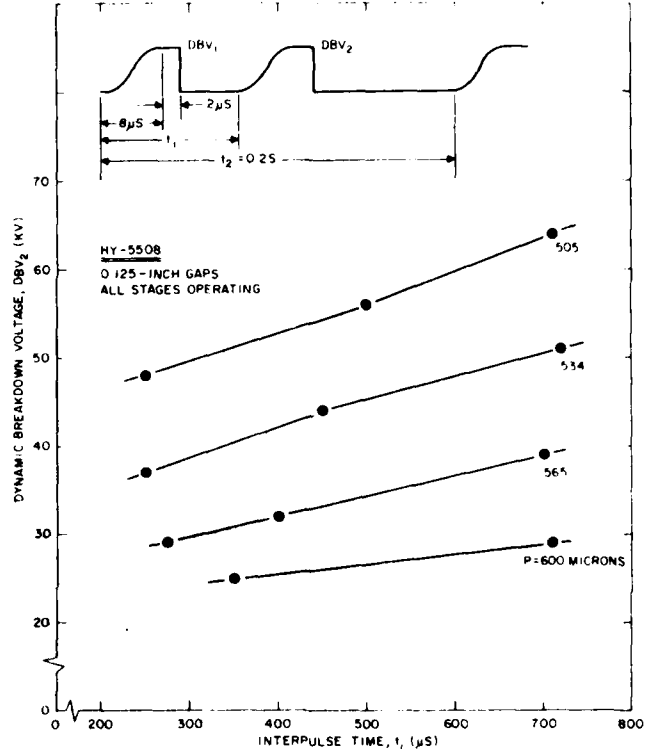


Figure 47. Breakdown characteristics at high prr - HY-5508.

The recovery investigations reported here are not exhaustive, nor were they intended to be. The purpose of this work was to establish the framework within which future investigations must lie. From Figure 49, it was concluded that the recovery characteristics of multi-stage box-grid tubes are less than a factor of 10 poorer than those of single-stage devices - not an enormous differential. It is nonetheless clear that considerable future work will be required to develop high voltage, low inductance tubes that are capable of operating at significant pulse repetition rates.

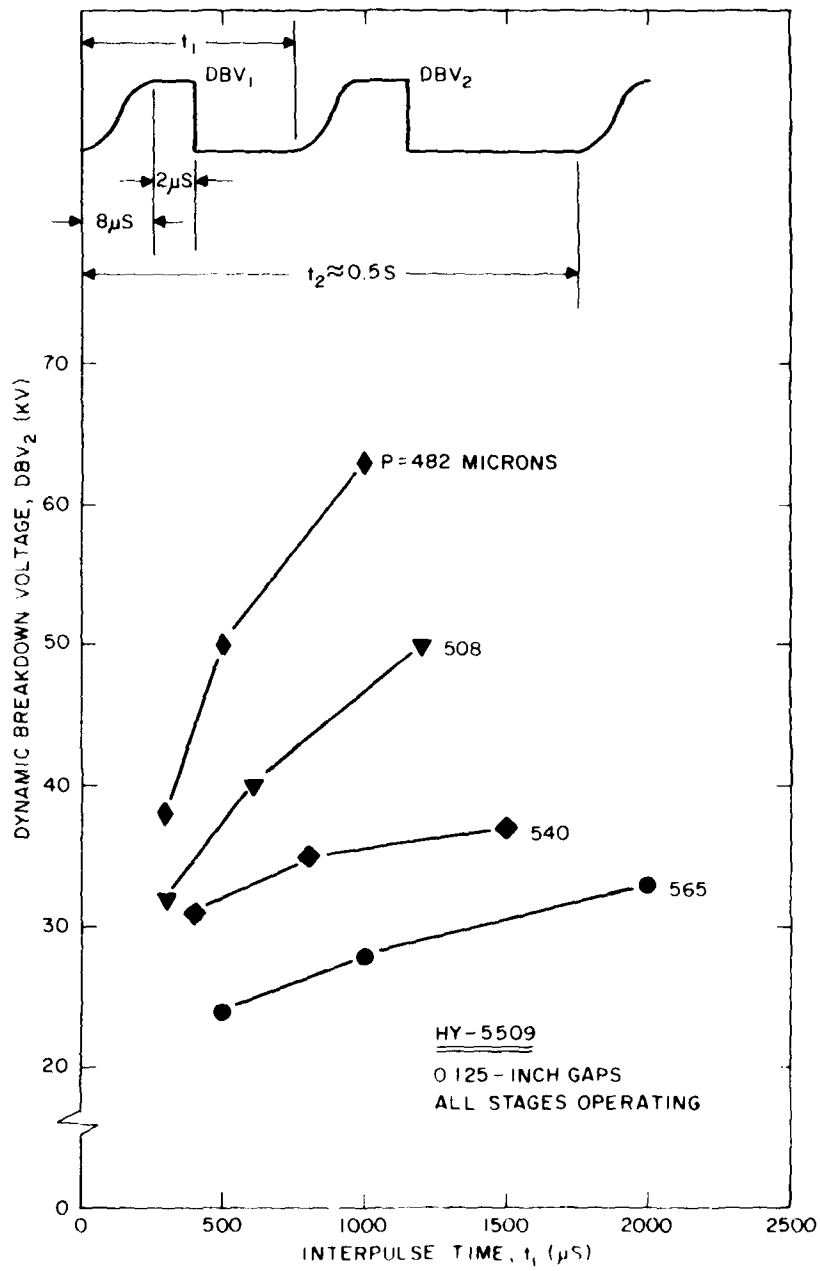


Figure 48. Breakdown characteristics at high ppr - HY-5509.

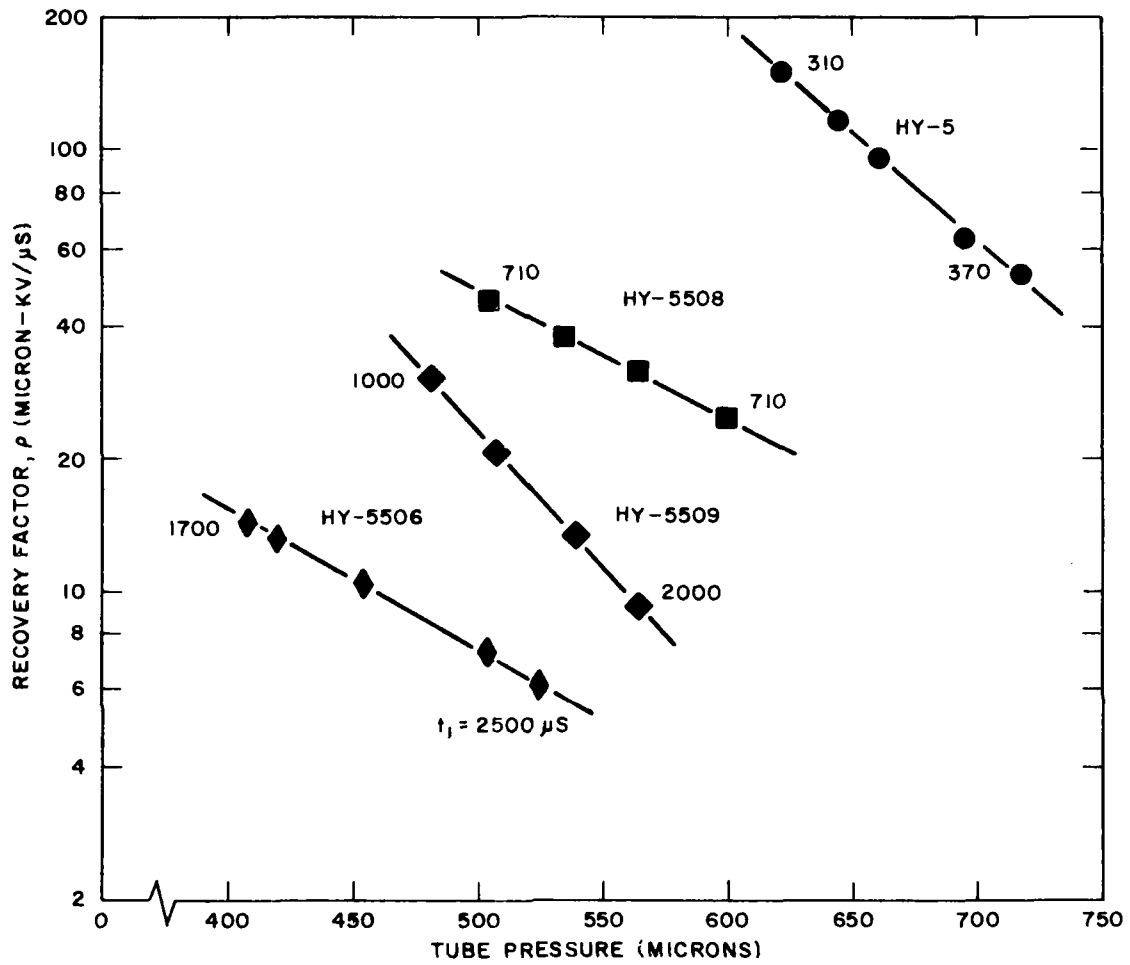


Figure 49. Comparison of recovery factors — multistage tubes and HY-5. The HY-5508 had the best recovery characteristics of the multistage tubes. This was probably due to the shorter diffusion distances that resulted from the relatively thick gradient grid baffles of the tube.

(6) Current Rise Time vs Gas Pressure

The three experimental tubes were operated in the high di/dt test kit to determine their anode current rise times as a function of gas pressure. A typical oscillogram showing the shape of the current pulse (at high pressure) is given as Figure 50. The peak anode current was maintained constant at 3 kA and the tubes were control-grid triggered with the auxiliary grid grounded through 100 ohms.

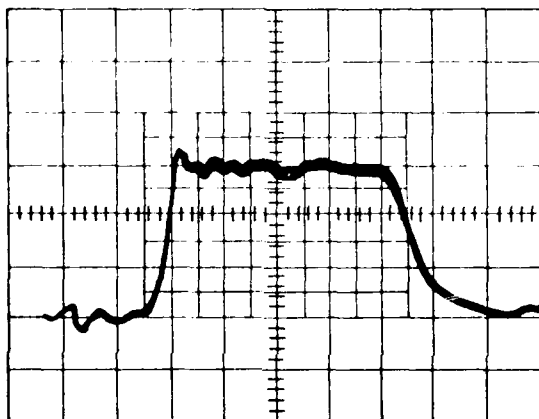


Figure 50. A typical anode current pulse at high gas pressure. The 3 kA pulse shown was generated by the HY-5506 in the high di/dt test kit. The rise time of the pulse is 10 ns. The current rise time was dominated by the anode fall time.

Figure 51 shows t_r (10-90%) as a function of P for the three tubes. The rise time characteristics are substantially the same; those of the higher-inductance HY-5506 and the highly baffled HY-5508 are identical,* and the 50 micron shift observed for the HY-5509 could easily be the result of some

*It was assumed that the HY-5506 had a higher inductance because of its two additional stages. However, the three-stage, baffled tubes could have had a somewhat higher inductance than that calculated on the basis of their geometries because of the tortuous discharge path introduced by the gradient grid baffles.

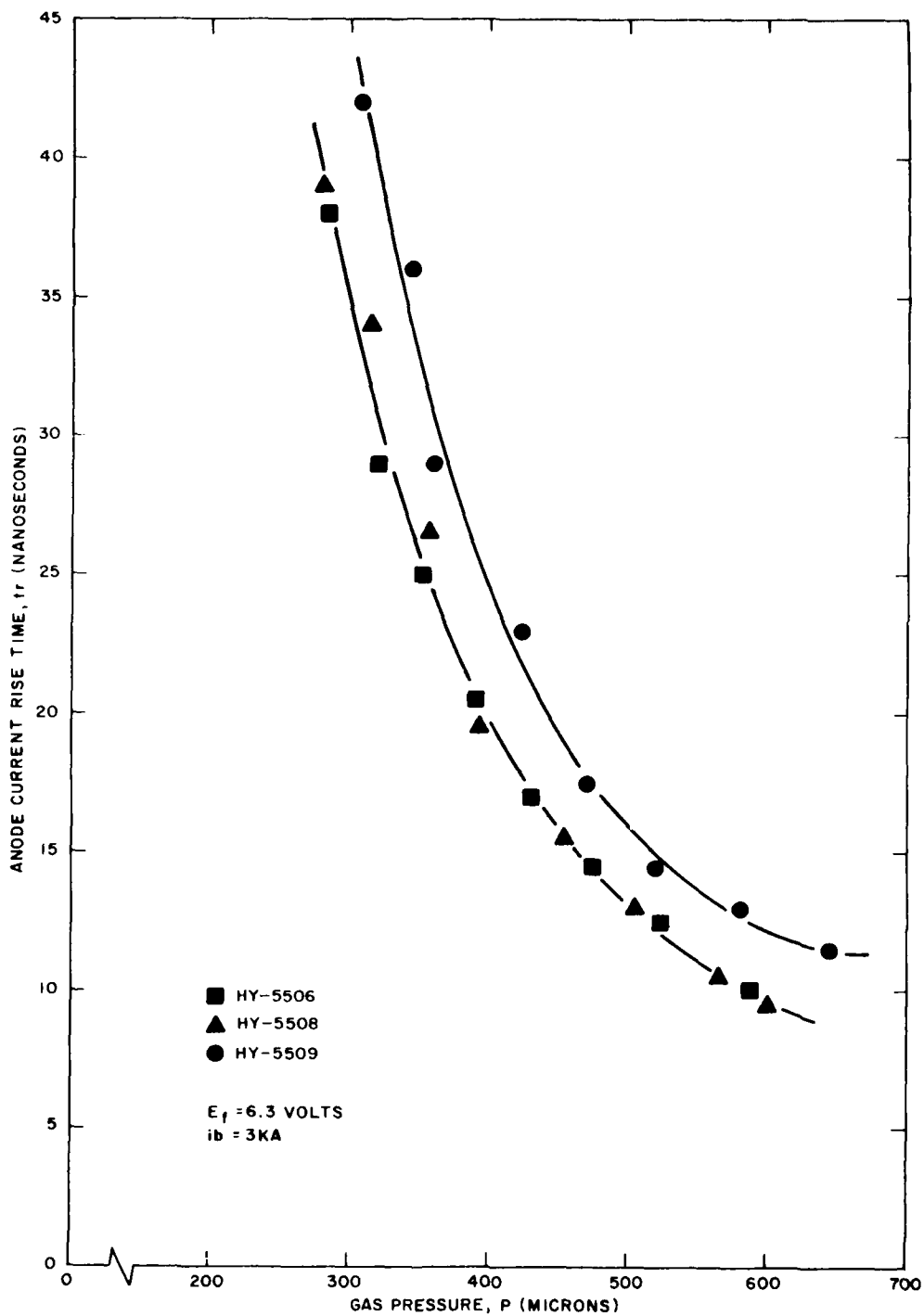


Figure 51. Rise time as a function of gas pressure — multistage tubes. The rise time characteristics of the three tubes were substantially the same.

pressure calibration error. The data are inconclusive regarding any correlation between rise time and inductance or degree of baffling. This is probably because over most of the pressure range investigated, t_r was in fact dominated by the resistive anode fall time; that is, by the turn-on time of the tubes, and not by the total circuit inductance. There is ample support for this contention as discussed further below.

As the gas pressure was increased, the rise time continued to decrease in a predictable fashion. No inductance-limited mode was observed. The rise time characteristics for the HY-5506 and HY-5508 (Figure 51) can be approximated by the relation

$$t_r = 1.52 \times 10^6 P^{-1.87} \quad (54)$$

where P is the pressure in microns and t_r is the rise time in nanoseconds. Equation (54) is accurate to 3% over the range of 300 to 600 microns. The rising portion of the anode current pulse was in general dominated by the exponential nature of the anode fall; it did not have the familiar inductance-controlled shape.

An experiment was performed to determine an upper bound for the inductance of the HY-5508. It yielded an upper limit of 58 nH for the tube, and a total circuit inductance that could be defined only as being slightly higher than the tube inductance. This measurement was consistent with a geometrically calculated tube inductance of 50 nH and an inductance of less than 10 nH for the balance of the circuit.

The HY-5508 was operated at high pressure in the relatively high inductance 80 kV pulse charge test kit, where its anode fall time was about 10 nS. When operated at the same pressure in the high di/dt test kit with $di/dt \approx 2 \times 10^{11}$ A/S, the anode fall time was again observed to be about 10 nS. Thus the drop, $L_T di/dt$, was low even at high di/dt . This indicates that the actual L_T was materially less than that value determined to be its upper bound.

The overall conclusions are that the inductance of the experimental tubes was low and that the rise of the anode current was thus dominated by the inherent anode fall time. The low tube inductance suggests that the discharge was substantially uniform even for a 3 kA current pulse rising in 10 nS. Even the five-stage HY-5506 had an inductance that was conservatively estimated to be less than 50 nH. Unless the constraints imposed by capacitive-controlled voltage division ultimately dictate to the contrary, the inherently low inductance of these designs means that additional stages could be added to increase their total forward holdoff without materially affecting their anode current rise times.

During the investigation described here, 3 kA current pulses such as that shown in Figure 50 were routinely generated by each of the experimental multi-stage tubes when operated with $e_{py} = 30$ kV. This corresponds to a di/dt per volt of 8×10^6 A/S/volt. From ERADCOM's applicable Technical Guidelines (Table 1), a di/dt per volt of 1.28×10^7 can be inferred, and this is a switching capability not far removed from that already demonstrated in the laboratory. The conclusion is that the inherent switching capabilities of hydrogen thyratrons are consistent with the needs of this Program.

(7) Triggering Characteristics

The important triggering characteristics are the sequence in which the gaps break down, the associated time jitter, and, to a lesser extent, the anode delay time. The amount of grid drive required to achieve acceptable triggering would not limit the utility of these tubes for most applications unless it were to become a significant fraction of the power being switched by the tube.

Breakdown Sequence

A hydrogen thyratron is a plasma-triggered device. In a multi-stage tube, that gap having the optimum combination of electric field and plasma density will break down first, and it is essential that the breakdown sequence be proper. Each stage must serve as a virtual cathode for the stage directly above it if upper stage arcing is to be avoided. Furthermore, as commutation proceeds toward the anode, the voltage across the upper stages increases until

the full anode voltage appears across the uppermost stage. The resultant insulator stress can be accommodated by grading the lengths of the insulators, but only when the firing sequence is reliable.

By viewing the voltage waveforms at the anode and the various gradient grids, the breakdown sequences for the HY-5506, 5508, and 5509 were determined. When the auxiliary grids were triggered, the breakdown sequences were in some cases erratic, but it is strongly suspected that the erratic behavior was linked to an improperly designed control grid baffle as discussed further below in connection with measurements of time jitter. When the control grids were triggered, the breakdown sequences were in all cases correct, i.e., the gaps broke down from the control grid to the anode. For types 5506 and 5509, control-grid triggering did result in an improper sequence if the time on charge approached the DBV time (the time beyond which the TUT could not hold off the applied voltage). For the HY-5508, the breakdown sequence was correct regardless of the time on charge.

The results are summarized as follows: 1) a design defect in the control grid baffle made the results of the auxiliary grid triggering tests inconclusive; 2) for control grid triggering of the relatively loosely baffled tubes (5506 and 5509), the breakdown sequence was proper, provided that the time on charge did not approach the DBV time; and 3) for the highly baffled 5508, the stages were so well isolated that a high triggering plasma density was always reached in the lower stages before the next gap could break down. Thus the firing sequence was always proper for the 5508.

The overall conclusion is that multi-stage, box-grid tubes can be made to commutate reliably in the proper sequence, although it remains to be shown that the proper sequence can be maintained at hundreds of kilovolts as opposed to a few tens of kilovolts — the level for which the present data apply.

Time Jitter

To measure the time jitter, the TUT was installed in the high di/dt test kit and the output of the coaxial current viewing resistor was monitored in the cathode circuit. The trigger current pulse observed at the instant of trigger breakdown thus served as a time reference. Conveniently, as

each stage commutated, its stray capacitance also discharged through the CVR. Finally, upon commutation of the last gap, the full anode current was observed. It was thus possible to use a single waveform (the CVR voltage output) to determine time jitter, the propagation time through each stage, and the total anode delay time.

The initial measurements of time jitter were discouraging. With control grid triggering, jitters of tens of nanoseconds were observed. As expected, the more highly baffled tubes were more prone to jitter, but even the 5506 (no gradient grid baffles) was not jitter-free. Auxiliary grid keep-alive and auxiliary grid triggering led to even more discouraging results in that t_j worsened or remained the same, and t_{ad} actually increased. Increasing the grid drive by a factor of two did in fact reduce t_j , but not to an acceptable level. The conclusion was that a fundamental design change would be required to reduce t_j .

The key seemed to be that increased t_{ad} accompanied the use of keep-alive, this being indicative of truly aberrant tube behavior. The conclusion was that the keep-alive was establishing a plasma in some region of the auxiliary grid-cathode space that was far removed from the apertures of the control grid baffle, and this line of reasoning led to a review of the design of the control and auxiliary grids.

To keep the tube inductance low, the apertures in the various grids had in general been located at the outer reaches of the tube, thereby constraining the discharge current to flow as closely as possible to the current in the external return. Because of the relatively small-diameter cathode, however, the apertures in the auxiliary grid were considerably farther from the tube sidewalls than were all other apertures. This resulted in a relatively large offset between the apertures in the auxiliary grid and those in the control grid baffle. It is highly likely that this offset was responsible for the jitter characteristics observed for these tubes.

To test the theory described above (and also to force a reasonable t_j), a high power trigger generator (egy up to 8 kV at 100 A) was built to flood the control grid-cathode space with triggering plasma. The reasoning was that an optimum plasma density might be generated to compensate for the excessive

offset without accelerating the electrons so much that they bombarded the lower surface of the control grid baffle instead of propagating to (and through) the baffle apertures.

This experiment worked, and with a drive of typically 75 amperes at 6 kV applied to the control grid, t_j was reduced to less than 2 nS for each of the experimental tubes. The jitter question was not totally resolved, however, as described further below.

After 15 minutes to about 1 hour of running time from a cold start (depending on tube type), t_j would gradually increase from some unmeasurable or insignificant value to values of the order of 10 nS, with tubes having tighter gradient grid baffling being most prone to operate with jitter. An investigation later showed that t_j was not dependent on time or prr but rather on the total number of shots accumulated after a long rest period. Shot-dependent phenomena are indicative of a cathode-related process, and the cathode might be involved in the observed behavior.

To investigate the dependence of t_j on the properties of the cathode, each tube was operated until significant jitter appeared, and then the cathode heater voltage was increased 10% above its nominal value. In each case, t_j was reduced to near-zero at the higher heater voltage. For the highly baffled tubes, t_j eventually began to increase at even the higher cathode temperature; for the 5506, t_j remained unmeasurable after several hours. A similar set of experiments was then performed except that the heater voltage was reduced to 90% of its nominal value. In the low heater case, t_j again decreased to near-zero at first, and then gradually increased to 10 nS or more. Since changing the cathode temperature caused new regions of the cathode to become activated (only to become depleted after some number of shots), the cathode heater experiments demonstrated that the observed jitter was in fact the result of a cathode depletion process. Furthermore, it is reasonable that this effect would be most pronounced (as it was) in those tubes having highly baffled gradient grids, since any perturbations in the triggering plasma can only be emphasized by grid structures having a low transfer efficiency.

The results of the jitter investigation are summarized as follows: the aperture offset between the auxiliary grid and the control grid baffle was excessive. This condition made auxiliary grid triggering unreliable, and the use of keep-alive ineffective. It also resulted in a time jitter of tens of nanoseconds when the tubes were control-grid triggered with a usually adequate drive of 30 amperes at 1200 volts.

To force a reasonable t_j , the control grid was pulsed with 75 amperes at 6 kV. The time jitter was then 2 nS or less for the three tubes under test. A shot-dependent jitter characteristic was discovered that was traced to the cathode and is believed to be the result of a cathode depletion process that occurs under high di/dt conditions.

It is a trivial matter to correct the aperture situation for future tubes, and this has been done for the intermediate tube for ERADCOM (Section 8.0). The cathode situation is less straightforward but nonetheless feasible to correct. It has long been recognized that a short, highly utilized cathode would be required for this application and others that involve operation at high di/dt . The first in a series of such cathodes have been designed and are in the process of being built into a single-stage tube for initial testing. At present, the development of a suitable cathode will not hinder progress on this Program.

Anode Delay Time

As previously discussed, the output of the CVR was a convenient mechanism to use to determine t_{ad} . This diagnostic was used to generate the data of Table 13, which shows (as a function of pressure) the time to breakdown for each gap and also the anode delay time, t_{ad} , for the HY-5506, 5508, and 5509. For the data of Table 13, the tubes were control-grid triggered (1200 volts at 60 amperes, maximum), * $t = 0$ corresponds to the time where control grid current was first observed, and t_{ad} corresponds to the time where anode takeover had clearly occurred. For each datum point in Table 13, $i_b = 3$ kA and $e_{py} = 30$ kV; therefore, the voltage across each stage was the same for

*Because of the baffle aperture configuration previously described, similar data with an auxiliary grid keep-alive would be of no value.

Table 13. Breakdown times (per gap) of box-grid tubes.*

HY-5506	Pressure	Gap					Total (tad)
		No. 1	No. 2	No. 3	No. 4	No. 5	
($\alpha = 0.4$)	320	60	36	48	41	29	214
	352	52	33	36	36	24	181
	390	48	28	28	34	24	162
	430	30	26	28	30	20	134
	475	27	23	24	24	18	116
	525	27	21	23	22	15	106
	588	27	21	21	20	15	104

HY-5508	Pressure	Gap			Total (tad)
		No. 1	No. 2	No. 3	
($\alpha = 0.95$)	316	160	80	48	288
	358	158	80	40	278
	393	156	72	38	266
	454	156	44	36	236
	504	154	40	32	226
	565	154	32	24	210
	600	148	26	20	194

HY-5509	Pressure	Gap			Total (tad)
		No. 1	No. 2	No. 3	
($\alpha = 0.75$)	308	140	72	58	270
	342	132	58	54	244
	360	128	58	40	226
	424	124	52	39	215
	470	120	46	36	202
	520	112	39	32	183
	580	104	40	28	172
	645	100	32	20	152

*Pressures in microns; times in nanoseconds; gaps numbered from cathode to anode.

each tube type regardless of gas pressure. Note first from Table 13 that, as expected, all gaps break down faster as the pressure is increased. This characteristic applied even to the last gap — an indicator that upper-stage arcing did not occur.

For each tube, the first gap required the longest period to break down. It is probable that the large offset between the auxiliary grid and the control grid baffle exaggerated this characteristic, so no significant conclusion can be drawn from such behavior. It is, however, interesting that the propagation time through the upper stages invariably decreased toward the anode, apparently due to an acceleration of the triggering plasma under the influence of the increased field as commutation progressed along the length of the tube.

The more highly baffled the tube, the longer the time required for commutation to occur. This is consistent with the concept that commutation is fostered by the physical progression of the triggering plasma through the various grids, with the low-field region of a highly baffled box tending to slow the motion of the plasma toward the last gap.

8 INTERMEDIATE HIGH VOLTAGE, LOW INDUCTANCE
HYDROGEN THYRATRON — HY-5525

For the intermediately sized experimental tube to be delivered to ERADCOM, a conservative design based on the experimental results of Phase II was chosen. The goal is to demonstrate a peak forward holdoff capability arbitrarily chosen to be 150 kV with a tube that operates at high pressure (for a short "resistive" fall time) and has an inductance of less than 50 nH. At lower pressures (but still high by thyatron standards), an epy well in excess of 150 kV is expected. The intermediate tube has been designated as HY-5525. A section drawing showing its salient features is given as Figure 52.

The tube envelope is 4.5 inches in diameter and the tube stands 6.3 inches high from the bottom of the cathode flange to the top of the anode flange. It has five gaps, since 30 kV per stage (on average, and at high pressure) is reasonable in light of the experiments, and yet the combined length of the high voltage sections is short enough to provide a low total inductance. The tube is designed for use with a 12-inch diameter current return. The inductance of the tube/return combination will be about 40 nH. The tube should be capable of generating a 10 kA, 60 nS current pulse having a rise time of 10 to 15 nS. A pulse repetition rate of 1 kHz should be achievable in the burst mode.

The design approach is basically conservative in that only concepts that have been experimentally verified have been used. For example, liquid cooling of the anode was provided for, but use of a hollow anode was avoided since our experience with such anodes is limited. The gap spacing was varied from 0.121 inch at the control grid to 0.115 inch at the anode to improve the voltage distribution across the tube (C1/C2 is about 12 for a 12-inch return and about 13 for a 14-inch return), but even the 0.115-inch gap is well above the spacing (0.090) where our experimental results show that field emission may become a concern.

The upper-stage insulator is 1.515 inches long. This is more than adequate according to the results of the ceramic tests. The stress during commutation is only one-third greater than that corresponding to the 118 kV data for the HY-5509 as discussed earlier in this report.

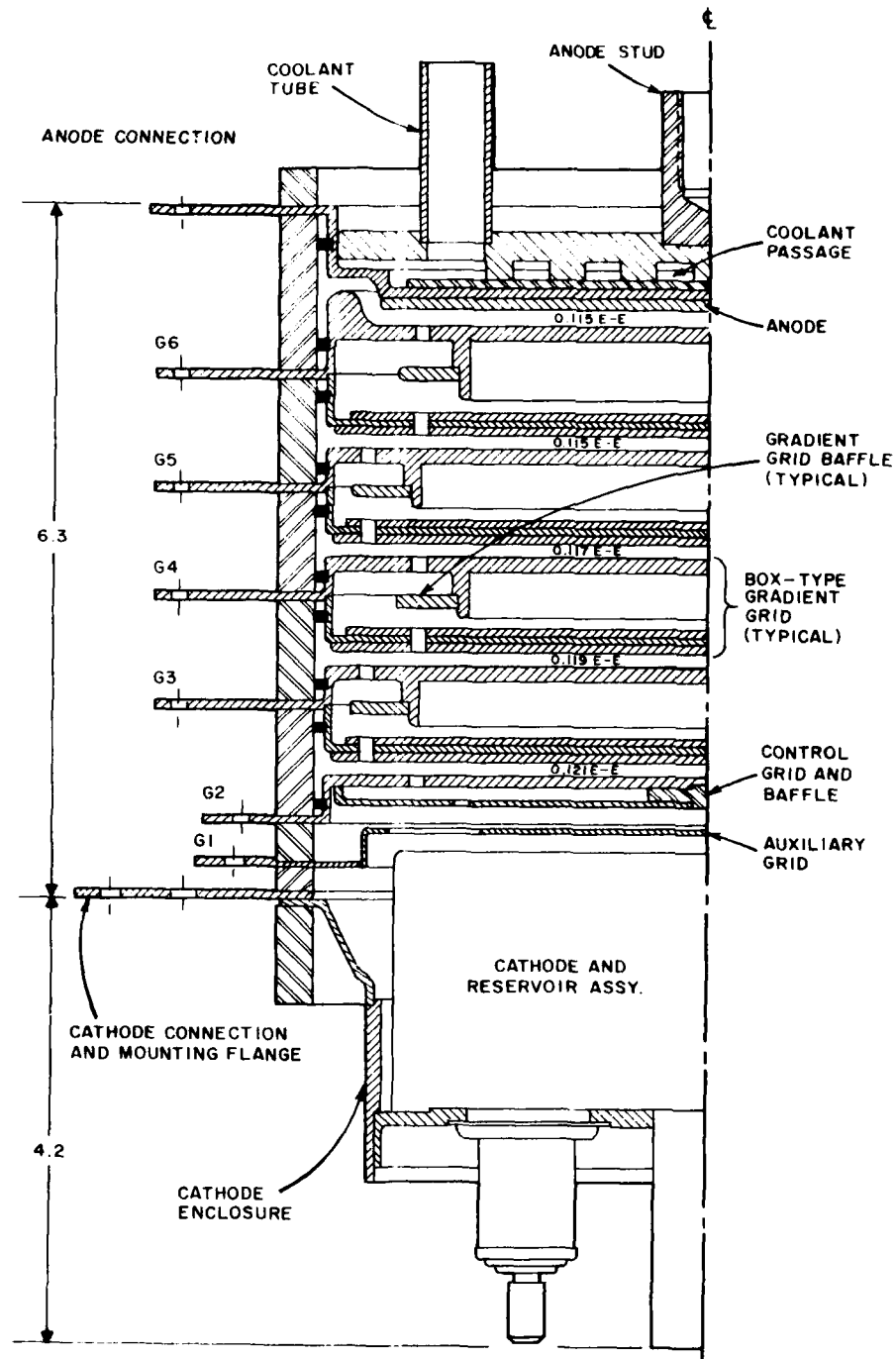


Figure 52. Intermediate experimental tube - HY-5525. The tube should be capable of generating a 10 kA current pulse having a rise time of 10-15 nS. A peak forward holdoff capability of 150 kV is expected at high pressure. The calculated inductance of the tube and a 12-inch current return is 40 nanohenries.

A ratio of baffle thickness to internal grid height about 1.5 times that of the HY-5509 but only one-half that of the HY-5508 is used for the gradient grid baffles. Therefore reasonably good stage isolation ($\alpha \approx 0.9$) without triggering problems is expected.

Finally, it was decided to offset the apertures from grid-to-grid but not within each grid despite grid studies, as discussed earlier in this report, because all of our experimental data apply for such a grid arrangement, while the theory has yet to be experimentally verified.

Some concessions were made in the design of the HY-5525 for expediency. For example, high di/dt experiments with standard HY-5313s at $i_b = 10$ kA have shown that a short, vertically vaned cathode will ultimately be required for high voltage, low inductance tubes. Specially shaped insulators (a project now in process) will allow higher holdoff per stage and promote longer tube life. Also, a thick, hollow anode will probably be required to provide reasonable life at high i_b . Finally, improved gradient grid baffling techniques will be required to achieve operation at pulse repetition rates beyond about 1 kHz.

Despite these considerations, building and testing a high voltage tube that extends previous work and demonstrates high voltage holdoff and low inductance is an important step toward achieving the objectives of the Program.

9 CONCLUSIONS FROM PHASE II AND PLANS FOR PHASE III

a. Conclusions from Phase II

A low-inductance hydrogen thyratron capable of reliable operation at 250 kV is feasible. No impediments to success are known to exist.

The ceramic breakdown tests showed that the inherent dielectric strength of high alumina ceramics exceeds that required for the insulators of a tube that can meet the objectives of this Program. However, the tests also showed that no local regions of uncontrolled stress can be allowed to exist either inside or outside of the tube. Furthermore, the tests were conducted only at room temperature and at low repetition rates. Although the insulator issue will not be resolved until life data are accumulated for actual tubes operating at significant pulse repetition rates, the existing data justify tube designs having a calculated inductance well within the limit set by the requirements of this Program.

It is now established that a multi-stage tube having a plurality of short, box-type gradient grids can in fact hold off, commute, and recover in the same manner as a conventionally designed tube. Internal baffles are an effective mechanism for determining the holdoff/commutation properties of such grids, and the baffles simultaneously promote tube operation at high pulse repetition rates. With properly designed grids, near-perfect stage voltage addition can be achieved with a holdoff structure that commutates easily and reliably.

Box-type grids can be modeled, computer-generated field plots can be used to aid in the specifics of their design, and their predicted characteristics are consistent with their measured voltage addition properties. Although further work is required to determine whether tube performance is dominated by the relative or absolute fields present in the grid structures, the work of Phase II has (for the first time) provided an analytical technique for the design of thyratron grids. The use of this technique has already allowed the design of effective grid structures without the need to resort to costly and time consuming experimentation.

A comprehensive theoretical analysis of anode dissipation has yielded relations that predict the anode heat loads that will be encountered under a variety of operating conditions. The analysis predicts a total tube loss well under 10%. Thermal analyses and testing of practical grid and anode structures must now be performed.

Command pulsed charging with a few microseconds for the voltage run-up and a few microseconds at full charge allows tube operation at significantly increased peak forward anode voltages. Furthermore, pulsed charging precludes kick-outs while simultaneously reducing the high voltage exposure time of the system as a whole.

Even under pulsed charge conditions, the anode breakdown voltage is a strong inverse function of the gas pressure in the tube. The multi-stage tubes built during Phase II were capable of holding off very high voltages at pressures where their triggering characteristics were acceptable and their anode fall times reasonably fast, but for very high di/dt applications, operation at even higher gas pressures is required. It is thus clear that the most significant single advance that can be made during the next phase of this Program will be to devise a means for increasing the dynamic breakdown voltage (per stage) at still higher gas pressures. Mechanisms for doing this are under investigation.

The recovery characteristics of the existing multi-stage, box-gridded tubes were in general about a factor of 10 poorer than those of a single-stage tube having the same diameter. A recovery capability consistent with operation at 1 kilohertz was, however, achieved. Further work on grid baffle design (now underway) is expected to result in an order of magnitude improvement in the recovery time.

The rise time capabilities and triggering characteristics of box-grid tubes are of the same general nature as those of conventionally designed thyratrons. The experimental multi-stage tubes had actual inductances that were consistent with those calculated on the basis of their geometries. As expected, when these tubes were operated in a very low inductance circuit, the rise time of the circuit current was limited not by inductance, but rather by

the "resistive" anode fall times of the tubes. The time constant of the anode fall depends solely on the gas pressure in the tube, so tubes used in high di/dt service must be operated at high gas pressures.

During Phase II, 3 kA current pulses having a rise time of 10 nS were routinely generated by various multi-stage experimental tubes. This corresponds to a di/dt per volt of 8×10^6 A/S/volt. From the applicable Technical Guidelines (Table 1), a di/dt per volt of 1.28×10^7 can be inferred, i.e., a switching capability not far removed from that already demonstrated in the laboratory. The conclusion is that the inherent switching capabilities of hydrogen thyratrons are consistent with the needs of the Program.

In general, the experimental tubes commutated easily and reliably, and with a modest grid drive. This was true even of that tube having the highest degree of gradient grid baffling (and thus the best stage voltage addition). As expected, higher baffling increased the anode delay time, but anode delays less than 200 nS were always achievable at high gas pressures. No indication of upper-stage arcing was observed under any reasonable operating conditions.

The experimental tubes exhibited excessive time jitter. The jitter was traced to an apparent cathode depletion process and an excessive control grid baffle offset, so excessive jitter does not appear to be an inherent characteristic of multi-stage, box-grid tubes. Even those tubes having the excessive baffle offset could be made to commutate with a jitter of about 2 nS when sufficiently driven. Improved baffle designs have since been generated, and a low inductance, generally high-performance cathode must now be developed for use in tubes that operate under conditions of high di/dt.

b. Plans for Phase III

It is required that the experimental work of Phase II be extended to include tube operation at much higher voltages — up to and including 250 kV. Such operation is necessary to prove that the upper-stage insulators are in fact adequate, that stage voltage addition can be maintained in the presence of high electric fields, and that upper-stage arcing will not in fact occur.

Toward this end, the 250 kV test kit has been repaired, and this system is expected to be in operation shortly. Some data can be generated by using this kit to test the existing experimental tubes (at reduced gas pressures), but it is more beneficial to take advantage of the results of the Phase II efforts, and to build a series of experimental tubes that is specifically designed to address those considerations that prompt the greatest practical concern. Therefore a theoretical and experimental effort will be conducted to determine the relative significance of the transfer field ratio (γ) versus the absolute field intensity (particularly in connection with upper-stage arc prevention). Experimental work should be done to improve the high pressure holdoff of individual gaps — mainly by developing new insulator and electrode geometries.

Under the terms of our existing contract with ERADCOM, Phase III requires the delivery of a prototype high voltage, low inductance tube. However, a proposal to conduct additional experimental work on a time scale that will encompass the whole of Phase III and beyond has been submitted to the Naval Surface Weapons Center (NSWC).

In the work for NSWC, it is planned to use the same theoretical/experimental approach used during Phase II of this Program, use computer-generated field plots to aid in the specifics of gradient grid design, and build and test experimental tubes to verify the results of the theoretical work. In addition to the principal concerns mentioned above, certain practical considerations also need to be addressed. These include the use of offset apertures within each gradient grid to reduce inductance, complexity, and cost, "hollow" anodes to reduce damage by electron bombardment, and gradient grid baffling arrangements that are specifically designed to promote rapid recovery and thus promote tube operation at high pulse repetition rates. A new, low inductance, high performance cathode must also be developed that is specifically suited to the rigors of high current, high di/dt operation, and the triggering characteristics of multi-stage tubes so equipped must be determined under high di/dt conditions.

Early during the effort described above, it will be necessary to commit to a design for the prototype tube of Phase III so that the device can be delivered to ERADCOM on schedule. At present, it is planned to build simultaneously at least one additional tube of a generally similar nature (perhaps with interesting variations), and to test this tube during the balance of the NSWC effort.

Finally, it is hoped that NSWC will extend the overall Program to include a "Phase IV." The emphasis of the Phase IV effort will be to study those factors that presently serve to limit the pulse rate capabilities of high voltage, low inductance tubes, and to extend those capabilities as far as possible. Our goal is to demonstrate high voltage operation at (at least) 10 kHz by the end of 1981.

10 REFERENCES

1. Rogers, W.E., Introduction to Electric Fields, McGraw-Hill, New York, 1954. p. 162.
2. Kraus, J.D., Electromagnetics, McGraw-Hill, New York, 1953. p. 74.
3. Caristi, R.F., and Turnquist, D.V., Research and Development Technical Report No. DELET-TR-77-2725-F, March 1979. p. A-3.
4. Caristi, R.F., et al., 1979. ED-26, No. 10, October.
5. Goldberg, S., and Rothstein, J., Advances in Electronics and Electron Physics, Vol. XIV, "Hydrogen Thyratrons," Academic Press, New York, 1961. p. 234.

DISTRIBUTION LIST

012	Defense Documentation Center ATTN: DDC-TCA Cameron Station (Bldg 5) Alexandria, VA 22314	001	Command, Control & Communications Division Development Center Marine Corps Develop & Educ Comd Quantico, VA 22134
001	Code R123, Tech Library DCA Defense Comm Engrg Ctr 1800 Wiehle Ave Reston, VA 22090	001	Rome Air Development Center ATTN: Documents Library (TILD) Griffiss AFB, NY 13441
001	Defense Communications Agency Technical Library Center Code 205 (P.A. Tolovi) Washington, DC 20305	001	HQ, Air Force Systems Command ATTN: DLCA Andrews AFB Washington, DC 20331
001	Office of Naval Research Code 427 Arlington, VA 22217	001	Cdr, MIRADCOM Redstone Scientific Info Center ATTN: Ch, Document Section Redstone Arsenal, AL 35809
001	Commander Naval Surface Weapons Center ATTN: F-12 (K. Baile) Dahlgren, VA 22448	001	Commandant US Army Aviation Center ATTN: ATZQ-D-MA Fort Rucker, AL 36362
001	Cdr, Naval Surface Weapons Center White Oak Laboratory ATTN: Library Code WX 21 Silver Spring, MD 20910	001	Director, Ballistic Missile Defense Advanced Technology Center ATTN: ATC-R, PO Box 1500 Huntsville, AL 35807
001	Commander Naval Surface Weapons Center ATTN: Dr. M. F. Rose Dahlgren, VA 22448	001	Commander US Army Intelligence Center & School ATTN: ATSI-CD-MD Fort Huachuca, AZ 85613
001	Commander Naval Surface Weapons Center ATTN: Dr. Gripshover Dahlgren, VA 22448	001	Commander HQ, Fort Huachuca ATTN: Technical Reference Div Fort Huachuca, AZ 85613
001	Commander Naval Surface Weapons Center ATTN: F-12 (D. Lindberg) Dahlgren, VA 22448	001	Commander Naval Surface Weapons Center ATTN: F-12 (H. Odom) Dahlgren, VA 22448
001	Commander Naval Surface Weapons Center ATTN: F-12 (L. Leussen) Dahlgren, VA 22448		

001 Director Naval Research Laboratory ATTN: Code 2627 Washington, DC 20375	002 Commander, Picatinny Arsenal ATTN: SARPA-FR-5 Bldg 350 Dover, NJ 07801
001 Deputy for Science & Technology Office, Assist Sec Army (R&D) Washington, DC 20310	001 Commander US Army Satellite Communications Agency ATTN: DRCPM-SC-3 Fort Monmouth, NJ 07703
001 HQDA (DAMA-ARZ-D/Dr. Verderame) Washington, DC 20310	001 Cdr, USA Missile R&D Command ATTN: DRCPM-HEL (T. Roberts) Redstone Arsenal, AL 35809
001 Commandant US Army Signal School ATTN: ATSN-CTD-MS Fort Gordon, GA 30905	001 Cdr, Rome Air Development Center ATTN: Mr. B. Gray Griffiss AFB, NY 13441
001 Cdr, Harry Diamond Labs ATTN: Library 2800 Powder Mill Road Adelphi, MD 20783	001 Cdr, Ballistic Missile Defense Advanced Technology Center ATTN: ATC-T (L. Havard) Redstone Arsenal, AL 35809
001 Director US Army Ballistic Research Labs ATTN: DRXBR-LB Aberdeen Proving Ground, MD 21005	001 Cdr, US Army Mobility Equipment Research & Development Command ATTN: DRDME-EA (Dr. Amstutz) Fort Belvoir, VA 22060
001 Harry Diamond Laboratories, DA ATTN: DELHD-RCB (Dr. Nemarich) 2800 Powder Mill Road Adelphi, MD 20783	001 Cdr, Naval Surface Weapons Center ATTN: Mr. C. Hudelston White Oak Laboratory Silver Spring, MD 20910
001 Director, US Army Materiel Systems Analysis Activity ATTN: DRXSY-MS Aberdeen Proving Ground, MD 21005	001 Cdr, Air Force Aero Propulsion Lab AFAPL/POD-1 (Mr. R. Verga) Wright-Patterson AFB, Ohio 45433
001 Mr. A. Gordon ITT Electron Tube Division Box 100 Easton, PA 18042	001 Dr. S. A. Gilmore Dept of Electrical Engineering State University of New York 4232 Ridge Lea Road Amherst, NY 14226
001 Dr. Robin Harvey Hughes Research Laboratory 3011 Malibu Canyon Road Malibu, California 90265	001 Dr. M. Kristiansen Texas Tech University College of Engineering PO Box 4439 Lubbock, Texas 79409
001 Cdr, Naval Air Systems Command NAVAIR-350F (R. J. Wasneski) Washington, DC 20361	

001 Cdr, US Army Research Office ATTN: DRXRO-IP PO Box 12211 Research Triangle Park, NC 27709	002 Commander US Army Logistics Center ATTN: ATCL-MC Fort Lee, VA 22801
001 Cdr, US Army Research Office ATTN: DRXRO-PH (Dr. R. Lontz) PO Box 12211 Research Triangle Park, NC 27709	001 Cdr, PM Concept Analysis Center ATTN: DRCPM-CAC Arlington Hall Station Arlington, VA 22212
001 Commandant US Army Inst for Military Assistance ATTN: ATSU-CTD-MO Fort Bragg, NC 28307	001 Chief Ofc of Missile Electronic Warfare Electronic Warfare Lab, ERADCOM White Sands Missile Range, NM 88002
001 Commandant US Army Air Defense School ATTN: ATSA-CD-MC Fort Bliss, TX 79916	001 Chief Intel Materiel Dev & Support Ofc Electronic Warfare Lab, ERADCOM Fort Meade, MD 20755
001 Commander US Army Nuclear & Chemical Agency 7500 Backlick Rd, Bldg 2073 Springfield, VA 22150	001 Cdr, Harry Diamond Labs ATTN: DELHD-CO 2800 Powder Mill Road Adelphi, MD 20783
001 HQ, TCATA Technical Information Center ATTN: Mrs. Ruth Reynolds Fort Hood, TX 76544	001 Commander ARRADCOM DRDAR-TSB-S Aberdeen Proving Ground, MD 21005
001 Commander, DARCOM ATTN: DRCDE 5001 Eisenhower Ave Alexandria, VA 22333	001 Commander, ERADCOM ATTN: DRDEL-CG; -CD; -CS (IN TURN) 2800 Powder Mill Road Adelphi, MD 20783
001 Cdr, US Army Signals Warfare Lab ATTN: DELSW-OS Vint Hill Farms Station Warrenton, VA 22186	001 Cdr, ERADCOM ATTN: DRDEL-CT 2800 Powder Mill Road Adelphi, MD 20783
001 Commander US Army Mobility Equip R&D Command ATTN: DRDME-R Fort Belvoir, VA 22060	001 Dr. John Hammond W. J. Schafer Associates, Inc. Clinton Bldg, Suite 408 2109 W. Clinton Avenue Huntsville, AL 35805
001 Maxwell Laboratories ATTN: Mr. R. Fitch 9244 Balboa Ave San Diego, CA 92123	001 Cdr, Air Force Weapons Laboratory AFWL/ALE (J. O'Loughlin) Kirtland Air Force Base New Mexico 87117

001 Cdr, ERADCOM ATTN: DRDEL-PAO 2800 Powder Mill Road Adelphi, MD 20783	Commander US Army Communications & Electronics Materiel Readiness Command Fort Monmouth, NJ 07703
001 Cdr, ERADCOM ATTN: DRDEL-LL; -SB; -AP (IN TURN) 2800 Powder Mill Road Adelphi, MD 20783	1 DRSEL-PL-ST 1 DRSEL-MA-MP 2 DRSEL-PA
001 Cdr, ERADCOM ATTN: DRDEL-AQ 2800 Powder Mill Road Adelphi, MD 20783	001 CINDAS Purdue Industrial Research Park 2595 Yeager Road W. Lafayette, IN 47096
001 Cdr, ERADCOM ATTN: DRDEL-PA; -ILS; -ED (IN TURN) 2800 Powder Mill Road Adelphi, MD 20783	002 MIT- Lincoln Laboratory ATTN: LIBRARY (Rm A-082) PO Box 73 Lexington, MA 02173
001 HQ, Harry Diamond Laboratories ATTN: DELHD-TD (Dr. W.W. Carter) 2800 Powder Mill Road Adelphi, MD 20783	001 NASA Scientific & Tech Info Facility Baltimore/Washington Intl Airport PO Box 8757, MD 21240
Commander US Army Electronics R&D Command Fort Monmouth, NJ 07703	001 National Bureau of Standards Bldg 225, Rm A-331 ATTN: Mr. Leedy Washington, DC 20231
1 DELET-D 1 DELET-DD 2 DELET-DT 5 DELET-BG (W. Wright) 1 DELSD-L (Tech Library) 2 DELSD-L-S (STINFO)	002 Advisory Group on Electron Devices 201 Varick Street, 9th Floor New York, NY 10014
Commander US Army Communications R&D Command Fort Monmouth, NJ 07703	002 Advisory Group on Electron Devices ATTN: SECY, Working Grp D (Lasers) 201 Varick Street New York, NY 10014
1 DRDCOM-COM-RD 1 USMC-LNO 1 ATFE-LO-EC	001 TACTEC Battelle Memorial Institute 505 King Avenue Columbus, OH 43201
001 Cdr, Air Force Weapons Laboratory ATTN: Dr. A. Guenther (AFWL/CA) Kirtland Air Force Base, NM 87117	001 Plastics Tech Eval Center Picatinny Arsenal, Bldg 176 ATTN: Mr. A.M. Anzalone Dover, NJ 07801
001 Lawrence Livermore Laboratory ATTN: L. Reginato PO Box 808 Livermore, CA 94550	001 Metals & Ceramics Inf Center Battelle Memorial Institute 505 King Avenue Columbus, OH 43201

001 Mr. Phil Mace
Los Alamos Scientific Laboratory
PO Box 1663
Los Alamos, NM 87545

001 Cdr, Defense Advanced Research
Projects Agency
DARPA/STO (J. Mangano)
1400 Wilson Boulevard
Arlington, VA 22209

001 Cdr, Defense Advanced Research
Projects Agency
ATTN: Col. Benedict, J. Bayless
(In Turn)
1400 Wilson Boulevard
Arlington, VA 22209

001 Avco-Everett Research Laboratory
2385 Revere Beach Parkway
ATTN: Mr. R. Feinberg
Everett, MA 02149

001 Avco-Everett Research Laboratory
2385 Revere Beach Parkway
ATTN: Dr. J. Jacobs
Everett, MA 02149

